Dissertation
submitted to the
Combined Faculties for the Natural Sciences and for Mathematics
of the Ruperto-Carola University of Heidelberg, Germany
for the degree of
Doctor of Natural Sciences

presented by
Pascal Geschwill, M.Sc.
born in: Speyer, Germany
Oral Examination: 29.09.2017

Cellular and Network Mechanisms
Underlying the Switch Between Hippocampal Oscillatory States

Referees: Prof. Dr. Andreas Draguhn
Prof. Dr. Hilmar Bading

Abstract

Local field potentials in the hippocampus are dominated by two different activity patterns - persistent gamma band (30-60Hz) oscillations and intermittent sharp wave-ripple (∼200Hz) complexes. The former are associated with exploratory behaviours in which information is acquired while the latter are believed to be involved in transfer and consolidation of information to long-term memory. Although there is a great wealth of knowledge about how neuronal networks maintain each oscillatory state, it is not entirely clear what cellular mechanisms mediate the switch between gamma to sharp wave-ripple activity.

The goal of this thesis was to characterise this transition at the network and synaptic level. To this end, an *in vitro* model based on acute hippocampal slices was established in which both gamma rhythms and sharp wave-ripples could be evoked. This was achieved with a custom-built holographic illumination system granting targeted and selective optogenetic stimulation of pyramidal cells. Prolonged stimulation of the reduced hippocampal slice network elicited self-synchronisation to a gamma rhythm (∼50Hz) with a resonance at theta frequency inputs (i.e. 4-5Hz sinusoidal stimulation). This frequency preference was confirmed at the single unit level which revealed most precise coordination of single cell activity within the ongoing gamma rhythm at theta frequency inputs. Additionally, evoked gamma synchronisation emerged suddenly ∼200ms after stimulus onset indicating a near instantaneous switch of hippocampal network states. This finding was reflected in whole-cell recordings of postsynaptic currents which displayed a sharp increase in both excitatory and inhibitory inputs around 200-300ms after stimulus onset. On the other hand, applying short (5ms) square pulses of low intensity stimulation evoked local field potential signatures closely resembling sharp wave-ripples. This implies that stimulus duration and profile are critical determinants of network output.

The results presented here provide experimental evidence for prevailing models of different hippocampal network oscillations and extend the knowledge about how neuronal networks can maintain different oscillatory states and how the transition between these states is brought about.

Zusammenfassung

Lokale Feldpotentiale im Hippokampus sind geprägt von zwei verschiedenen Aktivitätszuständen - persistierende Gamma (30-60Hz) Oszillationen und sporadisch auftretende sharp wave-ripple (∼200Hz) Komplexe. Gamma Oszillationen treten während explorativem Verhalten auf, das mit der Aufnahme von Information assoziiert ist, wohingegen sharp wave-ripples mit der Übertragung von Information in das Langzeitgedächtnis in Verbindung gebracht werden. Trotz der vielen Erkenntnisse über die Aufrechterhaltung verschiedener Netzwerkzustände, sind die zellulären Mechanismen, die für das Umschalten zwischen den Zuständen nötig sind, nicht abschließend geklärt.

Das Ziel dieser Disseration bestand darin, diesen Übergang sowohl auf Netzwerk- als auch auf synaptischer Ebene zu charakterisieren. Hierzu wurde ein *in vitro* Modell basierend auf einem akuten hippokampalen Schnittpräparat etabliert, in dem durch gezielte und selektive, optogenetische Stimulation von Pyramidenzellen Gamma Rhythmen und sharp wave-ripples evoziert werden konnten. In der Folge lang anhaltender, optogenetischer Stimulation bildete das reduzierte hippokampale Netzwerk synchronsierte Gamma Oszillationen (∼50Hz) aus, die eine Präferenz zur Stimulation in niedrigen Theta Frequenzbereich zeigten (z.B. 4-5Hz sinusoidale Stimulation). Dies wurde auf single unit Ebene bestätigt, was auf eine präzisere Koordinierung von Einzelzellaktivität in den Gamma Rhythmus hindeutet. Darüberhinaus entstehen Gamma Oszillationen in einem stufenartigen Vorgang, was ein unmittelbares Umschalten des Netzwerkzustandes nahelegt. Diese Beobachtung wurde anhand von whole-cell Messungen von inhibitorischen und exzitatorischen synaptischen Strömen bestätigt, welche einen scharfen Frequenzanstieg etwa 200-300ms nach Beginn des Stimulus aufwiesen. Kurze, 5ms lange Rechteckspulse lösten hingegen ein Feldpotential aus, das sharp wave-ripples ähnelt, was darauf hin weist, dass Stimulationsdauer und -profil die Netzwerkantwort beeinflussen.

Die hier vorgelegten Ergebnisse dienen als experimentelle Hinweise für gegenwärtige Modelle der Funktionsweise von hippokampalen Netzwerken. Zudem erweitern sie den Kenntnisstand über sowohl die Aufrechterhaltung verschiedener Aktivitätsmuster als auch das Umschalten zwischen den Netzwerkzuständen.

Contents

1 Introduction

1.1 Structure and Function of the Hippocampal Formation

1.1.1 Anatomical Overview and Circuitry

The hippocampus (HC) is a bilaterally located cerebral structure in vertebrates which lies at the medial side of the temporal lobe. It is part of the limbic system which among other structures comprises the hypothalamus and the amygdala. Due to its remote morphological resemblance to a seahorse, the hippocampus was named after the animal's Latin name by the Venetian anatomist Arantius in 1587 (Bir et al., 2015). The hippocampal formation consists of several subregions, namely the dentate gyrus (DG), *Cornu Ammonis* (CA) and the subiculum (Sub). The CA area itself is subdivided into three subfields CA3, CA2 and CA1 and is commonly referred to as hippocampus proper (Amaral and Witter, 1989). The CA3 area is further partitioned into CA3a, CA3b and CA3c according to its distance the DG from distal to proximal (Lorente de No, 1934). Both the dentate gyrus and the hippocampus proper are roughly U-shaped which appear interlocked anatomically (see figure 1.1).

One of the most noticeable anatomical features of the hippocampal areas is their strikingly clear lamination. The layers differ in cellular composition and are mainly constituted by a single neuronal domain. The molecular layer (*stratum moleculare*) of the dentate gyrus, its outermost layer, mostly contains the conical dendritic arborisations of granule cells as well as input fibers from the entorhinal cortex (EC) which form the perforant path. The granule cell layer (*stratum granulare*) is constituted of the somata of granule cells, the main excitatory (glutamatergic) cell type of the DG. Situated at the innermost part of the DG is the hilus which is pervaded by granule cell axons forming the mossy fibre tract projecting towards CA3 (Amaral and Witter, 1989). Besides several types of inhibitory γ-aminobutyric acid (GABA) secreting interneurons, small excitatory mossy cells are also located in the hilus (Sik et al., 1997; Amaral, 1978). In the hippocampus proper (CA3 and CA1), a total of six layers can be identified, namely *stratum lacunosum-moleculare, stratum radiatum, stratum lucidum, stratum pyramidale, stratum oriens and alveus* of which the

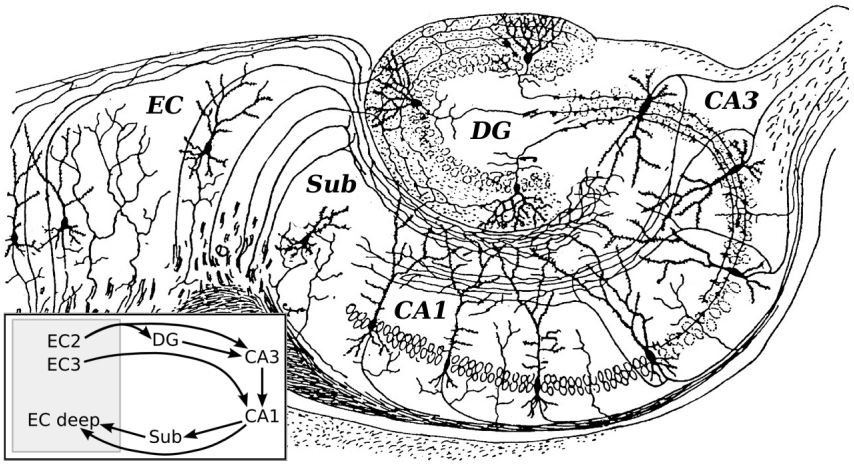

Figure 1.1: Anatomical overview of the rat hippocampus. *Shown here is the hippocampal formation (DG, CA3, CA1, Sub) together with its main input area, the entrorhinal cortex (EC). The inset at the bottom left summarizes the basic circuitry of the hippocampus. The image is adapted from an anatomical drawing by Santiago Ramón y Cajal published in 1911 (Wikipedia, 2017).*

stratum lucidum is only found in CA3 as it contains the mossy fibre endings. The most prevalent cell type of the CA areas is the glutamatergic pyramidal cell (PC) whose apical dendritic arbour extends through the *strata radiatum* and *lacunosum-moleculare*. Their basal dendritic tree is located in the *stratum oriens*. CA3 PCs receive inputs from the DG and from layer II of the EC and in turn send heavily collateralised axons towards the apical and basal dendrites of CA1 PCs. The glutamatergic synapses of these so called Schaffer collaterals are one of the most well described neuronal connections in the neuroscientific literature (Collingridge et al., 1983; Whitlock et al., 2006). Apart from Schaffer collateral input which terminates in the *stratum radiatum* and *stratum oriens*, PCs in the CA1 area receive excitatory transmissions from layer III of the EC to their distal dendritic domains within *stratum lacunosum-moleculare* (Deng et al., 2010). Their axons form a densely packed bundle at the innermost border of the hippocampus proper which is called *alveus*. They project towards the Sub and EC as well as to the contralateral hippocampus and the prefrontal cortex via the *fornix*. A major feature that separates CA3 from CA1 is its highly recurrent innervation (Mitra et al., 2011) which leads to a strongly increased excitability of the region and is thought to be crucial for the generation of certain physiological signatures such as wave-ripple complexes (SPW-R) (Buzsaki et al., 1983).

The circuitry of the hippocampus is classically described by a trisnayptic excitatory loop (Amaral and Witter, 1989), i.e. the DG receives perforant path input from layer II of the EC and transfers this information to CA3. From there, the signal is carried towards CA1 via the Schaffer collaterals which ultimately send axons to the EC and various other brain regions. Although this description poses a mas-

sive simplification by omitting for example interneuron circuits, extrahippocampal neuromodulatory inputs or projections from the EC it still is a viable model for information transfer within the hippocampus. A more detailed account of hippocampal anatomy and circuitry can be found elsewhere (Andersen, 2007).

1.1.2 Memory Formation and Consolidation

The hippocampus is commonly referred to as the gateway to memory, meaning that is thought to be involved in transferring novel information to long-term mnemonic storage. This notion arose after the publication of the landmark medical case of Henry Gustav Molaison, more well known by his initials "H.M.", in 1957 (Scoville, 1954; Scoville and Milner, 1957). Patient H.M. suffered from severe recurrent intractable epileptic seizures which appeared drug resistant. Following the identification of the medial temporal lobe as the epileptogenic site, a bilateral lobectomy was performed which greatly alleviated his symptoms but also resulted in serious anterograde and partly retrograde amnesia. The memory impairments however were mostly restricted to explicit or declarative memory as he was still able to learn new motor skills (Corkin, 2002) thus underlining the importance of the hippocampus for the formation of new memories. After H.M.'s death in 2008 his brain was subjected to comprehensive anatomical analyses which revealed the extent of the temporal lobe resection (Augustinack et al., 2014; Annese et al., 2014). It was found that parts of the amygdaloid structures and posterior parts of the hippocampus were spared whereas most of the anterior hippocampal body and entorhinal cortices were lesioned. This may serve as an explanation for the observation that H.M. was still capable, albeit in a very limited manner, to memorize the names of previously unknown people.

Since the description of H.M.'s case, a large body of work has been conducted which was aimed at substantiating the role of the hippocampus in the transfer of information to long-term memory (Tulving and Markowitsch, 1998; Vargha-Khadem, 1997). Most of the studies that have contributed to this issue employed animal (mostly rodent) models of spatial memory which is a form of explicit memory and a very useful readout for the characterisation of mnemonic performance. It has for example been shown that rats with bilateral hippocampal lesions performed much worse in the Morris water maze task which reflects the animal's ability to encode or recall spatial memory (Morris, 1984). The ambiguity of whether this phenomenon is caused by impaired memory acquisition or recollection has been addressed in many other lesion studies in which retrograde amnesia is a very common observation (Nadel and Moscovitch, 1997; Winocur, 1990; Cho et al., 1993). These series of experiments provided strong evidence for the notion that the hippocampus serves

as an intermediate transmission hub which receives inputs from sensory systems and integrates them over time into neocortical storage structures. In line with this idea, it has been shown that recently experienced episodes are particularly vulnerable to hippocampal damage whereas older memory content remains relatively stable (Cho et al., 1995).

The observations in animal experiments mostly appear consistent with the descriptions of H.M.'s pathologies. However the question still remains whether spatial memory performance in rodents poses an adequate readout for the more complex mnemonic processes such as autobiographical memory that occur in humans. In recent years a theory has been brought forward attempting to bridge this gap which is based on a large body of evidence collected by György Buzsáki as well as Edvard and May-Britt Moser (Buzsaki and Moser, 2013). Their theory suggests that the neural mechanisms underlying egocentric or allocentric spatial navigation are similar to the ones mediating episodic or semantic memory processes. For example, a sequence of memorable moments of one's past can be navigated as if one is physically travelling from one place to another. Similarly, assigning a word or a meaning to a certain object or concept may recruit the same neuronal pathways required for planning a trip through a city using a map (Buzsaki, 2005; Eichenbaum et al., 1999; Lever et al., 2002). To date, numerous studies have been published in favour of this theory (Fortin et al., 2004; Kennedy and Shapiro, 2009; Eacott and Norman, 2004; Aronov et al., 2017) and although many of its details have to be experimentally proven, it remains a very compelling hypothesis for the function of the hippocampus in memory formation.

1.2 Hippocampal Physiology

The hippocampus expresses a variety of extracellular local field potentials (LFP) that can be categorized according to their leading oscillation frequency and their association with different behavioural states. While it is known that cortical structures exhibit oscillations spanning frequencies from 0.05Hz up to around 600Hz (Buzsaki and Draguhn, 2004), hippocampal field potentials are dominated by either gamma (30-60Hz) oscillations nested into a slower theta (4-10Hz) rhythm or SPW-R. In addition to these coordinated rhythmic activity patterns of large groups of cells that is thought to underlie these field potentials, it has been shown that action potential firing frequency of individual neurons of the CA region appears to be closely correlated to the location of an experimental animal (O'Keefe and Dostrovsky, 1971). This peculiar firing pattern of these so called place cells has since been found in many other species including humans (Ekstrom et al., 2003). The repertoire of place selective cells in the hippocampus and adjacent brain regions has steadily grown in recent

years and now includes among others, grid cells, border cells and head-direction cells (for review see Moser et al. (2008)).

It is important to note that neuronal network oscillations and single cell activity don't represent independent phenomena but instead cofunction as a framework which supports the mechanisms by which information can be encoded. Therefore, in order to highlight the role of network oscillations as a reference frame for the activity of individual neurons, the two most prominent rhythms of the hippocampus, theta-nested gamma oscillations and SPW-R and their correlation with spatial memory formation shall be described in more detail.

1.2.1 (Theta-nested) Gamma Oscillations

In rodents, theta oscillations emerge in the hippocampus during active exploratory behaviour and rapid eye movement (REM) sleep (Vanderwolf, 1969). They are usually accompanied by oscillations in higher frequency bands between 30 and 150Hz (Buzsaki et al., 1983). These two superimposed frequency signatures have been described as theta-nested gamma oscillations and are thought to represent an 'online' cognitive state in which information is acquired or processed. In the literature, gamma oscillations have been subdivided into at least three bands, slow (30-50Hz), medium (50-90Hz) and fast (90-150Hz) gamma (Belluscio et al., 2012) although the borders of these ranges vary (Scheffer-Teixeira et al., 2012). Throughout this thesis, I will refer to oscillations in the 30-60Hz band as gamma oscillations.

The interplay between local field potential and single cell activity and its apparent significance for spatial navigation was first described by O'Keefe and Recce (O'Keefe and Recce, 1993). It was demonstrated that the animal's location in space is not only encoded by the firing rate of place cells but that the phase relationship of unit firing with respect to the ongoing theta cycle also carries spatial information (see figure 1.2).

These findings have highlighted the importance of theta oscillations for navigational coding but the question in what way gamma oscillations contribute to these processes remains. Although to date, there is hardly any direct evidence for the necessity of gamma oscillatory activity for normal mnemonic performance, it has been shown that gamma band power is associated with increasing memory load (Osipova et al., 2006; van Vugt et al., 2010; Yamamoto et al., 2014) and is disturbed in patients suffering from schizophrenia (Chen et al., 2014). Another important parameter beyond gamma frequency and power that is frequently described in the literature is cross-frequency coupling (Tort et al., 2008). It has been demonstrated that the amplitude of gamma oscillations is modulated by the phase of an underlying theta band activity (Tort et al., 2010). This so-called phase-amplitude modulation

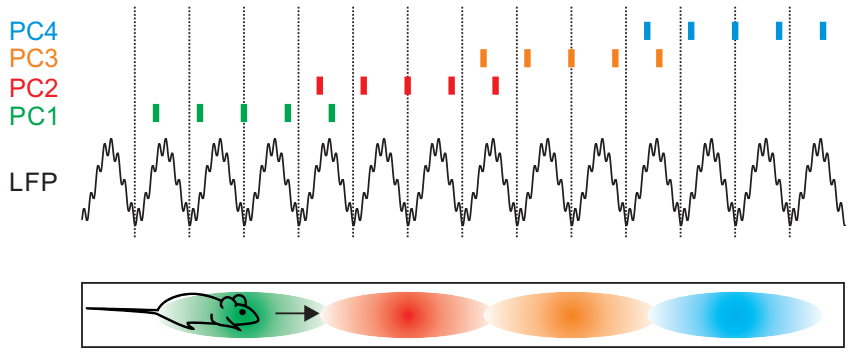

Figure 1.2: Schematic representation of place cell rate and phase coding. *Displayed here are schematic raster plots (top) where each colour corresponds to one place cell (PC1-4) and each bar indicates a spike. The black trace (middle) shows an exemplified local field potential trace with a fast oscillation superimposed onto a slower one. The troughs of the slow oscillation are marked by a dashed line. When a rat moves across a linear track, a place cell increases its firing rate as it approaches the centre of its place field (colour shaded ellipses, intensity represents firing rate). In addition to the change in firing rate, spikes occur at progressively earlier phases of the slow oscillation as the animal traverses a place field. Note that the animal's trajectory is encoded by a sequential activation of place cells.*

is thought to play an important role for precise orchestration of timed firing of neurons and even cross regional synchronisation (Scheffer-Teixeira and Tort, 2016; Tort et al., 2008; Scheffzuk et al., 2011). Along with these findings, there is evidence that the different aforementioned gamma bands are differentially modulated regarding the hippocampal laminae in which they are recorded. For example medium gamma (∼80Hz) is most strongly modulated in *stratum lacunosum moleculare* of CA1 which receives input from entorhinal afferents (Scheffer-Teixeira et al., 2012). On the other hand slow gamma (∼30Hz) is most prominent in *stratum radiatum* indicating that this gamma band is most strongly influenced by Schaffer collateral inputs originating from CA3 (Belluscio et al., 2012; Colgin et al., 2009). These studies have pointed towards external sources supplying inputs to CA1 in a gamma rhythm but recent evidence suggests that CA1 is capable of generating oscillations in the 50-70Hz range independently of CA3 or entorhinal inputs (Butler et al., 2016). As mentioned before, the relative timing of firing of single cells in relation to an underlying theta oscillation is proposed to contain information about the location of an animal in space. Similarly, the activity of anatomically distributed groups of neurons is thought to be organised into distinct 'packages' within a gamma cycle. For instance, prediction of spike times of hippocampal neurons is optimal assuming a time window of 10-30ms (Harris et al., 2003) which corresponds to frequencies between ∼30-100Hz. Since this time window is congruent with the membrane time constant of pyramidal cells (Spruston and Johnston, 1992) and the temporal frame for spike-timing-dependent synaptic plasticity (Magee and Johnston, 1997), the view of gamma oscillations as an internal clock is further emphasised.

The neuronal composition of local networks and the mechanisms by which they achieve gamma synchrony have been extensively studied (Buzsaki and Wang, 2012) and it is widely accepted that GABAergic interneurons are required for rhythm generation. The two most prevalent models of gamma oscillations are the interneuron-gamma (ING) model and the pyramidal-interneuron gamma (PING) model as depicted in figure 1.3.

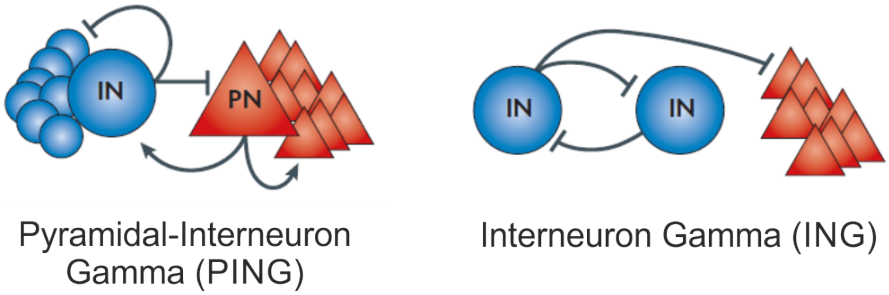

Figure 1.3: Network models of gamma oscillations. *Left: Reciprocal excitatory and inhibitory synaptic connections between interneurons (blue) and pyramidal cells (red) generate oscillations. Right: Mutual inhibition among interneurons elicits an oscillation which is projected onto pyramidal cells. Adapted with permission from Macmillan Publishers Ltd from Bartos et al. (2007)*

Both these models have been developed mostly on the basis of pharmacological experiments. One study in favour of the PING mechanism found that gamma oscillations induced by acetylcholine receptor activation were sensitive to blockade of the glutamatergic α-amino-3-hydroxy-5-methyl-4-isoxazolepropionic acid (AMPA) receptor (Fisahn et al., 1998). Other *in vitro* experiments employing optogenetically evoked gamma oscillations also advocated a PING system for local CA1 gamma (Butler et al., 2016). On the other hand, kainate induced oscillations proved to be AMPA-receptor independent indicating a mechanism not involving excitation from pyramidal cells (Fisahn et al., 2004). However, both models collapse under $GABA_A$ antagonisation thus underlining the importance of inhibition for oscillation maintenance (Fisahn et al., 2004, 1998). It is not entirely clear whether and in what way these two mechanisms compete but a wide range of *in silico* studies have generated supporting evidence for both models (Brunel and Wang, 2003; Whittington et al., 1995; Wang and Buzsaki, 1996; Butler et al., 2016).

In spite of the large variety of GABAergic interneurons in the hippocampus (McBain and Fisahn, 2001; Hu et al., 2014), most of them do not appear to contribute to gamma oscillations with the exception or perisomatic targeting fast spiking basket cells (Buzsaki et al., 1983). These cells are known to establish elaborate axonal branches across whole regions (Lapray et al., 2012) and are interconnected with each other thus allowing them to orchestrate the activity of a large number of pyramidal cells (Mann et al., 2005). Recent studies found that suppressing parvalbumin

(PV, a marker for basket cells) positive interneurons impairs gamma power (Sohal et al., 2009) whereas driving them optogenetically can induce gamma oscillations (Cardin et al., 2009). These findings underline the importance of PV^+ interneurons for the emergence of gamma oscillations.

Taken together, gamma oscillations cooperate with slower frequency bands to coordinate the firing of anatomically dispersed neurons for precisely timed information processing.

1.2.2 Sharp Wave-Ripple Complexes

Another activity pattern that is characteristic for the hippocampus is the sharp wave-ripple complex. SPW-R have been shown to occur in many mammalian species including humans (Buzsaki et al., 2013) and there is increasing evidence that they may act as a vehicle for transferring recent experiences to long-term memory (Girardeau et al., 2009; Ego-Stengel and Wilson, 2010; Buzsaki, 2015). A major physiological difference of SPW-R compared to the previously described theta/gamma oscillations is their irregular, non-rhythmic occurrence (Buzsaki et al., 1983) which is why in early descriptions of these signatures they were called large irregular activity (LIA) (Vanderwolf, 1969) or mini population spikes (Buzsaki, 1986). They can be recorded in the LFP of *stratum radiatum* or *stratum pyramidale* of the CA areas during consummatory behavioural states, i.e. states after which an action has been carried out such as waking immobility, eating or slow-wave (non-REM) sleep (Buzsaki et al., 1983).

As their name suggests, SPW-R mainly consist of two superimposed LFPs of different frequency bands (see figure 1.4). *In vivo*, the sharp wave component is most prominent in the *stratum radiatum* as a negative deflection whereas the ripple oscillation is confined to the *stratum pyramidale* (Girardeau and Zugaro, 2011). Current-source density analyses have shown that during SPW-R, a large current sink is found in the *stratum radiatum* which is accompanied by a source in *stratum pyramidale* (Sullivan et al., 2011). This suggests that the negative signal in *stratum radiatum* originates from excitatory afferents from CA3 which are counterbalanced by positive return currents in *stratum pyramidale*.

The ripple oscillation is characterised by its spindle like appearance in the 150-300Hz frequency band which has its maximal amplitude on the upstroke of the sharp wave. SPW-R episodes occur with an incidence of 0.01-2Hz (with a higher probability during non-REM sleep), last around 30-100ms and contain 3-6 ripple cycles (Buzsaki, 1986). During an SPW-R, single cell activity increases sharply compared to baseline (Bahner et al., 2011) which is probably caused by the increase in network excitability during SPW-R (Buzsaki, 1986; Csicsvari et al., 1999). Indeed, SPW-R represent the most synchronous physiological pattern of activity in the brain which recruits around 10% of hippocampal neurons (Csicsvari et al., 2000).

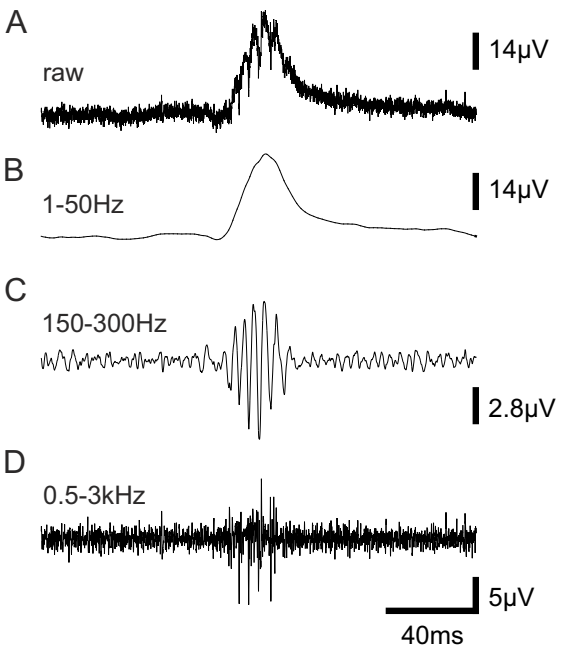

Figure 1.4: Example of a sharp wave ripple complex and its frequency components recorded in vitro. *(A) depicts a wideband recording of an SPW-R recorded in CA1 stratum pyramidale of a mouse hippocampal slice. Its low frequency component is shown in (B). (C) displays a band-pass filtered trace illustrating the superimposed ripple oscillation. (D) shows single unit activity achieved by high-pass filtering.*

As mentioned before, SPW-R play an important role in memory consolidation, a term which describes the formation of long-term memory from recently experienced episodes (McGaugh, 2000; Muller and Pilzecker, 1900). This notion is linked to the observation that especially non-REM sleep is critical for normal memory performance (Walker, 2009). Additional support arose from animal experiments which could show that the same ensembles of hippocampal neurons that had been firing during waking were reactivated in subsequent sleep periods (Wilson and McNaughton, 1994). It was later found using place cell recordings and spatial memory tasks that a sequence of place cells that had been triggered when an animal follows a certain trajectory through space (cf. figure 1.2) is replayed in a time-compressed manner during non-REM sleep (Lee and Wilson, 2002). The first clear evidence that replay of place cell sequences is locked to SPW-R activity was reported in 2007 by Diba and Buzsáki (Diba and Buzsaki, 2007) (schematic shown in figure 1.5). They could furthermore show that replay can occur in reverse order and that place field distance is encoded by the temporal delay between replayed units (Foster and Wilson, 2006). A causal link between expression of SPW-R and mnemonic performance was established by studies showing that rats performed worse in a spatial memory task when SPW-R

had been selectively suppressed during post-learning sleep (Girardeau et al., 2009; Ego-Stengel and Wilson, 2010). There is also correlative evidence for the occurrence of ripples and normal memory consolidation in humans (Axmacher et al., 2008).

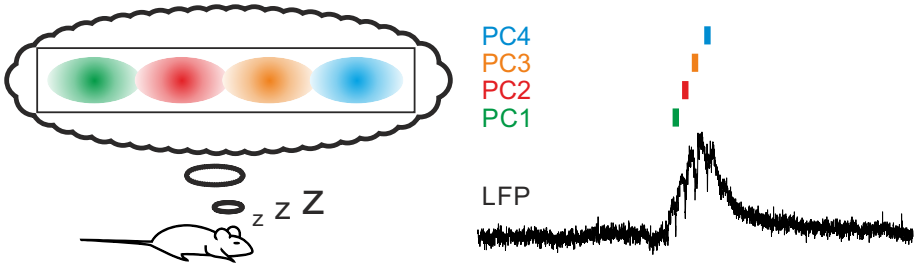

Figure 1.5: Schematic representation of place cell sequence replay during SPW-R. *Recent experiences acquired during ambulatory exploration, for example running across a linear track are consolidated in subsequent consummatory states (e.g. sleep). The sequence of place cells that was triggered by the spatial trajectory of the rat is replayed within an SPW-R episode in a time-compressed fashion.*

To date, many studies have been carried out which were aimed at elucidating the (sub)cellular and network mechanisms underlying the generation of SPW-R. Several different theories have been proposed based on experimental data and *in silico* models. While it is fairly well established that sharp waves are most likely initiated by the autoassociative CA3 network which outputs highly synchronised excitatory synaptic signals onto CA1 (Buzsaki et al., 1983), the mechanisms of ripple generation are less well understood. The two most prevalent models of ripple formation propose either direct interactions between pyramidal cells or reciprocal excitatory and inhibitory synaptic connections between pyramidal cells and GABAergic interneurons. In the former class of models, ripples are thought to originate either from axonal gap-junctions among electrically coupled pyramidal cells (Traub and Bibbig, 2000; Draguhn et al., 1998) or from synchronously propagated inputs in pyramidal cell networks with supralinear dendritic integration (Jahnke et al., 2015). The latter theoretical frameworks propose synaptic interaction between pyramidal cells and inhibitory interneurons as a source for ripple generation (Stark et al., 2014; Ylinen et al., 1995). The observation that ripple oscillations are abolished under blockade of AMPA or GABA receptors underlines this concept (Schonberger et al., 2014). Numerous comprehensive works on the activity patterns of different GABAergic interneurons during SPW-R (reviewed by Somogyi et al. (2014)) have found that perisomatic targeting PV^+ interneurons and bistratified interneurons show the strongest phase-locked increase of firing during SPW-R (Klausberger et al., 2003). In line with these descriptions, current source density analyses provided evidence that GABAergic currents in perisomatic regions of CA1 largely constitute the local current source (Sullivan et al., 2011). Furthermore, Schlingloff et al. (2014) demonstrated that driving PV^+ interneurons optogenetically induces ripples even under

blockade of fast excitatory transmission . Interestingly, it was also shown that light-driven activation of pyramidal cells could also induce ripples *in vivo* (Stark et al., 2014) providing further evidence for pyramidal-interneuron communication as basis for ripple generation.

To sum up, SPW-R can be regarded as a biomarker for cognitive processing and memory formation that is evolutionarily conserved among mammalian species (Buzsaki, 2015).

1.3 The Two-Stage Model of Memory Formation

The idea that long lasting memory content may be formed in a two-step fashion was postulated by György Buzsáki in 1989 (Buzsaki, 1989). Briefly summarised, the theory posits that information such as spatial cues or sensory inputs are actively received during 'on-line' cognitive states in which hippocampal LFPs are dominated by theta/gamma rhythmic activity. This newly acquired content remains labile, i.e. is easily forgotten until it is consolidated during resting, 'off-line' cognitive states such as sleeping in which the hippocampus expresses SPW-R. It is thought that short-term and long-term plastic changes (Bliss and Lomo, 1973) at intrahippocampal and hippocampo-cortical synapses provide the mechanistic framework for the generation of novel memories. More specifically, during theta/gamma periods entorhinal cortical inputs are relayed to CA3 via convergent inputs of granule cells of the DG. Since granule cells are most strongly activated during theta/gamma (Buzsaki et al., 1983), this leads to weak synaptic potentiation of mossy fibre connections. When SPW-R activity takes over, the recurrent excitatory loops of CA3 amplify the previously potentiated synapses and forward this pattern onto CA1 in a highly synchronised manner. The high synchrony is believed to be required to trigger classical forms of long-term synaptic plasticity but also makes the hippocampus the most seizure-prone area in the brain (Buzsaki, 1989). Recent findings showed that learning can cause long-term potentiation (LTP) (Whitlock et al., 2006) and that SPW-R help coordinate synaptic plasticity during place cell consolidation (Sadowski et al., 2016) which supports the hypothesis of SPW-R mediated synaptic plasticity. Another aspect of the two-stage model is concerned with the transfer of information between the hippocampus and neocortical areas. It appears obvious that the hippocampus cannot be solely responsible for the formation as well as the storage of memory due to its limited capacity and comparatively simple structure. Therefore, mnemonic content is believed to be transferred from the hippocampus to cortical stores over time (Girardeau and Zugaro, 2011). While there is conflicting evidence as to whether memory traces can become hippocampus independent (Wang et al., 2009) or remain hippocampus associated (Wiltgen et al., 2010), there is clear

anatomical and functional data supporting hippocampo-cortical interaction (Roth et al., 2016).

A question that is not conclusively addressed in Buzsáki's original publication is the mechanism by which the network switches back and forth between theta/gamma and SPW-R. Buzsáki argued that exploratory theta/gamma is generated by rhythmic cholinergic inputs from subcortical sites to CA3 (Buzsaki, 1989; Buzsaki et al., 1983) which lower the excitability of local pyramidal cells. When the subcortical control is released following termination of exploratory behaviour, recurrent excitation takes over in CA3 and discharges intrinsically generated population bursts that are transmitted to CA1 as SPW-R. While it is still generally accepted that external inputs arising from the medial septum play an important role in theta/gamma generation and maintenance (Fuhrmann et al., 2015; Teles-Grilo Ruivo and Mellor, 2013), it was also shown that complete rat hippocampal preparations are capable of developing theta without septal inputs (Goutagny et al., 2009). However, since acute hippocampal slices (Bahner et al., 2011; Reichinnek et al., 2010) and fornix lesioned animals (Buzsaki et al., 1989) display spontaneous SPW-R, it seems that the default mode of operation in the hippocampus is the SPW-R state.

In conclusion, the two-stage model of memory formation and its experimental support highlight the tightly intertwined relationship of the different oscillatory states of the hippocampus. Nevertheless, many important questions remain open. For example, it is not clear how the neuronal ensembles that participate in different oscillations are selected. It is moreover unclear whether ripple frequency oscillations contribute to downstream processing of information or are merely an artefact of hippocampal topology. Most importantly though, it needs to be clarified how synaptic inputs and coordinated single cell activity leads to the switch of hippocampal network states.

2 Aims of the Study

Within the scope of this thesis, the following questions will be addressed:

- **Establish an *in vitro* system for studying gamma oscillations and SPW-R based on optogenetic tools.** This will prove a highly powerful tool for revealing network and cellular mechanisms which underlie different activity patterns. Optogenetic methods are ideally suited for these investigations as they allow spatiotemporally and cell-specific activation of neurons within the local network.

- **Find means for evoking different patterns of hippocampal activity.** Is it possible to drive a reduced *in vitro* neuronal network into different activity states which can also be observed *in vivo*? If so, are there differences between signals recorded form either paradigm? Also, what are the prerequisites that need to be fulfilled, e.g. how many cells are involved in different activity patterns, are there differences among subregions of the hippocampus?

- **Investigate the mechanisms underlying the switch from the SPW-R network state to gamma oscillations and vice versa.** To date, there is a wealth of knowledge about hippocampal oscillations and their significance for normal brain function. However, information about how hippocampal activity shifts back and forth between different patterns is very limited. More specifically, how is the hippocampus able to switch rapidly between 'on-line' information acquisition during gamma to 'off-line' information consolidation during SPW-R?

3 Materials and Methods

3.1 Materials

3.1.1 Mice

All experiments described here were carried out according to guidelines of the *Federation of European Laboratory Animal Science Associations* (FELASA) and were approved by the state government of Baden-Württemberg (AZ G-188/15).

Male C57/Bl6 mice (Charles River, Sulzfeld, Germany) were used for intracranial vector injections at age P42-P56 and subsequently kept at 21-24°C and 30% relative humidity at a 12h light/dark cycle for 2-4 weeks. Animals were fed *ad libitum* and received fresh litter weekly.

3.1.2 Chemicals

Table 3.1: List of used chemicals

Item	Supplier
$CaCl_2$	AppliChem, Darmstadt, Germany
Cesium-Methanesulfonate	Sigma, Steinheim, Germany
EGTA	Sigma, Steinheim, Germany
Glucose	Merck, Darmstadt, Germany
HEPES	Carl Roth, Karlsruhe, Germany
KCl	AppliChem, Darmstadt, Germany
MgATP	Sigma, Steinheim, Germany
$MgSO_4$	Merck, Darmstadt, Germany
NaCl	AppliChem, Darmstadt, Germany
$NaHCO_3$	Sigma, Steinheim, Germany
NaOH	AppliChem, Darmstadt, Germany

NaH_2PO_4	Grüssing, Filsum, Germany
Normal Goat Serum (NGS)	PAN-Biotech, Aidenbach, Germany
Sucrose	AppliChem, Darmstadt, Germany
Triton X-100	Serva, Heidelberg, Germany

3.1.3 Further Materials and Labware

Table 3.2: List of other materials and labware

Item	Manufacturer
Goat Anti-Mouse IgG - Atto 633 (Cat.No. 78102-1ML-F)	Sigma, Steinheim, Germany
Mouse Anti-NeuN Antibody (Cat.No. MAB377)	Merck Millipore, Darmstadt, Germany
Buprenorphine HCl (0.3mg/ml)	Indivior Eu Limited, Berkshire, UK
Drill Head 0.7mm	Hager & Meisinger GmbH, Neuss, Germany
Lens Cleaning Paper	Tiffen, Hauppauge, USA
Moisturising Eye Ointment	Bepanthen 5% Dexpanthenol Augen&Nasensalbe
Perforated MEA (60pMEA200/30iR-Ti)	Multichannel Systems MCS GmbH, Reutlingen, Germany
Sterile Saline 0.9% NaCl	Braun, Melsungen, Germany
Surgical Suture Thread (Vicryl V734E 4-0)	Ethicon, Norderstedt, Germany

3.1.4 Solutions

Table 3.3: List of used solutions

Solution	Composition
Artificial Cerebrospinal Fluid (ACSF)	in mM: 124 NaCl, 1.8 $MgSO_4$, 1.6 $CaCl_2$, 10 glucose, 1.25 NaH_2PO_4, 26 $NaHCO_3$; pH 7.4 at 37°C (saturated with 95% O_2/5% CO_2)
Phosphate Buffered Saline (PBS)	in mM: 137 NaCl, 2.7 KCl, 10 NaH_2PO_4, 5 NaOH, pH adjusted to 6.8 with 10M NaOH
Pipette Solution for Patch-Clamp Recordings	in mM: 130 Cesium-Methanesulfonate, 2 KCl, 10 EGTA, 10 HEPES, 2 MgATP, 4 NaCl; pH adjusted to 7.3 with CsOH, 295mOsm (adapted from Gan et al. (2017))
Sucrose Solution (30%)	30g sucrose in 100ml 0.1x PBS

3.1.5 Instruments

Table 3.4: List of used equipment

Instrument	Model Description	Manufacturer
Autoclave	D-65	Systec GmbH, Wettenberg, Germany
CCD Camera	ImageM Model C9100-13	Hamamatsu Photonics, Hamamatsu, Japan
Constant Vacuum Pump	CVP	Multichannel Systems MCS GmbH, Reutlingen, Germany
Cryotome	CM1850	Leica Biosystems GmbH, Nussloch, Germany
473nm DPSS Laser	DL473	Rapp Optoelectronics, Hamburg, Germany

515nm DPSS Laser	iBeam smart OEM	Toptica Photonics, München, Germany
Dichroic Mirror	LaserMUX LM01-480-25	Semrock, Rochester, USA
Digital Laser Power Meter	PM100D	Thorlabs, Newton, USA
Digitizer	1401 Power 3	Cambridge Electronic Design, Cambridge, UK
Extracellular Potential Amplifier	EXT 10-2F	npi electronics, Tamm, Germany
Fluorescence Emission Filter	ET535/30M	AHF Analysentechnik, Tübingen, Germany
Heatable Perfusion Cannula	PH01	Multichannel Systems MCS GmbH, Reutlingen, Germany
Heating Plate	ATC-2000	World Precision Instruments, Sarasota, USA
Isoflurane Vaporizer	Halothane Vapor 19.1	Dräger, Lübeck, Germany
Microdrill	K.1070	Foredom Electric, Bethel, USA
Microelectrode Array (MEA) system	USB-MEA60-Up-BC	Multichannel Systems MCS GmbH, Reutlingen, Germany
Micromanipulator (Field Potential Electrode)	MX-4	Narishige, Tokyo, Japan
Micromanipulator (Patch-Clamp)	Model SMX	Sensapex, Oulu, Finland
Microscope Objective	N16XLWD-PF (16x, 0.8NA, 3mm WD)	Nikon, Tokyo, Japan

Microsyringe Pump Controller	SYS-Micro4	World Precision Instruments, Sarasota, USA
Patch-Clamp Amplifier	ELC-03XS	npi electronics, Tamm, Germany
Perfusion Pump	REGLO Analog	Ismatec, Wertheim, Germany
Perfusion Temperature Controller	TC02	Multichannel Systems MCS GmbH, Reutlingen, Germany
Photodiode Power Sensor	S121C	Thorlabs, Newton, USA
Pipette Puller	P-1000	Sutter Instrument, Novato, USA
Shearing Machine	Exacta GT415	Braun Aesculap, Suhl, Germany
Spatial Light Modulator	X10468	Hamamatsu Photonics, Hamamatsu, Japan
Spinning Disk Confocal Microscope	CSU-X1	Yokogawa Electric Corp., Tokyo, Japan
Stereotaxic Frame		Stoelting Co., Wood Dale, USA
USB Camera	uEye SE	IDS Imaging Development Systems GmbH, Obersulm, Germany
Vibratome	Leica VT1000S	Leica Biosystems GmbH, Nussloch, Germany
Widefield Fluorescence Microscope	BX61	Olympus, Hamburg, Germany

3.1.6 Adeno-associated Viral Vectors and Optogenetic Tools

Adeno-associated viruses (AAVs) were commercially purchased from the vector core facility of the University of North Carolina (available at: `http://genetherapy.unc.edu/services.htm`). The vectors were shipped on dry ice and delivered as ready-to-use 100μl aliquots. Viruses were dispensed in 350mM NaCl+5% D-Sorbitol in PBS with titers of $4x10^{12}$ virus genomes/ml. The viral construct used for the experiments described here (AAV5-CaMKIIα-hChR2(H134R)-EYFP) encodes a mammalian codon optimised channelrhodopsin2 -EYFP fusion protein under the control of the Calmodulin kinase II alpha (CamKIIα) promoter packaged in a serotype 5 AAV. This serotype is known to possess a predominantly neural tropism making it particularly well suited for efficient transduction of hippocampal tissue (Burger et al., 2004). It has furthermore been shown to spread across a larger volume compared to other serotypes when injected directly into the brain (Watakabe et al., 2015; Aschauer et al., 2013). The use of AAVs did not lead to any noticeable immune responses in mice as has been shown in several studies (Rogers et al., 2011; Zaiss et al., 2002).

As the CaMKIIα promoter is primarily active in principal neurons (Wang et al., 2013), this leads to a widespread and robust expression of the transgene in pyramidal cells of the hippocampus. Codon optimisation of channelrhodopsin2 improves expression in mammalian systems (Boyden et al., 2005; Gradinaru et al., 2007; Lin et al., 2009) whereas the amino-acid substitution (H134R) enables larger photocurrents combined with slightly slower off kinetics compared to other variants of channelrhodopsin (Lin et al., 2009; Nagel et al., 2005).

3.2 Methods

3.2.1 Intracranial Delivery of Viral Vectors

For analgesic purposes, the animals received a subcutaneously applied dose of buprenorphine at 0.1mg/kg 30-45 minutes preoperatively. Bilateral intracranial virus injections were carried out under isoflurane anaesthesia (4% preoperatively, 1.5-2.5% perioperatively). During the operation, the animal's body temperature was regulated by a heating plate set to 37°C to prevent hypothermia. The animal's eyes were covered with moisturising ointment. The depth of anaesthesia was regularly checked by observing the breathing frequency and checking for loss of toe pinch reflex.

The animal's head was shaved and its scalp disinfected with 70% EtOH followed by exposure of the skull with an incision along the sagittal midline of about 1cm length. The area was held open by restraining the skin flaps to the side with surgical threads (Vicryl V734E 4-0, Ethicon, Germany). The underlying connective tissue was moved aside using cotton buds soaked in 0.9% saline. Next, the coordinates of the bregma and lambda were determined and noted. The position of the head was adjusted if it was tilted along either the lateral-medial or the anterior-posterior axis. The coordinates of the target brain region, in this case the ventral hippocampal CA3 region (relative to bregma: AP -2.8, LM ±3.2, DV -3.3/-3.1/-2.9, see figure 3.1) were drawn on the skull. The bone above the injection sites was thinned using a dental drill with a 0.7mm tip (Hager & Meisinger GmbH, Germany). The microsyringe was then loaded with the virus suspension and its tip was lowered through the thinned skull to the desired position. A volume of 1.2-1.5μl was injected evenly distributed at the

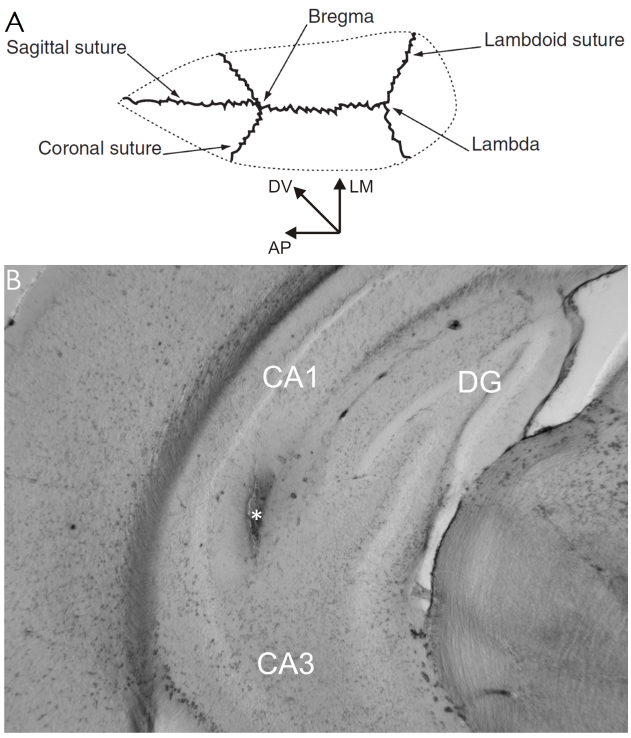

Figure 3.1: Location of intracranial virus injection. *(A) Schematic drawing of the bone sutures of a mouse skull viewed from dorsal. Bregma and lambda as reference points are indicated. Axis directions are shown at the bottom: AP: anterior-posterior, DV: dorsal-ventral, LM: lateral-medial. Adapted with permission from Macmillan Publishers Ltd from Cetin et al. (2006). (B) Coronal section through a mouse brain indicating the injection site between CA3 and CA1 marked by an asterisk.*

three dorsoventral depth coordinates at 200nl/min (SYS-Micro4, World Precision Instruments, USA). The virus was allowed to diffuse into the brain tissue for 10min before withdrawing the syringe.

Finally, the skin flaps were stitched together and the animal was allowed to recover for several hours under an infrared heating lamp set to 32°C with regular monitoring. An additional dose of buprenorphine was administered 4-6h postoperatively. Mice were predominantly operated in pairs, meaning that two mice which were kept in the same cage after birth were submitted to injections and also subsequently put in the same cage in order to grant sufficient social exposure. Mice were kept in the animal facility for 2-4 weeks to ensure sufficient expression of the transgene before use in slice experiments.

3.2.2 Preparation of Acute Hippocampal Brain Slices

Virus injected mice were transferred to an anaesthesia chamber which was gradually flooded with CO_2 until a reduction of breathing frequency and loss of righting reflex set in. The animal was then quickly decapitated and its head was immediately immersed in ice cold (<4°C) ACSF. The brain was swiftly removed from the skull socket and stored in ice cold ACSF gassed with carbogen ($95\%O_2/5\%CO_2$). The cerebellum as well as a third of the rostral brain were removed. To obtain horizontal slices, a thin part of the dorsal parietal cortex was cut and the brain was glued to the cutting stage with the ventral portion facing upwards using instant adhesive. The cutting chamber was carefully filled with gassed, ice cold ACSF and slices of 400μm thickness were produced (Leica VT1000S, Germany) and the hemispheres were separated. The obtained slices were transferred to and interface style holding chamber for a recovery time of at least 2h. In this chamber, the slices were supplied with a constant flow (∼1.5ml/min) of ACSF and warmed to 32±1°C in a carbogen atmosphere. These conditions allow the slice to generate spontaneous SPW-R oscillations.

3.2.3 Microelectrode Array Recordings

Following the recovery period, the slices were briefly checked for spontaneous SPW-R activity by placing a glass electrode connected to a field potential amplifier (EXT10-2F, npi, Germany) into the pyramidal cell layer of CA1. If a slice displayed reliable SPW-R, it was transferred to a perforated MEA chamber (USB-MEA60-Up-BC & 60pMEA200/30iR-Ti, Multichannel Systems, Germany) in which they were perfused with gassed ACSF at 4-5ml/min. The perforation of the MEA allowed for perfusion from both sides of the slice which granted improved supply of nutrients and oxygen (see figure 3.2). Together with the high perfusion rate, these conditions were necessary and sufficient for the slice to maintain spontaneous SPW-R activity in submerged conditions (Maier et al., 2009; Hajos et al., 2009). The upper perfusion was generated by a perfusion pump (REGLO Analog, Ismatec, Germany) while the lower perfusion was achieved by a combination of gravity driven flow as well as a constant vacuum pump (CVP, Multichannel Systems, Germany). The negative pressure generated by the vacuum pump was furthermore used to draw the slice towards the electrodes of the MEA. Temperature in the chamber was set to 32°C and maintained by perfusion heating elements (PH01, Multichannel Systems, Germany). In these conditions, the slices reliably exhibited sustained spontaneous SPW-R activity over the course of several hours. Extracellular field potential data was sampled at 25kHz from 60 electrodes (30μm diameter, 200μm spacing) covering the entire hippocampal area and stored on a PC.

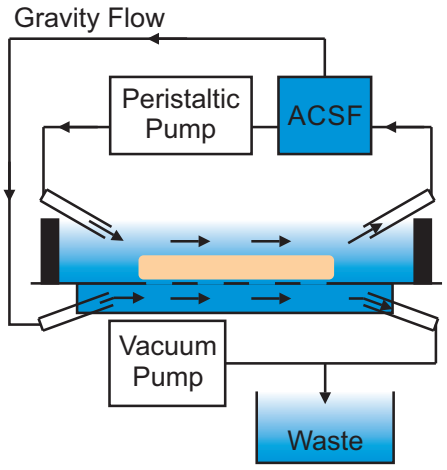

Figure 3.2: Schematic of double perfusion using a perforated MEA. *The slice is positioned in the middle of the MEA above the perforations. Note that the upper perfusion is recycled whereas the lower is discarded.*

3.2.4 Development of a Holographic System for Imaging and Optogenetics

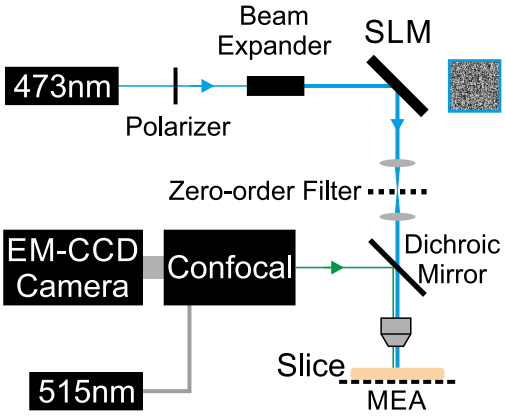

Figure 3.3: Schematic of the setup used for imaging and optogenetics. *The beam of the 473nm laser is shaped by the phase image displayed on the SLM and projected towards the slice. Transgene expression was imaged through a confocal microscope using a 515nm laser.*

A major part of this work consisted of implementing a holographic illumination system based on a spatial light modulator (SLM) for targeted, region-specific illumination of the slice network. The working principle of SLMs involves modulating the phase of the incident light so that the intensity pattern of the desired image is a result of the wave front modulation (Papagiakoumou et al., 2010; Neff et al., 1990). The SLM model used here (X10468, Hamamatsu Photonics, Japan) achieves this with liquid crystals on a silicon substrate which can adjust light phase depending on the applied voltage. This functional principle is very similar to a typical LCD computer display.

A schematic illustration of the illumination and imaging setup is shown in figure 3.3. The beam of a 473nm diode-pumped solid state laser (DL473, Rapp Optoelectronics, Germany) is run through a 90° polarisation filter and then expanded to a diameter of 20mm. The polarisation filter is needed because the liquid crystals of the SLM require a certain angle of polarisation for phase modulation (Hu et al., 2010). The expanded beam covers the aperture of the SLM and is reflected from there along an infinity ray path. Since the SLM is composed of individual pixels arranged in a grid, this causes unwanted diffraction effects which contaminate the holographic image (Zhang et al., 2013). The most prominent component of this diffraction pattern, the 0^{th} order is removed from the hologram by simply focussing the beam to create a virtual image and placing a glass coverslip with a black dot in the centre of beam path. Since the diffracted light is not phase modulated, it is in a different phase plane thus allowing elimination of the 0^{th} order without interfering with the hologram. After removal of the 0^{th} order, the ray path is again converted to parallel light using a tube lens and focussed through a microscope objective towards the slice.

For controlling the imaging and holographic illumination setup, a custom graphical user interface was developed in MATLAB by Felix Friedl, Martin Both, Jan-Oliver Hollnagel, Martin Kaiser and Pascal Geschwill. The software allows live image acquisition using MATLAB drivers for the EM-CCD camera (C9100-13, Hama-

matsu, Japan) provided by Hamamatsu and definition of a freely drawn area of illumination (AOI). The drawn illumination pattern is Fourier transformed and the resulting phase image is displayed on the SLM through a digital visual interface. The MATLAB algorithm for generating the phase image is based on the Gerchberg-Saxton algorithm which involves (inverse) Fourier transforms (Gerchberg, 1972). In addition to generating a two-dimensional illumination pattern, the SLM system can emulate a virtual fresnel lens which allows shifting the pattern in z-direction. Intensity, profile (sinusoidal, square pulse, ramp) and time courses of optogenetic stimulation were controlled via transistor-transistor-logic (TTL) inputs using a power1401 digital/analog converter (CED, Cambridge, UK) and the stimulus generator included in the accompanying Spike2 (v7) software.

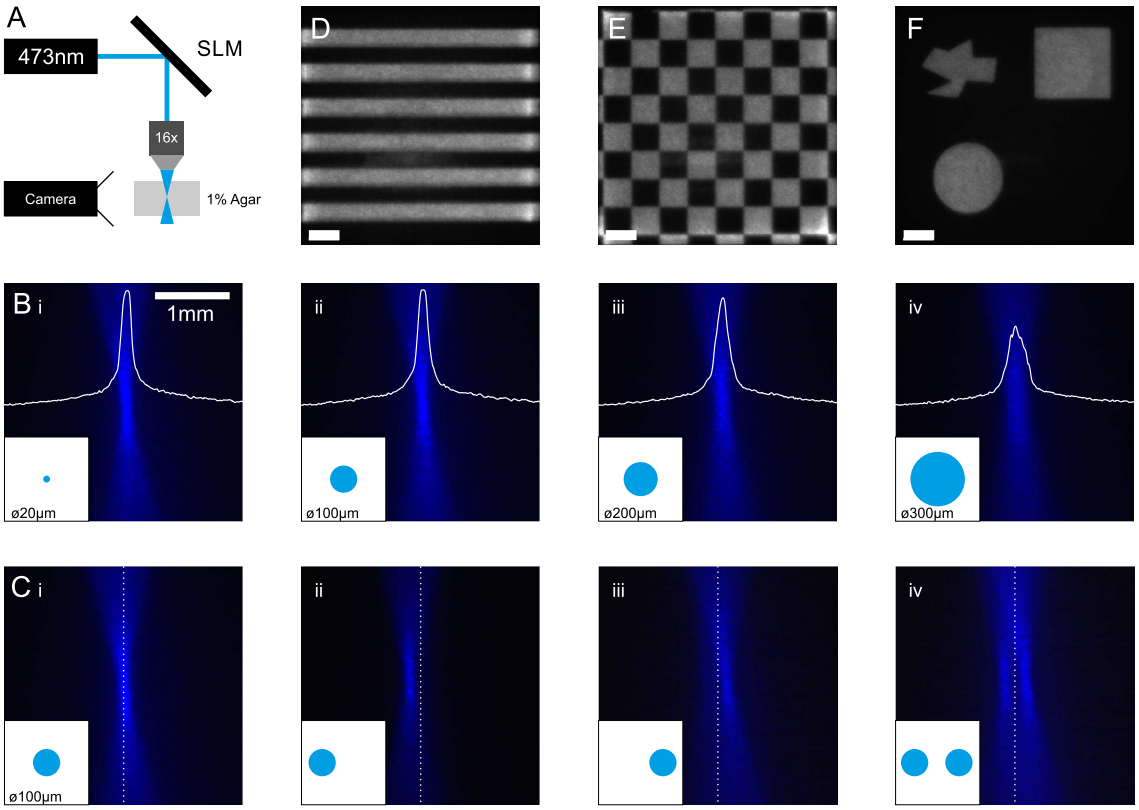

Figure 3.4: Laser beam shaping using a spatial light modulator. *(A) Schematic diagram of the image acquisition setup used to capture images shown in (B) and (C). A 473nm laser beam was directed towards the SLM displaying an image which was focussed through a 16x microscope objective towards a 1% block of Agar. A camera was positioned so that the shape of the beam could be observed. (B) Varying diameters of holographically projected circles directly influenced beam diameter and intensity at the focal point. White curves represent horizontal line scans through the focal plane. (C) Shifting the position of the circle in x/y direction within the field of view allowed controlling the position of the focal point. Dashed line indicates the vertical image centre line. Scale bar in (Bi) applies to all images in (B) and (C). (D-F) Examples of generated patterns and shapes projected onto a fluorescent probe and imaged through a confocal microscope. Scale bars in (D-F) 50µm.*

An overview of the beam shaping characteristics of the holographic illumination system is shown in figure 3.4. As displayed in figure 3.4 (B) the overall size (in this case a circle) of the computer generated hologram directly influenced the diameter of the resulting beam. Note also that the intensity at the focal point was inversely proportional to the diameter of the generated circle. This is because the light reflected from the SLM is distributed across the entire AOI. A smaller AOI is thus illuminated with a higher intensity compared to a larger area at constant laser power. This property is a fundamental improvement over digital micromirror device (DMD) based pattern illumination as it grants much higher light efficiency. The possibility of shifting the position of the AOI dynamically and even generating more than one AOI within the field of view is displayed in figure 3.4 (C). This facilitates optogenetic stimulation of several hippocampal subregions at the same time or changing the AOI freely during an ongoing experiment. The system is capable of generating either predefined patterns such as grids and checkerboards as well as freely drawn shapes like circles, rectangles and polygons as shown in figure 3.4 (D-F). The possibility of creating a freely adjustable beam shape was particularly useful when the AOI should be adapted to the curved shape of the CA area of the hippocampus.

In a typical experiment, the slice was placed in the MEA chamber and the expression of the ChR2-EYFP fusion protein was assessed using a spinning-disk confocal microscope (CSU-X1, Yokogawa, Japan) and a 515nm laser (iBeam smart, Toptica Photonics, Germany). Using a 16x submersible microscope objective (N16XLWD-PF, Nikon, Japan), a field of view of 430x430μm was visible. If expression levels were deemed sufficient and widespread, a subregion of the hippocampal area was selected and outlined in the MATLAB graphical user interface. A computer generated hologram of the outlined area was calculated and displayed on the SLM which then limits optogenetic stimulation to the AOI.

3.2.5 Patch-Clamp Recordings

Blind whole-cell patch-clamp recordings were carried out using pipettes of 2.5-4MΩ resistance which were advanced through the pyramidal cell layer of CA1 with positive pressure applied. A Gigaohm seal was formed by releasing pressure and applying light suction to the electrode after an increase in series resistance was detected which indicates the presence of a cell soma. Recordings were performed with a ELC-03XS amplifier (npi, Germany) and digitised at 20kHz with a power 1401 ADC (CED, Cambridge, UK) controlled by Spike2 (v7) and Signal4 software (CED, Cambridge, UK). The liquid junction potential was calculated to +10mV using JPCalc (Barry, 1994). Voltage clamp recordings of IPSCs were done with +10mV holding potential

and EPSCs were recorded at -74mV (chloride reversal potential was calculated to be around -82mV).

3.2.6 Immunohistochemical Staining

For immunohistochemical analyses, slices were chemically fixed by overnight storage in 4% paraformaldehyde (PFA) at 4°C. Slices were the incubated in 30% sucrose solution in phosphate buffered saline (PBS) at 4°C and subsliced to 25μm thickness at -25°C using a cryotome (CM1850, Leica, Germany). Slices were washed 3x5min in PBS and then blocked for 90min using 5% normal goat serum (NGS) and 0.3% triton in PBS. Subsequent incubation with the primary antibody (Mouse Anti-NeuN, dilution 1:1000 in 1%NGS/PBS+0.2% Triton in PBS) was carried out over night at room temperature. After washing the slices 3x5min in PBS, they were incubated with the fluorescent secondary antibody (Anti-Mouse IgG - Atto 633, dilution 1:1000 in 1%NGS/PBS+0.2% Triton) at room temperature for 90min. After an additional washing step with PBS, the slices were stained with DAPI (dilution 1:10000 in distilled water) and finally washed again with distilled water before they were mounted onto microscope slides. Slices were imaged using an upright fluorescence microscope (Olympus BX61, Hamburg, Germany).

3.2.7 Data Analysis

Data analysis was carried out offline using custom written MATLAB code based on the Neuroshare MATLAB API [1] for reading and processing multichannel data (.mcd) files generated by the MEA software (MC_Rack, Multichannel Systems GmbH, Germany).

Analysis of network oscillations was primarily based on complex morlet wavelet transforms which are part of MATLAB's wavelet toolbox (`cmor1-1.5`). This allowed for frequency analysis in the time domain as well as in the frequency domain. Briefly, raw data were downsampled by a factor of 10 and were transformed using the aforementioned wavelet. The resulting time-frequency plot was smoothed with a gaussian kernel and normalised to the maximum power value. Oscillation power is displayed in a colour code with brighter colours representing higher power and frequency components indicated on the y-axis.

Analysis of unit firing was achieved by high-pass filtering (3kHz) raw traces using a fourier-transform based filtering algorithm and determining time points of units with a thresholding algorithm. Single units are more easily detectable in high-pass filtered traces due to their very fast time courses. The detection algorithm was

[1] http://neuroshare.sourceforge.net/Matlab-Import-Filter/NeuroshareMatlabAPI-2-2.htm

adapted from the Leventhal Lab at the University of Michigan[2]. It is based on calculation of the smoothed nonlinear energy (SNLE):

$$\Psi[x(n)] = x^2(n) - x(n+1)x(n-1) \tag{3.1}$$

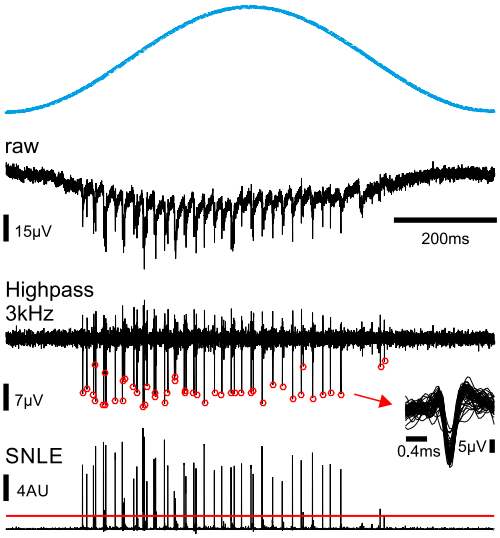

Figure 3.5: Unit detection based on calculation of smoothed non-linear energy. *Raw trace (top) is high-pass filtered at 3kHz (middle) and its SNLE is calculated (bottom). A threshold is then applied (red line) to extract time points and wave forms of units. Detected units are marked with red circles.*

Calculation of SNLE both increases signal-to-noise ratio by subtracting neighbouring datapoints and also removes negative potentials by squaring the signal before applying a threshold for unit detection. The workflow for unit detection is shown in figure 3.5: the raw trace recorded during optogenetic stimulation is filtered and the SNLE of the filtered trace is calculated (see bottom trace). From this SNLE trace, a threshold is calculated at two times (default value) the standard deviation of event-free baseline noise. The time points of threshold crossing are used to extract the units from the high-pass filtered trace (shown in the inset of figure 3.5). The quality of unit detection was checked by visual inspection and the threshold multiplier was adjusted if necessary to minimise false positives.

Data are either presented as mean±standard error of the mean (SEM) or as box plots in which the median is presented as a white dot (see figure 4.11) or black line (see figure 4.10) and the box limits represent the 25$^{\text{th}}$ and 75$^{\text{th}}$ percentile. Whiskers of box plots indicate data range within $\pm 2.7\sigma$ of the distribution.

Peaks and troughs of both gamma and ripple oscillations were detected by using a Hilbert transformation of previously filtered data and calculating its phase angle. Cross correlations and time lags of gamma oscillations were calculated using MATLAB's `xcorr` function.

Descriptive circular statistics were carried out using a circular statistics toolbox for MATLAB written by Philipp Berens[3]. Polar plots of unit firing relative to the phase of sinusoidal stimulation (as shown in figure 4.11) were produced from unit phase angles and illustrated with MATLAB's `polarhistogram` function. The mean

[2]https://github.com/LeventhalLab/EphysToolbox/blob/master/SpikeySpike/ getSpikeLocations.m

[3]https://de.mathworks.com/matlabcentral/fileexchange/10676-circular-statistics-toolbox–directional-statistics-

angle of firing was calculated using custom MATLAB algorithms. Statistical significance was assessed using GraphPad InStat (Version 3.10). The specific statistical tests and p-values are reported in the text accompanying the data.

Cell numbers in immunostained hippocampal slices were assessed by hand using the Cell Counter plugin[4] for ImageJ (Version 1.50i).

Synaptic currents (IPSCs/EPSCs) were detected from five trials of ramp stimulation per cell based on a deconvolution algorithm (Roth et al., 2016). The traces are filtered with a 200Hz fourier transform based low pass filter which is then deconvolved with a kernel resembling a typical postsynaptic current. After that, individual events were identified by threshold detection.

3.2.8 Contribution of Others

The experiments and analyses described here required the use of a broad range of methods which involved the assistance of many different people beyond the author of this thesis. In this section, the individual contributions of these colleagues shall be mentioned in a comprehensive manner.

All data shown here was collected within the group of Prof. Dr. Andreas Draguhn at the Institute for Physiology and Pathophysiology of the University of Heidelberg. In addition to providing equipment and lab space, Prof. Dr. Andreas Draguhn was involved in conceptual scientific supervision and design of experiments.

Dr. Martin Both acted as immediate project adviser and was directly engaged in the design and implementation of the holographic illumination system. He also provided technical support for slice recordings along with Dr. Claus Bruehl. Furthermore, he wrote the original wavelet transformation algorithms which were adapted by Pascal Geschwill.

The actual installation and adjustment of the holographic illumination system was carried by joint efforts of Dr. Martin Both, Martin Kaiser, Dr. Felix Friedl and Pascal Geschwill. Additionally, they accomplished the development of a graphical user interface for controlling the system (i.e. fluorescence image acquisition, laser controls and holographic pattern generation) which was aided by Dr. Jan-Oliver Hollnagel.

Intracranial virus injections were performed by either Katja Lankisch or Pascal Geschwill. Acquisition of wide field fluorescence images (see figure 4.17) was aided by Justus Schneider who executed cryotome subslicing and antibody staining as well as Nadine Zuber and Tina Sackmann who provided technical assistance for the fluorescence microscope.

Unless otherwise stated, electrophysiological recordings and the accompanying

[4]https://imagej.nih.gov/ij/plugins/cell-counter.html

data analysis shown here were carried out by Pascal Geschwill. Design of figures displaying experimental results was done by Pascal Geschwill. Exemplary raw data used for illustrative purposes were kindly provided by Dr. Vivan Nguyen-Chi (figure 4.3 (C) and (G)) and Dr. Jan-Oliver Hollnagel (figure 4.3 (A))

4 Results

4.1 Reversible Induction of Gamma-Band Oscillations and Sharp Wave-Ripple Complexes by Different Stimulus Profiles

Acute hippocampal slices expressing ChR2-EYFP under the control of the CamKIIα promoter were placed onto the MEA in submerged conditions. They reliably displayed spontaneous SPW-R at a frequency of 0.6±0.3Hz (mean±standard deviation (STD) 71 slices, 23 mice) which could be recorded over the course of several hours (see figure 4.1 (E)). Slices were placed such that the MEA electrodes could pick up signals from as large an area of the hippocampus as possible. The expression pattern of the transgene was assessed and using a confocal image, a subfield of the slice was outlined and defined as AOI. Stimulating the pyramidal cell layer of the CA3a region with a 5ms square pulse evoked a field potential in downstream CA1 which closely resembled spontaneous SPW-R (figure 4.1 (C)). Both evoked and spontaneous SPW-R displayed a prominent frequency component at 200-250Hz (figure 4.1 (F) and (G)). During prolonged sinusoidal light intensity courses at the same AOI, slices generated field potential oscillations in the 30-60Hz band (figure 4.1 (D) and (H)) which also travelled through the hippocampal network.

Interestingly, evoked activity not only spread to downstream regions of CA3 but also backpropagated to upstream areas in the hilus and DG where it resulted in a population spike resembling field potential when a 5ms rectangular pulse was applied. The negative potential deflection recorded in regions adjacent to the AOI can be explained by the influx of cations into the stimulated neurons through ChR2 which leads to an extracellular negativity. Optogenetically evoked gamma oscillations quickly disappeared when sinusoidal stimulation stops after which the slice returns to generating SPW-R spontaneously. This indicates that the "default" network state of hippocampal slices is the SPW-R state and that gamma oscillations only emerge in presence of external stimulation. This observation agrees with several postulated hypotheses about the emergence of SPW-R within hippocampal networks (Buzsaki et al., 1983; Buzsaki, 2015).

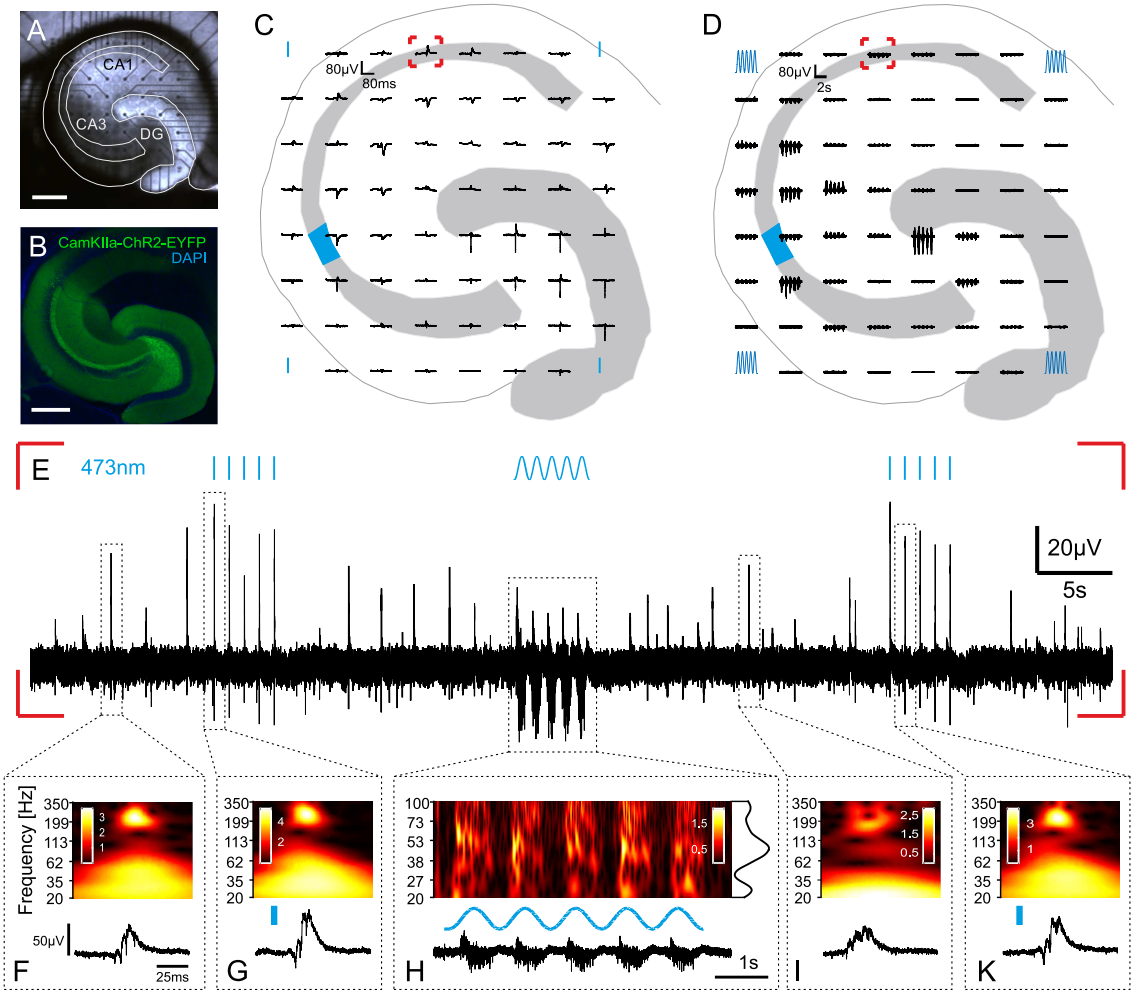

Figure 4.1: Reversibly Evoking distinct network activity patterns by different stimulus modalities. *(A) Overview light microscopic image of a hippocampal slice on a MEA. The subfields of the slice are outlined for clarity. Underlying extracellular electrodes span nearly the entire hippocampal formation. (B) Fluorescence micrograph of typical widespread ChR2-EYFP expression pattern. Scale Bars in (A) and (B) are 400µm. (C) Field potential responses recorded from 60 electrodes following stimulation with a 5ms laser pulse. The targeted area of illumination in CA3a is highlighted in blue. Note that the activity spread throughout the whole hippocampus. (D) same as in (C) but stimulation intensity following a sine wave. (E) Raw data recorded from the marked electrode in (C) and (D). In addition to spontaneous SPW-R, the slice generated signatures resembling SPW-R in CA1 upon delivery of 5ms laser pulses to CA3a. Sinusoidal stimulation evokes gamma band activity. Note that the slice returned to SPW-R state upon cessation of sinusoidal stimulation. (F-K) Enlarged views of the framed segments in (E). Top: wavelet spectra showing frequency components. Bottom: raw trace. (H) The network generated gamma band activity with a peak at ∼50Hz (mean of wavelet spectrum is shown as black line). Temporal scale bar in (F) applies to (G),(I) and (K).*

The propagation of evoked activity through the slice network is illustrated in figure 4.2. Interestingly, the evoked field potential in the upstream DG/hilus region usually displayed a very sharp downward deflection in response to a 5ms light flash (figure 4.2 (B)). This indicates that the backpropagated signal is not transmitted via a synaptic connection but rather consists of backpropagated synchronised action

potentials (population spikes). Backpropagation of light flash induced population spikes was successful in 88% (30/34 slices, 11 mice) of the slices while evoking an SPW-R was successful in 97% (33/34) of the slices. The transmission delay between CA3 and CA1 from stimulus onset to the peak of the evoked SPW-R was 21.3±5.7ms (761 SPW-R, 33 slices, 11 mice) whereas the delay between CA3 and the DG from stimulus onset to the peak of the evoked population spike was 8.3±1.2ms (942 population events, 30 slices, 11 mice). The lag between gamma cycles in CA3 and CA1, as assessed by cross correlation, was 5.4±6.3ms at 1Hz stimulation frequency (16 slices, 7 mice). These values stand in good accordance to published values of transmission velocities between CA3 and CA1 (Both et al., 2008).

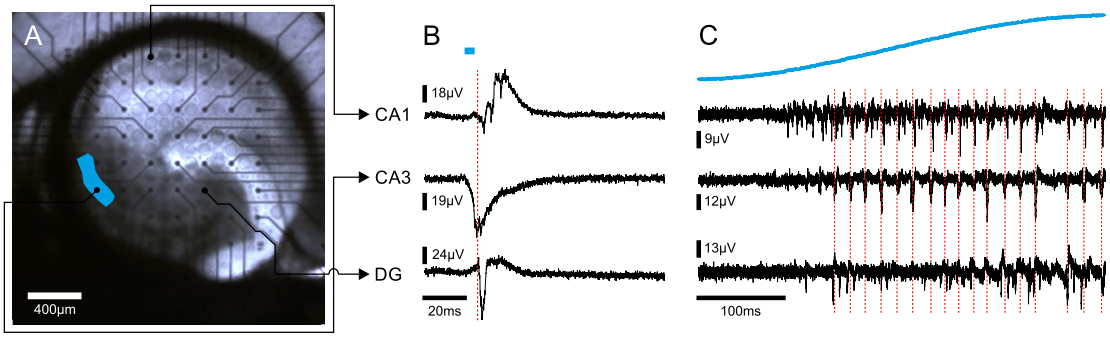

Figure 4.2: Propagation of evoked activity through the slice network. *(A) Light microscopic image of a hippocampal slice on a MEA. Illuminated area in CA3a is marked in blue. (B) Evoked activity in different regions of the hippocampus in response to a 5ms square pulse of light. Note the delay between the evoked peak at the stimulation site (CA3) and the downstream (CA1) or upstream (DG) sites. (C) Evoked activity in different regions of the hippocampus in response to the upstroke of a 1Hz sinusoidal light stimulation. Troughs of evoked gamma oscillations in CA3a are marked by red dashed line.*

A qualitative comparison of the optogenetically evoked gamma oscillations with other in *in vitro* and *in vivo* paradigms revealed that the leading frequencies of optogenetic gamma and *in vivo* gamma almost perfectly overlap (figure 4.3 (D)). This indicates that similar underlying mechanisms are recruited. Interestingly, while gamma oscillations *in vivo* are nested into underlying theta waves (figure 4.3 (C)), optogenetically evoked gamma appeared "pure" without an accompanying slower oscillation. A typical pharmacological paradigm for induction of gamma oscillations *in vitro* employing 10μM acetylcholine and 2μM physostigmine (Hollnagel et al., 2015) on the other hand induces oscillations at ∼30Hz (figure 4.3 (A)). This implies that cholinergic terminals which are strongly activated by the aforementioned pharmacological intervention appear to be irrelevant for generation of optogenetic gamma.

Comparing spontaneous and optogenetically evoked SPW-R recorded *in vitro* exposed a striking similarity in terms of frequency components and overall morphology (figure 4.3 (E) and (F)). The ripple frequency component was furthermore very similar to an *in vivo* situation (figure 4.3 (G)) although signals differed in overall morphology. It appears from the power spectrum shown in in figure 4.3 (H) that the ripple frequency peak *in vivo* is shifted towards lower frequencies compared to *in vitro* data. This difference is however well described in the literature (Sullivan et al., 2011) and is possibly caused by the reduced complexity of the slice network (Buzsaki, 2015).

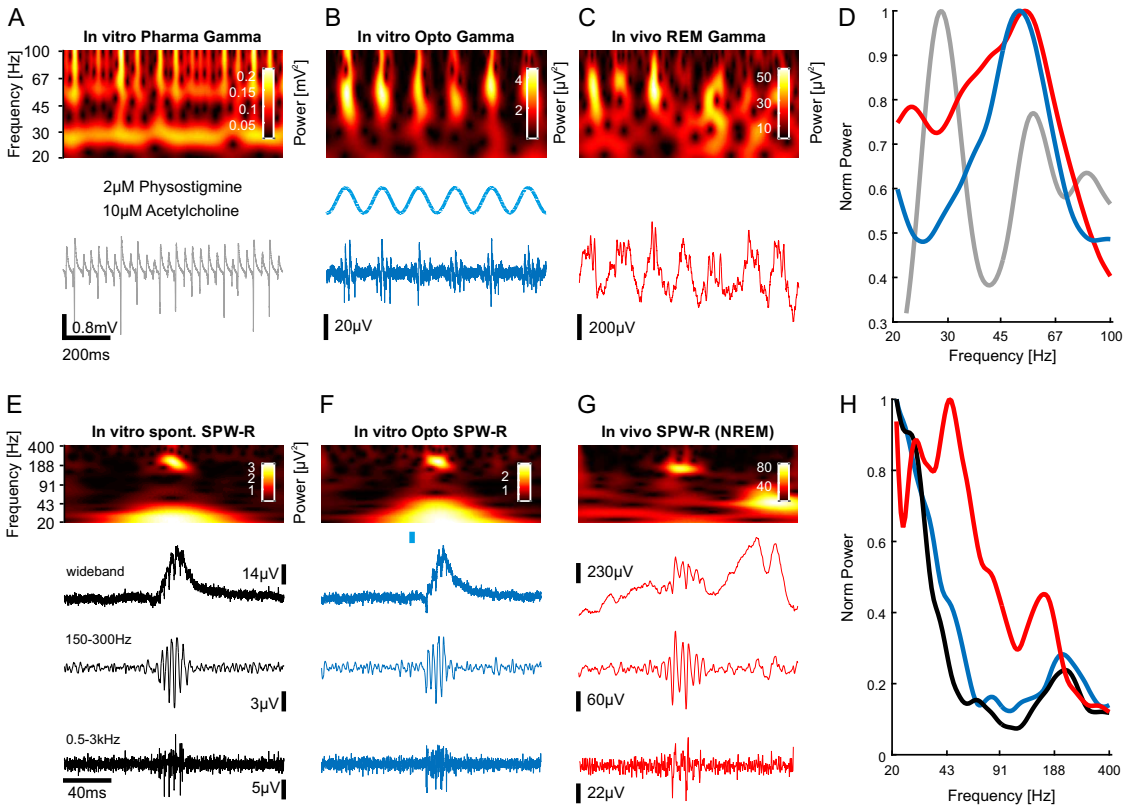

Figure 4.3: Qualitative comparison of optogenetically evoked network patterns with other paradigms. *(A) Representative field potential data recorded from a rat hippocampal slice incubated with 10μM acetylcholine and 2μM physostigmine. (B) Example trace of optogenetically evoked gamma by stimulation with a 5Hz sinusoidal intensity time-course recorded from a mouse slice. (C) In vivo recording of theta/gamma activity during REM sleep. Data in (A-C) was recorded from CA1 pyramidale. (D) Power spectra of data shown in (A-C) display overlapping peaks at 50Hz of optogenetic and in vivo gamma. (E-G) Comparison of frequency components of an in vitro spontaneously occurring SPW-R (E) with an optogenetically evoked one (F) and an SPW-R recorded in vivo during NREM sleep (G). Raw data is bandpass and highpass filtered to reveal ripple frequencies and unit activity. (H) Power spectra of data shown in (E-G) display overlapping peaks at 200-250Hz. Data in (A) kindly provided by Jan-Oliver Hollnagel. Data in (C) and (G) kindly provided by Vivan Nguyen-Chi.*

In conclusion, hippocampal slices are capable of producing two of the most prevalent network patterns of the hippocampus which also occur *in vivo*. Depending on the optogenetic stimulus modality, the network responded with either gamma oscillations (sinusoidal stimulation) or SPW-R (5ms square pulse).

4.1.1 Power and Frequency of Evoked Gamma Depend on Stimulation Intensity

As a subsequent step, the properties of optogenetically evoked signals were thoroughly characterised. Firstly, the input/output relationship between laser intensity and power as well as frequency of the resulting gamma band oscillation was described. This paradigm was carried out with different stimulation/recording configurations in order to find any possible differences in locally or distally generated oscillations. Therefore, slices were stimulated with a 1Hz sinusoidal stimulation profile lasting 5s with intensity maxima ranging from 1-5mW/mm^2.

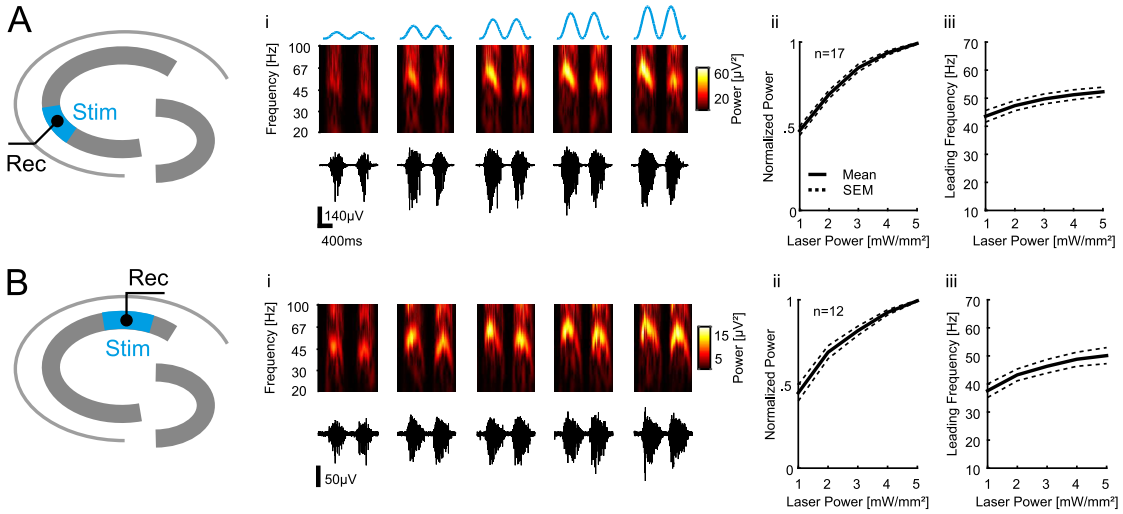

Figure 4.4: Input/output relationship between laser intensity and resulting power and frequency of resulting locally generated gamma. *(A) Schematic illustration of the stimulation/recording configuration. AOI was limited to CA3 pyramidale and a recording electrode in the same area was picked for analysis. (Ai) Bottom: Example traces showing gamma activity in response to increasing laser intensity. Top: Corresponding wavelet spectra revealing frequency distribution. (Aii) Oscillation power normalized to maximum value as a function of laser intensity. (Aiii) Oscillation frequency as a function of laser intensity. Data in (Aii) and (Aiii) were recorded in 17 slices from 4 mice. (B) same as (A) but with stimulation/recording in CA1. Data in (Bii) and (Biii) were recorded in 12 slices from 4 mice.*

As is evident from figure 4.4, the dynamic range of locally generated oscillations in CA3 and CA1 depended on the laser intensity according to a saturation curve. Therefore, using the illumination system described here, the network could be driven to almost its maximally possible activity level. Interestingly, not only the power of

evoked gamma but also its frequency depended on illumination strength, although the effect is very moderate (see figure 4.4 (Aiii) and (Biii). Possible explanations for this observation are given in the discussion.

As displayed in figure 4.1 (D), applying optical stimulation to CA3 not only induced a field potential in the vicinity of the AOI, but also caused the signal to be propagated towards both upstream (DG) and downstream (CA1) regions. The input/output characteristic of these transmitted oscillations is summarised in figure 4.5. As shown in figure 4.5 (A), the power of gamma oscillations which are propagated from CA3 to CA1 also depended on input strength, albeit to a lesser extent as locally generated gamma. The leading frequency also followed a similar course in response to higher light intensity. An examination of gamma backpropagated from CA3 to DG (seen in figure 4.5 (B)) revealed a largely linear input/output relationship concerning gamma power whereas frequency remained relatively stable. Interestingly, the gamma power output for this configuration appeared not saturable using the present stimulation system.

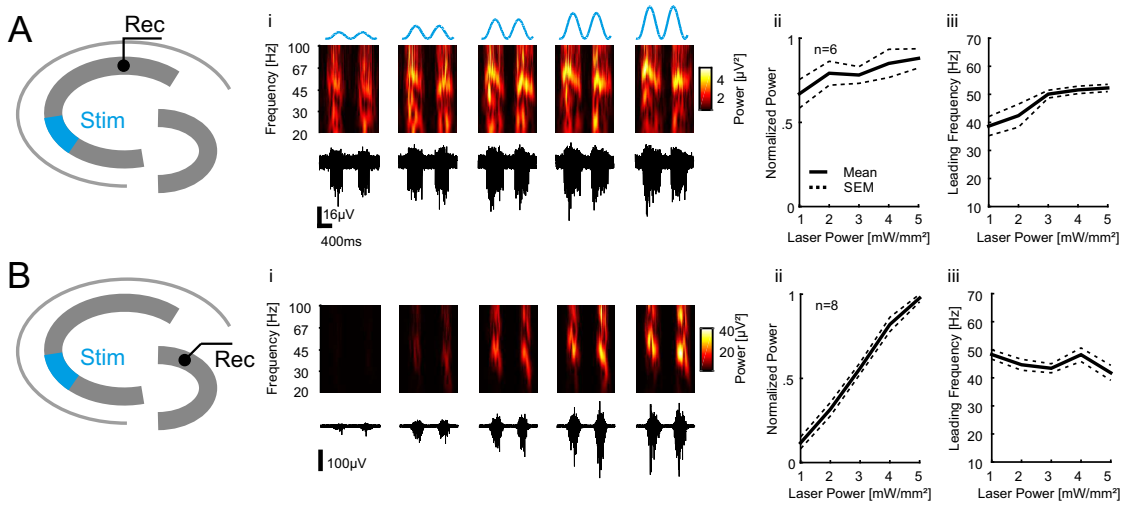

Figure 4.5: Input/output relationship between laser intensity and resulting power and frequency of resulting distally generated gamma. *(A) Schematic illustration of the stimulation/recording configuration. AOI was limited to CA3 pyramidale and a recording electrode in CA1 was picked for analysis. (Ai) Bottom: Example traces showing gamma activity in response to increasing laser intensity. Top: Corresponding wavelet spectra revealing frequency distribution. (Aii) Oscillation power normalized to maximum value as a function of laser intensity. (Aiii) Oscillation frequency as a function of laser intensity. Data in (Aii) and (Aiii) were recorded in 6 slices from 3 mice. (B) same as (A) but with recording in DG. Data in (Bii) and (Biii) were recorded in 8 slices from 3 mice.*

Overall, this series of experiments showed that power and frequency of evoked gamma oscillations are positively correlated to stimulus intensity. This effect was however less pronounced with regard to the resulting frequency.

4.1.2 Resonance Properties of Evoked Gamma Oscillations

In the previous set of experiments, slices were subjected exclusively to a 1Hz stimulation frequency. As a subsequent step, it should be determined whether the hippocampal network displays resonance effects in response to different frequencies of sinusoidal stimulation. Broadly speaking, it was examined whether gamma oscillations could be evoked 'more easily' at a certain stimulation frequency. To this end, slices were subjected to 5s periods of stimulation frequencies in the range between 1Hz-40Hz using the same stimulation/recording configurations already show in figure 4.4 and 4.5. Resonance properties of locally generated gamma are depicted in figure 4.6. It should be noted here, that stimulation intensity was kept constant at 5mW/mm^2 throughout this experimental series.

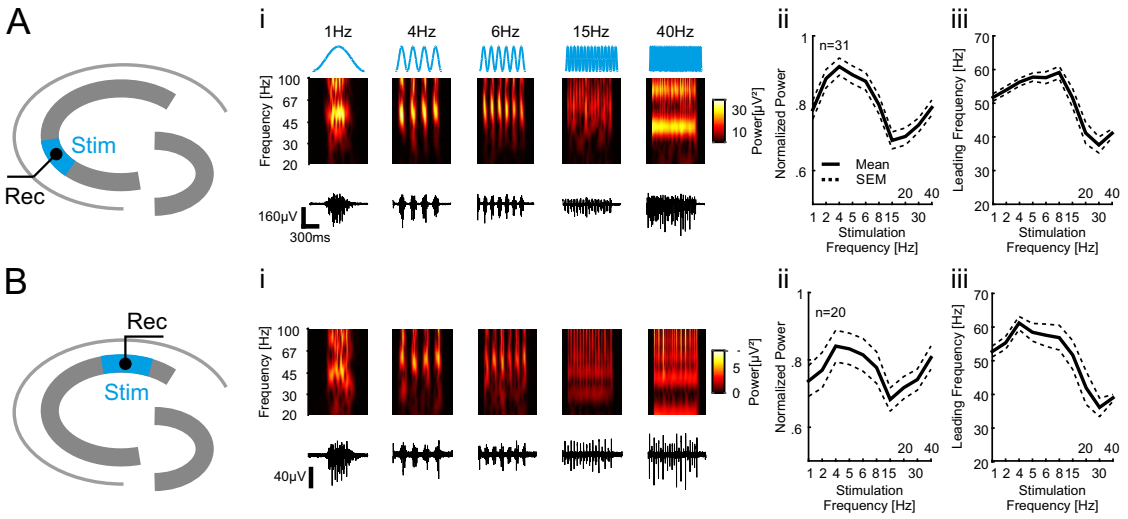

Figure 4.6: Resonance properties of locally generated gamma oscillations. *(A) Schematic illustration of the stimulation/recording configuration. AOI was limited to CA3 pyramidale and a recording electrode in the same area was picked for analysis. (Ai) Bottom: Example traces showing gamma activity in response to increasing stimulation frequency. Top: Corresponding wavelet spectra revealing gamma frequency distribution. (Aii) Oscillation power normalized to maximum value as a function of stimulation frequency. (Aiii) Oscillation frequency as a function of stimulation frequency. Data in (Aii) and (Aiii) were recorded in 31 slices from 8 mice. (B) same as (A) but with stimulation/recording in CA1. Data in (Bii) and (Biii) were recorded in 20 slices from 7 mice.*

As indicated in figure 4.6, the output gamma power of the hippocampal network showed a clear preference to stimulation frequencies between 2Hz-6Hz. This observation appears very compelling as this frequency range overlaps with the low theta spectrum (Buzsaki and Draguhn, 2004) and gamma rhythms *in vivo* usually occur superimposed onto an underlying theta wave (Buzsaki et al., 1983). Considering this information, it seems reasonable that the architecture of the hippocampal network is optimised to generate gamma oscillations at this input frequency in the most efficient manner. The data presented here furthermore stand in good accordance with

findings published by Butler et al. (2016) in which a similar stimulation paradigm was utilised. Strikingly, it appears that gamma power increased again when stimulation frequencies higher than 15Hz were applied (see figure 4.6 (Aii) and (Bii)). However, this is most likely caused by the fact that the field potential merely follows the input frequency in this domain which is for instance shown in figure 4.6 (Ai) and (Bi). Possible reasons for this behaviour are given in the discussion. This notion was further supported by data provided in figure 4.6 (Aiii) and (Biii) which show that leading gamma frequencies centre around stimulation frequency especially at 40Hz input. Nevertheless, it is interesting to note that input frequencies between 1Hz-15Hz elicited oscillations with a steadily increasing frequency. Possible underlying mechanisms are presented later on.

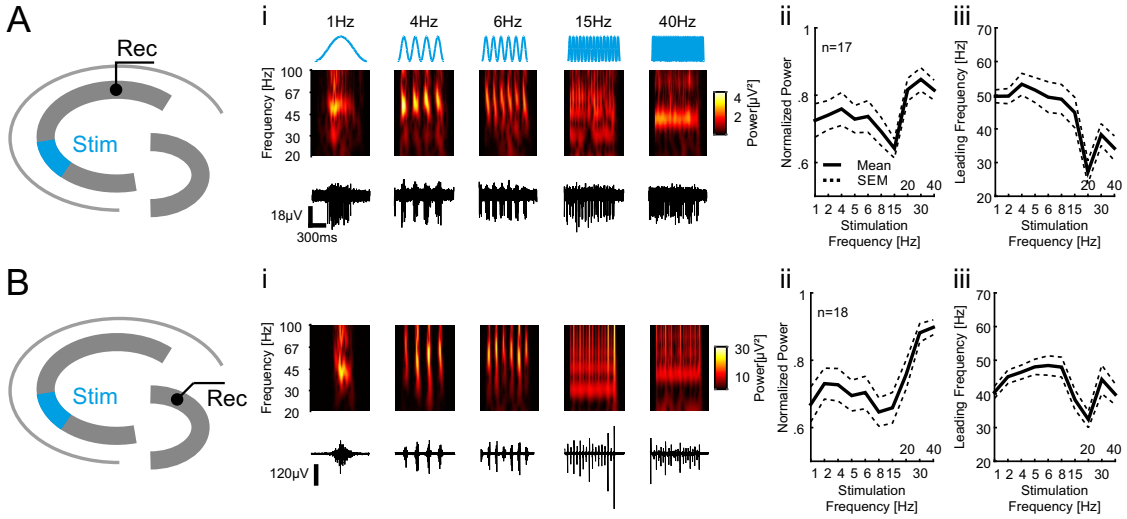

Figure 4.7: Resonance properties of distally generated gamma oscillations. *(A) Schematic illustration of the stimulation/recording configuration. AOI was limited to CA3 pyramidale and a recording electrode in CA1 was picked for analysis. (Ai) Bottom: Example traces showing gamma activity in response to increasing stimulation frequency. Top: Corresponding wavelet spectra revealing gamma frequency distribution. (Aii) Oscillation power normalized to maximum value as a function of stimulation frequency. (Aiii) Oscillation frequency as a function of stimulation frequency. Data in (Aii) and (Aiii) were recorded in 17 slices from 7 mice. (B) same as (A) but with stimulation/recording in CA1. Data in (Bii) and (Biii) were recorded in 18 slices from 8 mice.*

The situation for distally generated gamma was less clear. While gamma power propagated to CA1 or to the DG still displayed a somewhat discernible peak at ∼4Hz it is far less pronounced when compared to locally generated gamma. Furthermore, the previously mentioned effect that field potentials simply follow upon high frequency input was even stronger in comparison. It is also noteworthy that oscillation frequencies propagated from CA3 to CA1 appeared less susceptible to changes in input frequency as they remained relatively stable at around 50Hz while backpropagated gamma frequency was positively correlated to input frequency (see figure 4.7 (Aiii) and (Biii)).

Taken together, the hippocampal slice network exhibited resonance behaviour at stimulation frequencies which overlapped with the low theta range. This provides evidence that the hippocampal network serves as biological substrate which is organised in a such a way that information processing is carried out most efficiently within a theta/gamma rhythm.

4.1.3 Subregional Differences of Gamma Oscillations in CA3

Until now, the AOI was exclusively limited to CA3a, the most distal part of CA3 with respect to the DG. However, since there are known differences in the extent to which these anatomically distinct subregions participate in hippocampal activity (Hunsaker et al., 2008; de Almeida et al., 2007), it was necessary to characterise them in more detail. To find out more about each subregion's capability for generating gamma oscillations, slices were subjected to the same resonance frequency paradigm described in the previous section but with stimulation/recording limited to one of the three subfields (see figure 4.8 (A)). The results of this analysis are summarised in figure 4.8 (B) and (C).

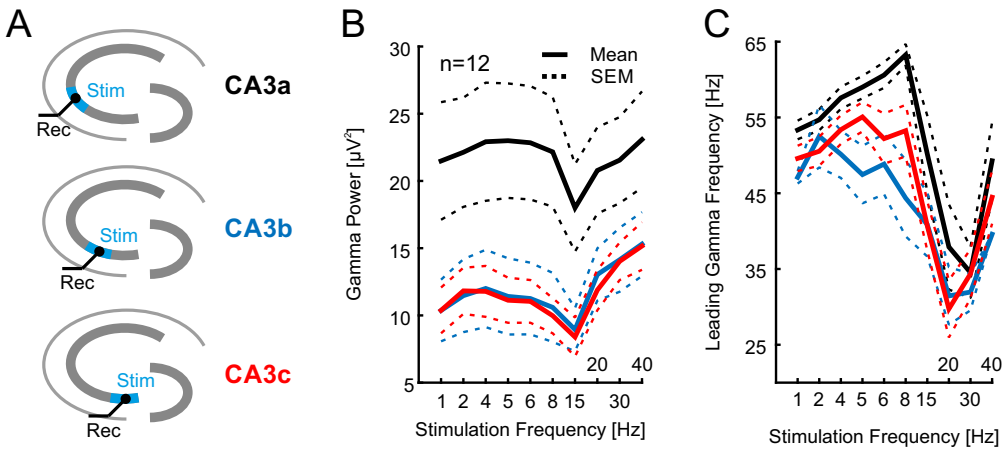

Figure 4.8: Resonance properties of locally generated gamma oscillations in CA3 subfields. *(A) Schematic illustration of the stimulation/recording configuration. AOI was limited to stratum pyramidale in CA3a, CA3b or CA3c and a recording electrode in the same area was picked for analysis. (B) Oscillation power in CA3a (black), CA3b (blue) and CA3c (red) in absolute values as a function of stimulation frequency. (C) Oscillation frequency as a function of stimulation frequency. Data in (B) and (C) were recorded in 12 slices from 4 mice.*

As presented in figure 4.8 (B), sinusoidal stimulation in all three subfields reliably elicited gamma oscillations with a similar resonance maximum between 2Hz-6Hz. However, in this case there was no apparent peak but instead a plateau of resonance frequencies. Most remarkably, there was a clear difference between CA3a intrinsic gamma and both of the other subregions concerning their resonance profile. While overall gamma power in CA3a ranged between 15-25μV^2, gamma power in

the two other subfields was much lower (between 5-15μV^2). In terms of gamma frequency, there was no noticeable difference among the subregions in response to input frequency. Although gamma frequency in CA3a appeared to be positively correlated with input frequency (as already reported in figure 4.6 (A)), the variance in comparison to other subregions makes it difficult to make a conclusive statement.

After all, these data indicate that CA3a may be the principal hub within CA3 which is responsible for effective integration and transmission of information between the DG and CA1.

4.1.4 Characterisation of Evoked Sharp Wave-Ripple Complexes

The data shown in figure 4.1 illustrate that optogenetic stimulation in CA3 using a 5ms square pulse elicits SPW-R in downstream CA1. The properties of this stimulation paradigm were addressed here in a more quantitative manner. First, it was determined whether there is, similarly to the data presented in figure 4.4 and 4.5, an intensity dependent change in the properties of evoked field potentials. As shown in the representative example data in figure 4.9 (B), the ripple component of the evoked LFP became less pronounced with increasing laser intensity until it was completely lost with maximal stimulation strength. It appears that the evoked potential became more synchronised with increasing stimulation strength. In fact, in some slices it was even possible to evoke a summed action potential (population spike) in CA1 pyramidale upon maximal stimulation (data not shown). More thorough analysis of the input/output relationship between stimulation intensity and LFP properties revealed that while amplitudes of field potentials were statistically significantly increased (figure 4.9 (C), $p<0.0001$, repeated measures ANOVA), their full width at half maximum (FWHM) was reduced with growing laser power (figure 4.9 (D), $p<0.0001$, repeated measures ANOVA). This underlines the notion that inputs to the local network of downstream CA1 which receives mostly excitatory input from CA3 become more synchronised with increasing stimulation strength. Furthermore, it appears that ripple oscillations superimposed on evoked field potentials gradually diminished until they completely disappeared. This is statistically examined in figure 4.9 (E) and (F). First, the SPW-R success rate was determined by individual analysis of 1175 field potential responses recorded from 34 slices and classifying them into whether or not they can be regarded as canonical SPW-R. This was done by visual inspection taking into account typical SPW-R parameters such as number of ripple cycles (at least three), width of the slow LFP component ($\sim$20ms) and temporal delay between stimulation and onset of LFP to exclude spontaneous SPW-R from the analysis.

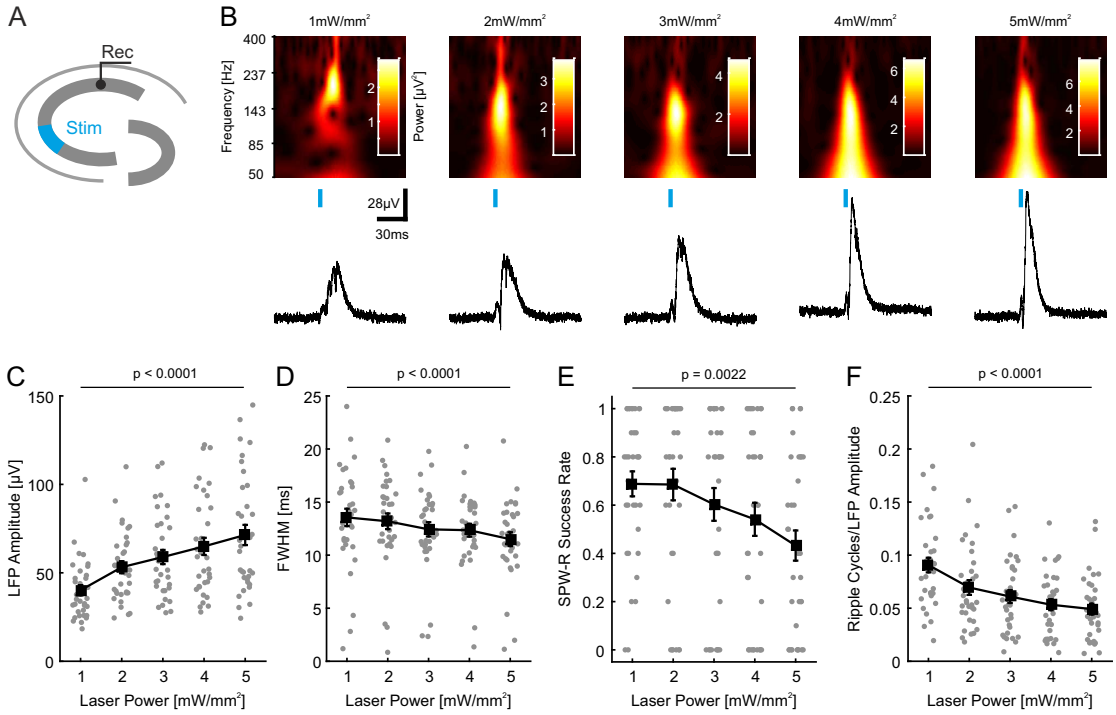

Figure 4.9: Characterisation of local field potential properties evoked by 5ms square pulses of varying intensity. *(A) Schematic illustration of the stimulation/recording configuration. AOI was limited to stratum pyramidale in CA3a and a recording electrode in CA1 was picked for analysis. (B) Bottom: Representative evoked field potentials in response to increasing laser intensity. Top: Corresponding wavelet spectra showing frequency components of field potentials. (C) Amplitude of evoked field potentials as a function of laser power. (D) Full width at half maximum (FWHM) of evoked field potentials as a function of laser power. (E) SPW-R success rate as a function of laser power. (F) Ripple cycles normalised to field potential amplitude as a function of laser power. Data in (C-F) were recorded in 34 slices from 11 mice. Grey dots indicate individual data points, black squares represent mean±SEM. Statistical significance was assessed by repeated measures ANOVA.*

As is evident from figure 4.9 (D), the SPW-R success rate decreased dramatically in response to higher stimulation strengths ($p<0.0022$, repeated measures ANOVA) which indicates that in order to generate ripple oscillations, CA1 required a more dispersed input from CA3 which does not override inhibitory networks of CA1 which are thought to be required for ripple generation (Schonberger et al., 2014; Gan et al., 2017). A similar analysis which was less prone to human error was aimed at quantifying the number of ripple cycles in response to rising laser power (see Methods: Data Analysis). The results of this analysis (shown in figure 4.9 (F)) indicated a negative correlation between stimulus strength and number of ripple cycles ($p<0.0001$, repeated measures ANOVA). This result is in line with the observation that SPW-R success rate decreased with higher illumination power since by definition an SPW-R must have at least three ripple cycles.

In figure 4.3 (E-F) a qualitative comparison of evoked and spontaneous SPW-R is depicted which at first glance gives the impression that the differences are minuscule. In order to obtain a more quantitative view on this matter, 50 SPW-R of each group were picked at random from the pool of spontaneous and evoked SPW-R using MATLAB's pseudorandom number generator and typical parameters of SPW-R were compared. As presented in figure 4.10, there were no differences in ripple frequency (evoked: P_{25}=180Hz, P_{50}=195.8Hz, P_{75}=208.6Hz vs. spontaneous: P_{25}=176.3Hz, P_{50}=195.8Hz, P_{75}=204.2Hz, p=0.47, Mann-Whitney test), ripple power (evoked: P_{25}=0.49μV^2, P_{50}=0.6μV^2, P_{75}=0.75μV^2 vs. spontaneous: P_{25}=0.52μV^2, P_{50}=0.66μV^2, P_{75}=0.83μV^2, p=0.1962) or amplitude (evoked: P_{25}=0.24μV, P_{50}=0.31μV, P_{75}=0.43μV vs. spontaneous: P_{25}=0.19μV, P_{50}=0.27μV, P_{75}=0.36μV, p=0.0824). However, evoked SPW-R were accompanied by significantly fewer superimposed units which reflect extracellularly recorded action potentials (evoked: P_{25}=4, P_{50}=5, P_{75}=6 vs. spontaneous: P_{25}=5, P_{50}=7, P_{75}=9, p=0.011). This may be due to the fact that optogenetic stimulation is more synchronous compared to endogenous synaptic activity projected to CA1 which in turn may cause more pronounced co-firing of units in CA1 therefore reducing the amount of individually detectable action potentials.

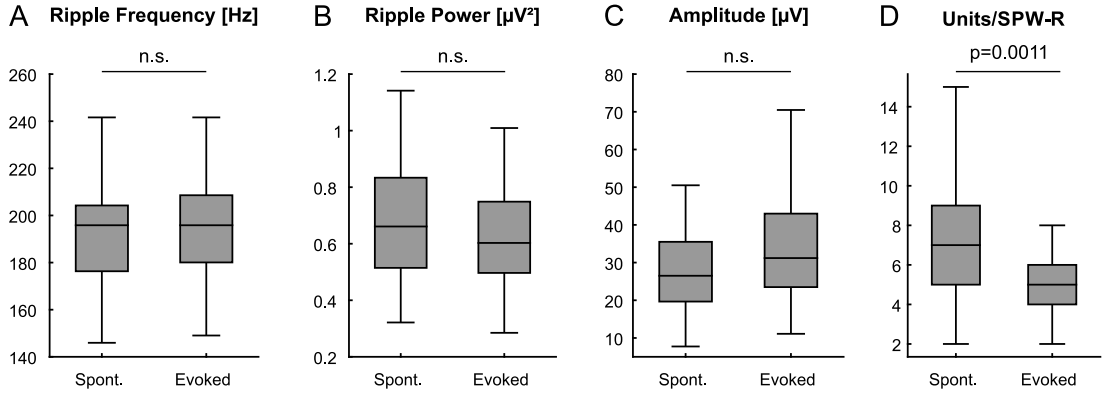

Figure 4.10: Statistical comparison of parameters of spontaneous and optogenetically evoked SPW-R. *Ripple frequency, ripple power, SPW-R amplitude were not significantly different while evoked SPW-R display significantly fewer units per SPW-R. Data in (A-D) were collected from 50 randomly picked SPW-R of each group. Statistical comparison was done using two-tailed Mann-Whitney test.*

To sum up, it appears that evoked SPW-R were more readily observed in CA1 upon weak CA3 stimulation. When laser stimulation was applied in excess, excitatory inputs were more strongly synchronised which could result in an input volley strong enough to override feed-forward inhibition which can cause hypersynchronous postsynaptic discharges. Moreover, statistically speaking, there were no significant differences between evoked and spontaneous SPW-R in terms of ripple frequency, ripple power and SPW-R amplitude.

4.1.5 Temporal Precision of Units is Highest with Theta Band Stimulation

Up to this point, analysis was limited to the field potential level. However, this approach disregards the dynamics of single cells in the context of local networks as field potentials reflect synaptic potentials of groups of several neurons. In order to obtain more detailed insight into the interaction of single cells and the network, it was necessary to investigate the behaviour of single unit discharges which reflect extracellularly recorded action potentials of individual neurons. These can be readily recorded with the planar extracellular electrodes of a MEA using a high-pass filter (Obien et al., 2014; Reinhard et al., 2014) (see Methods: Data Analysis).

In order to learn more about in how single cell activity is influenced by input frequency, slices were again subjected to the previously described resonance frequency paradigm (see figure 4.6 and figure 4.7). The results of this experiment are summarised in figure 4.11. When examining the exemplary data shown in figure 4.11 (Aii) it becomes evident, that units fired at progressively later time points relative to the phase of the stimulation sine wave. While most of the units appeared at the upstroke of the sine wave at 1Hz stimulation frequency, they were shifted further towards the downstroke at 40Hz. This observation was confirmed at a statistical level when viewing the polar plots displayed in figure 4.11 (B). These data highlight two interesting points: firstly, the previously mentioned shift in unit firing angle towards later stages relative to the sine wave was occurring gradually and secondly, the distribution of firing angles was narrower with some stimulation frequencies compared to others (see also figure 4.11 (C)). The width of the firing angle distribution is contained within the length of mean angle vector which is displayed as an orange arrow in figure 4.11 (B). A longer arrow points towards a more narrow distribution and vice versa. The normalised vector length as a function of input frequency is illustrated in figure 4.11 (Cii) which shows a local maximum in the theta range around 5Hz. This means that at stimulation frequencies within this spectrum, distribution of unit firing angles was more narrow compared to other frequencies which provides evidence towards more precisely timed single cell activity within the field potential oscillations.

It is also noteworthy that firing angles appeared fairly evenly distributed with one clear maximum with stimulation frequencies up to 8Hz. At frequencies of 15Hz and 20Hz, distributions became more non-uniform with either two peaks (15Hz) or strongly tilted (20Hz). However at even higher stimulation frequencies, firing angle distributions were again more even with a very low width (e.g. 30Hz). As figure 4.11 shows, interunit intervals tended to cluster around the lengths of one stimulus cycle at high stimulation frequencies (e.g. 25ms at 40Hz) further underlining the

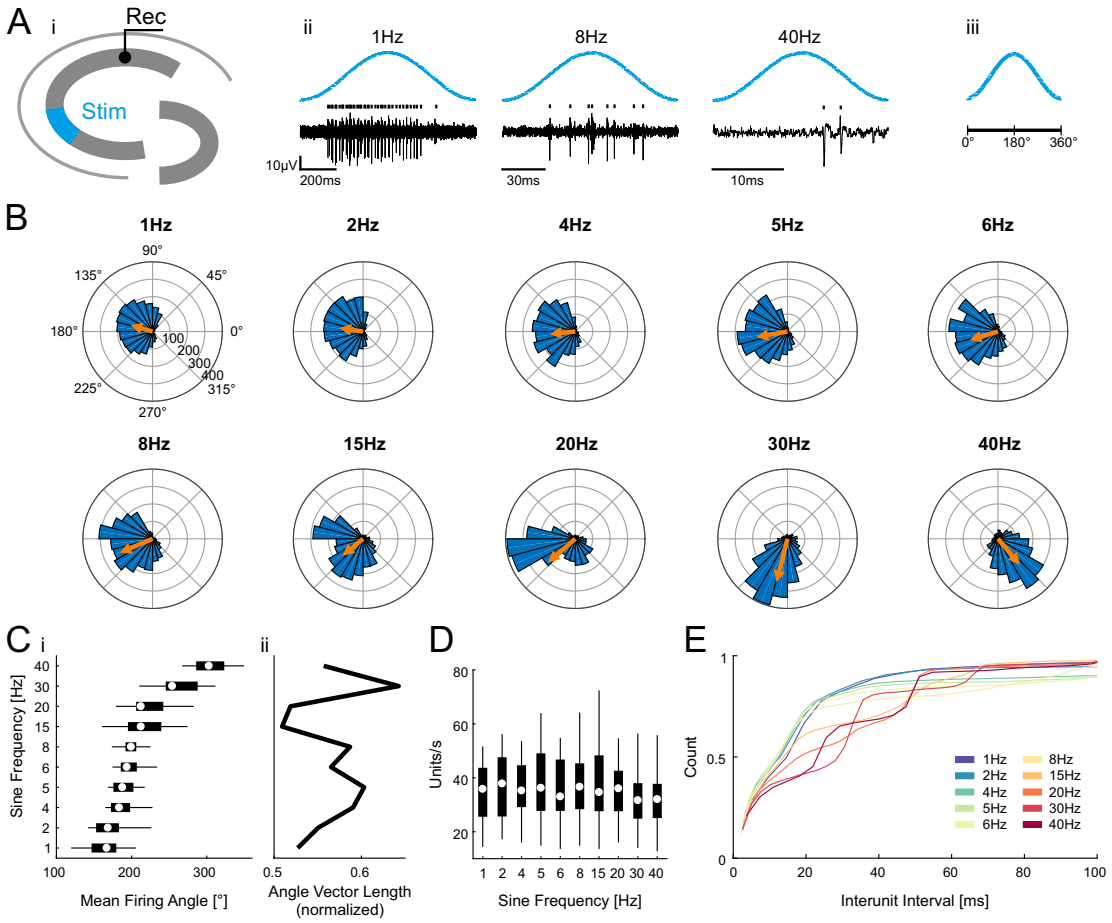

Figure 4.11: Phase relationship of single units to different stimulation frequencies. *(Ai) Schematic illustration of the stimulation/recording configuration. AOI was limited to stratum pyramidale in CA3a and a recording electrode in CA1 was picked for analysis. (Aii) Representative single unit recordings in response to one cycle of sinusoidal stimulation at 1Hz, 8Hz and 40Hz. Note the different temporal scale bars. Detected units are marked by ticks above the raw trace. (Aiii) Each cycle can be subdivided into 360˚ as a reference for unit timing. (B) Polar histograms of pooled data displaying the distribution of unit firing relative to the phase of each sine cycle in response to different sine frequencies. Length of orange arrows indicates width of distribution, orientation shows the mean phase angle. (Ci) Box plot of mean firing angle in response to different sine frequencies. (Cii) Length of the angle vector normalised to maximum value. (D) Box plot of number of units per second of stimulation in response to different input frequencies. (E) Cumulative histograms of interunit intervals recorded with different input frequencies. Data in (B-E) were recorded in 15 slices from 7 mice.*

notion that at these input frequencies, the network passively follows the input. This is in line with data shown in figure 4.6 and figure 4.7 which illustrated that gamma power is lowest at 15Hz and that the field potential merely follows inputs at higher stimulation frequencies. This could mean that using a 15Hz input causes destructive interference with the intrinsically generated gamma oscillations which leads to the observed effects. Although the number of recorded units per cycle declined with increasing input frequency due to shortening of cycle lengths, the overall unit rate appeared relatively constant at 30-40 units/s over the 5s recording period (figure

4.11 (D)). This suggests that there is no preferred stimulation frequency to recruit more units into the oscillation but that they are coordinated into segregated cycle associated packages more precisely which possibly provides means for more efficient information transfer.

Taken together, these data showed that single cell activity is dependent on input frequency and showed a preference towards theta band inputs. Units were distributed within individual temporal frames which were defined by the input frequency.

4.2 Investigation of the Network State Switch

According to the data presented until this point, it has become clear that the *in vitro* preparation described here is capable of producing gamma band oscillations as well as SPW-R upon either waxing and waning sinusoidal or synchronous stimulation with short square pulses. This raises the question whether the gradual increase of light intensity brought about by a sine wave is the critical factor causing synchronisation within a gamma rhythm. Conversely, it is conceivable that SPW-R can exclusively be elicited by extremely brief stimulation because ripple band oscillations have to be limited to a very short time window as they may represent chunked pieces of information.

In order to gain insight into the mechanisms by which these network patterns are governed, slices were subjected to stimulation with varying intensity slopes as well as prolonged square pulse stimulation. As depicted in figure 4.12 (B), an SPW-R could be evoked by stimulation with a square pulse which corresponds to an infinite rate of rise as described before (cf. figure 4.1 and figure 4.9). However, after decreasing the intensity slope giving it a more ramp-like appearance, gamma band oscillations gradually emerged whereas ripple power receded. This observation is statistically summarised in figure 4.12 (C) which shows that gamma oscillations apparently emerged instantaneously between 2 and 10 mW/mm^2s while ripple band power decreased drastically between 2 and 20 mW/mm^2s. This implies that gamma oscillations and SPW-R may be mutually exclusive and that they are regulated differently at a network level. It is interesting to note however that ripple power did not vanish completely in spite of the network being dominated by gamma oscillations(see figure 4.12 (C)). Possible reasons for this observation will be given in the discussion.

In the interest of elucidating the cellular mechanisms which govern the network synchronisation in a gamma rhythm, blind patch clamp recordings were performed in CA1 pyramidal cells. For this series of experiments, cells were patched in whole-cell voltage clamp mode with a holding potential of either -74mV or +10mV in

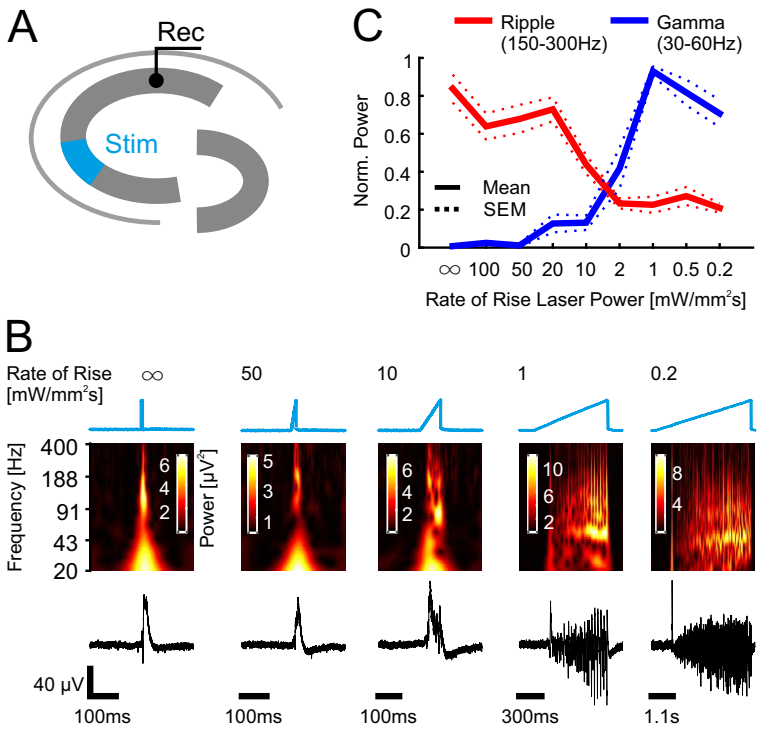

Figure 4.12: Changes in field potential frequency composition caused by different intensity time courses. *(A) Schematic illustration of the stimulation/recording configuration. AOI was limited to stratum pyramidale in CA3a and a recording electrode in CA1 was picked for analysis. (B) Bottom: Representative evoked field potentials in response to decreasing rate of rise of laser intensity. Top: Corresponding wavelet spectra showing frequency components of field potentials. (C) Power of ripple frequency band (150-300Hz, red) and gamma frequency band (30-60Hz, blue) as a function of varying rate of rise of laser power. Data were recorded in 15 slices from 7 mice.*

order to isolate inhibitory and excitatory postsynaptic currents (IPSCs/EPSCs), respectively (Gan et al., 2017; Roth et al., 2016). During recordings, the CA3a area of the slice was subjected a similar ramp-like stimulation paradigm as shown in figure 4.12 (B) using a 5s long ramp with a 0.2mW/mm^{2}s rate of rise. This window of stimulation was subdivided into 100ms bins and the leading frequency as well as the power of the 30-60Hz gamma band in the LFP were calculated. Furthermore, the frequency of IPSCs and EPSCs was assessed with respect to the onset of the ramp. The results of this analysis are shown in figure 4.13. As is already evident from the example traces shown in figure 4.13 (B) and (C), both the LFP and inhibitory and excitatory currents displayed a more and more pronounced synchronisation towards a gamma (in this case ∼50Hz) rhythm in response to increasing stimulation intensity. Strikingly, the data in figure 4.13 (D) suggest that this oscillatory switch into the gamma mode appears to occur in a step-like fashion since the leading frequency of the local field potential "jumps" into a ∼30Hz oscillation around 200-300ms after ramp onset. Following this initial switch, the leading frequency increased in an almost linear fashion with increasing time. This increase in gamma frequency can

be explained by the rising stimulation intensity as already shown in figures 4.4 and 4.7. The step-like switch was less pronounced when analysing the gamma power as displayed in the left panel of figure 4.13 (D) although, there appears to be a slight upward kink in gamma power also around 200-300ms after stimulus onset. At the IPSC/EPSC level, a similar rapid increase in event frequency was found as demonstrated in figure 4.13 (E). The frequency of both IPSCs and EPSCs showed a sharp increment within a similar time frame as the frequency of LFPs. It is moreover interesting to note that once the network has switched into the gamma mode IPSCs occurred with a much higher frequency compared to EPSCs. While the occurrence of EPSCs seemed to saturate at 40-50Hz, IPSCs can be recorded at frequencies of up to 60 or 70Hz which even exceeds the leading frequency of the local field potential. This finding and its implications for network mechanisms of gamma will be addressed in the discussion.

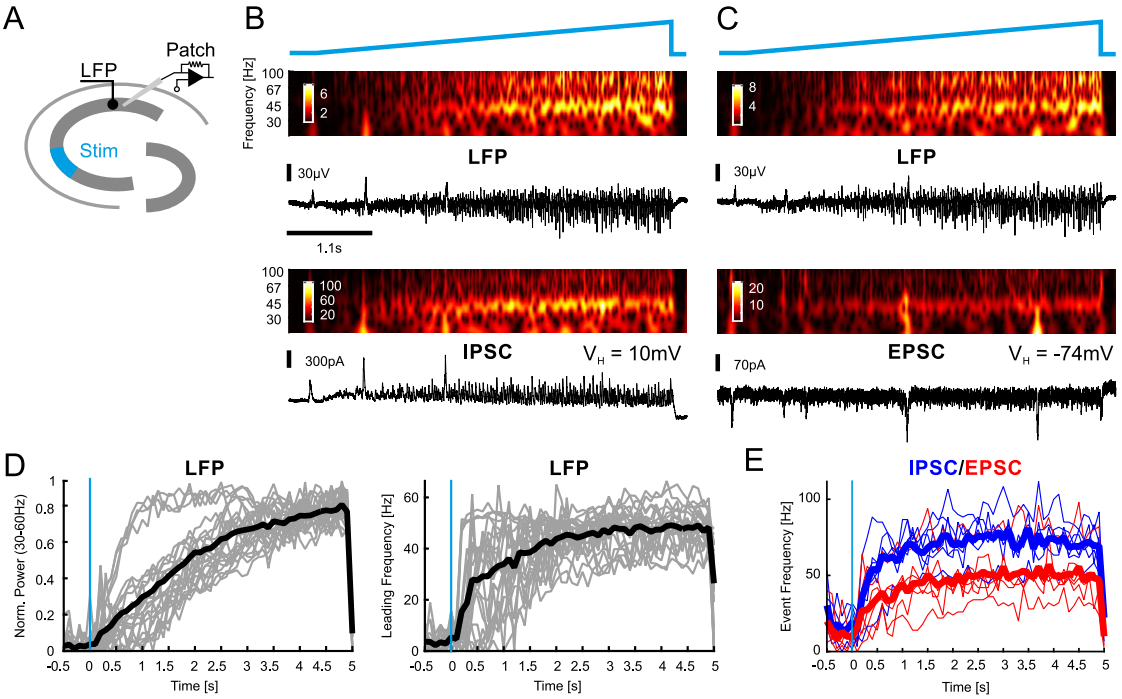

Figure 4.13: Gamma synchronisation at the network and single-cell level. *(A) Schematic illustration of the stimulation/recording configuration. AOI was limited to stratum pyramidale in CA3a and a MEA electrode in CA1 was picked for LFP analysis while whole-cell patch clamp recordings were performed simultaneously in the vicinity of the MEA electrode. (B) Example LFP recordings (top) together with IPSC recordings of a pyramidal cell (bottom). (C) Same as (B) but with simultaneous recordings of EPSCs. Note that both IPSCs and EPSCs show synchronisation at ∼50Hz albeit EPSCs are much smaller in amplitude. (D) Normalised power in the 30-60Hz band over time during the 5s ramp (left) and leading LFP frequency over time during the 5s ramp (right). Grey traces show individual recordings, black trace indicates mean. (E) IPSC (blue) and EPSC (red) frequency over time during the 5s ramp. Thin lines indicate individual recordings, thick ones display the mean. The light blue line at 0s in (D) and (E) denotes the onset of the ramp stimulation. Data in (D) were recorded in 9 slices from 5 mice. Data in (E) were recorded from 6 cells in 4 slices from 2 mice.*

Using a similar experimental preparation, Dine et al. (2016) reported that global stimulation of CA1 with prolonged rectangular pulses elicits gamma band oscillations locally. This observation contradicts the initial hypothesis proposed here which states that gamma oscillations are only evoked by a steadily increasing input following a ramp or sine wave (cf. figure 4.6 and figure 4.12).

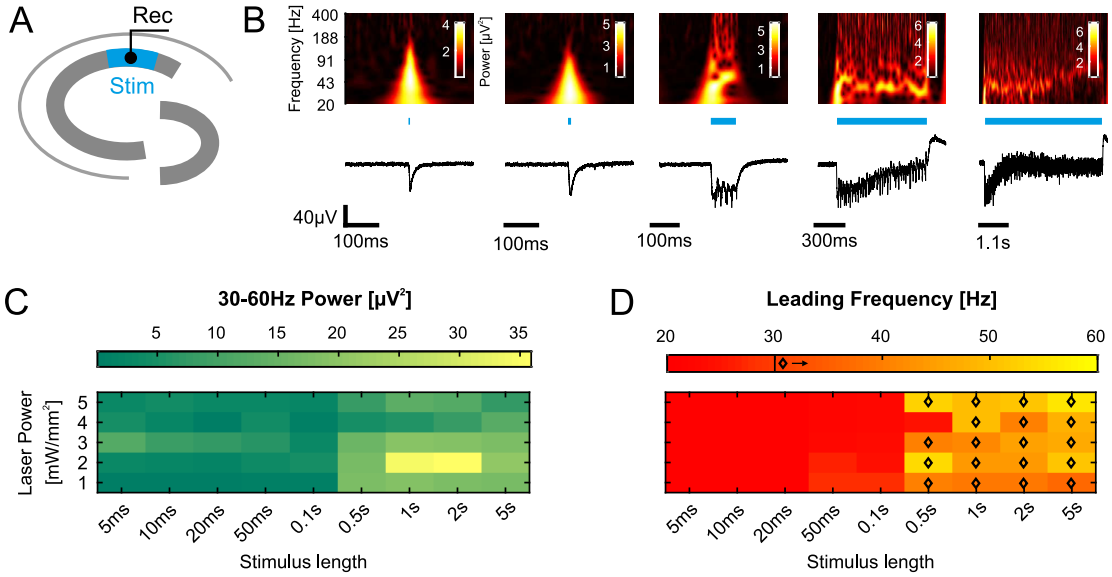

Figure 4.14: Emergence of locally generated gamma oscillations in CA1 in response to different square pulse lengths. *(A) Schematic illustration of the stimulation/recording configuration. AOI was limited to stratum pyramidale in CA1 and a recording electrode in the same area was picked for analysis. (B) Bottom: Representative evoked field potentials in response to increasing length of stimulation. Top: Corresponding wavelet spectra showing frequency components of field potentials. (C) Colour-coded map showing gamma band oscillation power (30-60Hz) as a function of both stimulus length (x-axis) and laser intensity (y-axis). Brighter colours represent higher power. (D) Same as (C) but leading frequency of evoked oscillation is displayed. Pixels which correspond to a combination of stimulus length and intensity which evoked frequencies larger than 30Hz are marked with a diamond. Data in (C) and (D) show averaged maps of recordings in 11 slices from 4 mice.*

Therefore, in order to revise these experiments, slices were stimulated with square pulses ranging from 5ms to 5s in length and of varying intensity. As can be seen in figure 4.14, local stimulation of CA1 pyramidale led to a negative deflection of the local field potential. This is due to fact that ChR2 acts as a non-selective cation channel which leads to a massive influx of cations and therefore to an extracellular negativity. Interestingly, the negative evoked field potentials appeared to synchronise into a gamma band rhythm if duration of light exposure exceeded 100ms. This is especially well illustrated in the middle panel of figure 4.14 (B). While light pulses shorter than 100ms merely led to a short and rapidly decaying negative field potential, a very prominent frequency component between 30-60Hz emerged when stimulation is applied for longer periods. This finding is summarised in figure

4.14 (D) which shows that synchronisation requires between 100ms and 500ms to develop a clear gamma band activity. This is further supported by data shown in figure 4.14 (C) showing that gamma band power displayed a step-like increase at 500ms stimulation length. It should also be noted that gamma band power reached a maximum when stimulated at 5mW/mm^2 and decreased when intensity exceeded this value. Possible reasons for this observation are given in the discussion. Overall however, these data confirm the initial reports of Dine and colleagues.

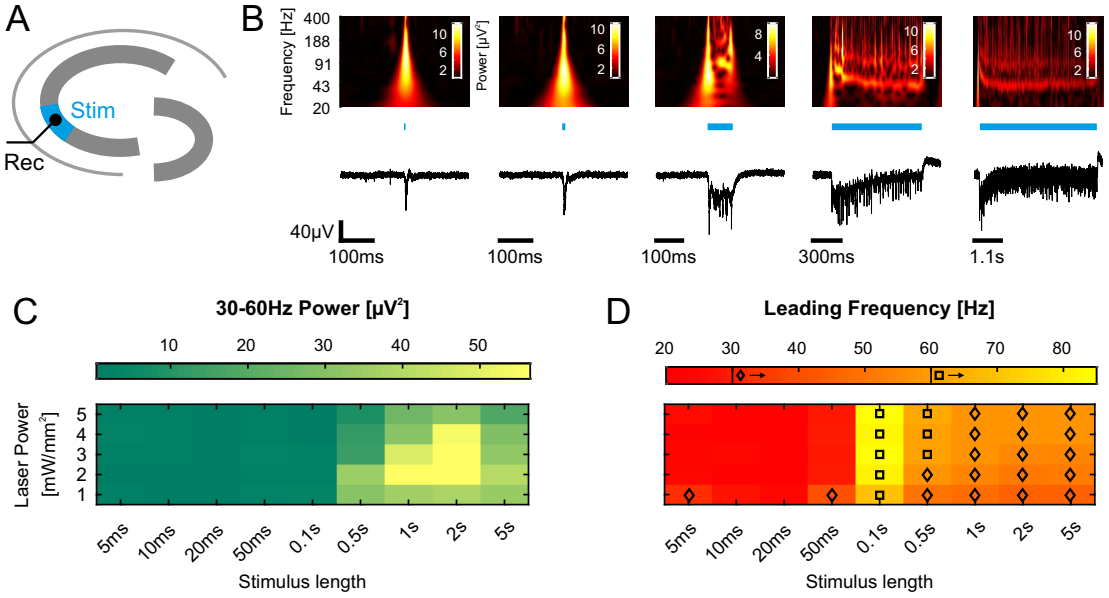

Figure 4.15: Emergence of locally generated gamma oscillations in CA3 in response to different square pulse lengths. *(A) Schematic illustration of the stimulation/recording configuration. AOI was limited to stratum pyramidale in CA3a and a recording electrode in the same area was picked for analysis. (B) Bottom: Representative evoked field potentials in response to increasing length of stimulation. Top: Corresponding wavelet spectra showing frequency components of field potentials. (C) Colour-coded map showing gamma band oscillation power (30-60Hz) as a function of both stimulus length (x-axis) and laser intensity (y-axis). Brighter colours represent higher power. (D) Same as (C) but leading frequency of evoked oscillation is displayed. Pixels which correspond to a combination of stimulus length and intensity which evoked frequencies larger than 30Hz or 60Hz are marked with a diamond or a square, respectively. Data in (C) and (D) show averaged maps of recordings in 22 slices from 5 mice.*

In order to extend the scope of these findings, the same stimulation paradigm was applied to CA3. Similarly to CA1, local stimulation of CA3 led to an negative field potential deflection which synchronised into a gamma rhythm if stimulation was applied for a prolonged period. However, unlike CA1 which required a minimum stimulus length of 500ms to robustly generate a gamma oscillation, CA3 gamma already emerged at 100ms stimulus length (see figure 4.15 (D)). Moreover, the frequency of evoked oscillation was dominated by a component higher than 60Hz at periods lasting between 100ms and 500ms. This might indicate that the recurrent architecture of CA3 is able to generate higher frequencies compared to other

subregions of the hippocampus. However, it appears that CA3 was unable to maintain these high frequencies exceeding 60Hz for longer extents of time as stimulation lengths of more than 500ms resulted in leading frequencies below this value. Within this framework, CA3 behaved similarly to CA1 considering the fact that power of gamma oscillations was diminished when light intensity exceeded 2-3mW/mm^2 or stimulation was carried out for more than 2s as depicted in figure 4.15 (C).

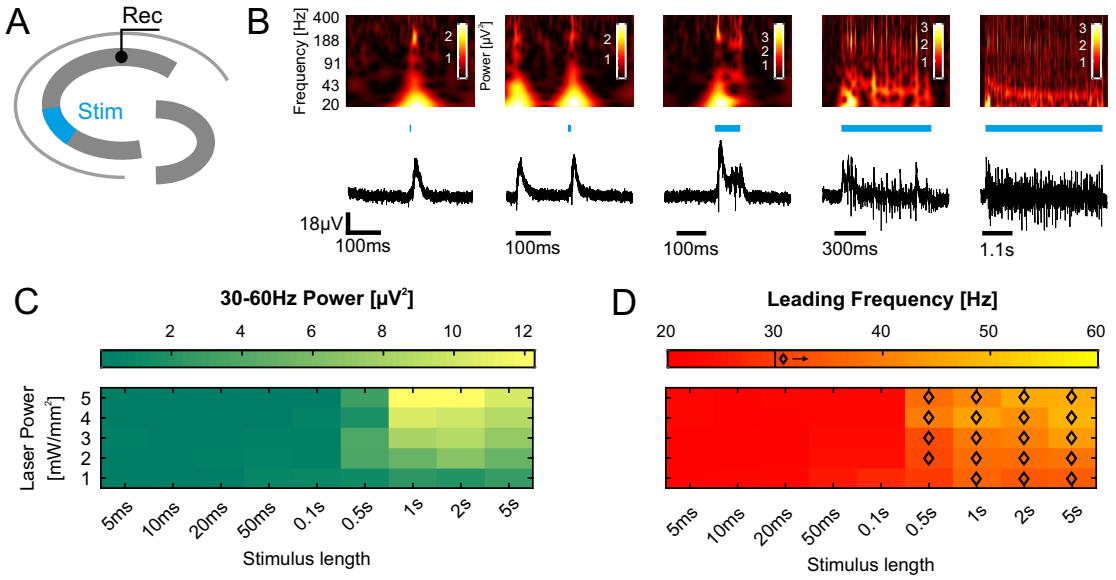

Figure 4.16: Emergence of gamma oscillations in CA1 in response to different square pulse lengths applied to CA3a. *(A) Schematic illustration of the stimulation/recording configuration. AOI was limited to stratum pyramidale in CA3a and a recording electrode in CA1 was picked for analysis. (B) Bottom: Representative evoked field potentials in response to increasing length of stimulation. Top: Corresponding wavelet spectra showing frequency components of field potentials. (C) Colour-coded map showing gamma band oscillation power (30-60Hz) as a function of both stimulus length (x-axis) and laser intensity (y-axis). Brighter colours represent higher power. (D) Same as (C) but leading frequency of evoked oscillation is displayed. Pixels which correspond to a combination of stimulus length and intensity which evoked frequencies larger than 30Hz are marked with a diamond. Data in (C) and (D) show averaged maps of recordings in 13 slices from 5 mice.*

Lastly, propagation of field potentials from CA3 to CA1 was assessed. As is evident from figure 4.16 (B), optogenetic excitation of CA3a evoked an SPW-R in downstream CA1 with square pulse of length up to 20ms which could be expected considering the previously shown data (e.g. figure 4.1). However, applying a more prolonged stimulus of more than 100ms caused the network to initially generate an SPW-R like signature which is followed by gamma band activity (see figure 4.16 (B)). The emergence of gamma oscillations in response to different light intensities and stimulus lengths is summarised in figure 4.16 (D). Similarly to locally generated gamma in CA1, the network required at least 500ms to synchronise into a rhythm of more than 30Hz. Power of evoked gamma oscillation again depended on laser

power and stimulus length as illustrated in figure 4.16 (C). Interestingly, at lower light intensities, gamma was hardly present in CA1 indicating a minimum level of activity required for efficient transfer of information.

In conclusion, it seems that the hippocampus requires a certain minimal activity level as well as prolonged inputs exceeding 100ms to generate robust gamma band activity. CA3 was able to produce higher gamma frequencies at lower input durations compared to CA3 which may be caused by the structural characteristics or by differences in cellular composition or biophysical properties. Another finding which confirms the report of Dine et al. (2016) is that oscillation frequency and power declined rapidly after stimulus onset and stabilised at a lower frequency than initially. Additionally, it was found that prolonged stimulation of CA3 led to an SPW-R like event at stimulus onset followed by gamma band activity which provides further evidence to the notion that onset and time course of inputs determine hippocampal rhythms. Most strikingly however, it appears that gamma oscillations appear to emerge in a step-like fashion which could be governed by a sharp increase in inhibitory and excitatory currents around 200-300ms after stimulus onset.

4.3 Estimating the Number of Optogenetically Activated Neurons

In order to get an idea of how many cells were typically activated by optogenetic stimulation in CA3a, hippocampal slices were fixed in 4%PFA after the experiment and stained for NeuN, a marker for neuronal nuclei. Fixed preparations were subsliced to 25μm which should contain approximately only a single layer of cells assuming a typical somatic diameter of 20-30μm of a CA3 pyramidal neuron (Andersen, 2007). By overlaying the fluorescent image with a polygonal shape that resembled the AOI used for stimulation during an experiment, the number of cells within this area could be assessed. An example of such a staining and the approach for cell counting is illustrated in figure 4.17. As can be seen in figure 4.17 (A), the prominent EYFP staining wass distributed evenly across the entire hippocampal formation. Since the expression construct codes for a ChR2-EYFP fusion protein which is integrated into the cell membrane, EYFP signal in *stratum pyramidale* in CA3/CA1 or *stratum granulare* in DG was weaker compared to *stratum radiatum* for example. This can be explained by the higher cytosol/membrane ratio in the soma containing areas.

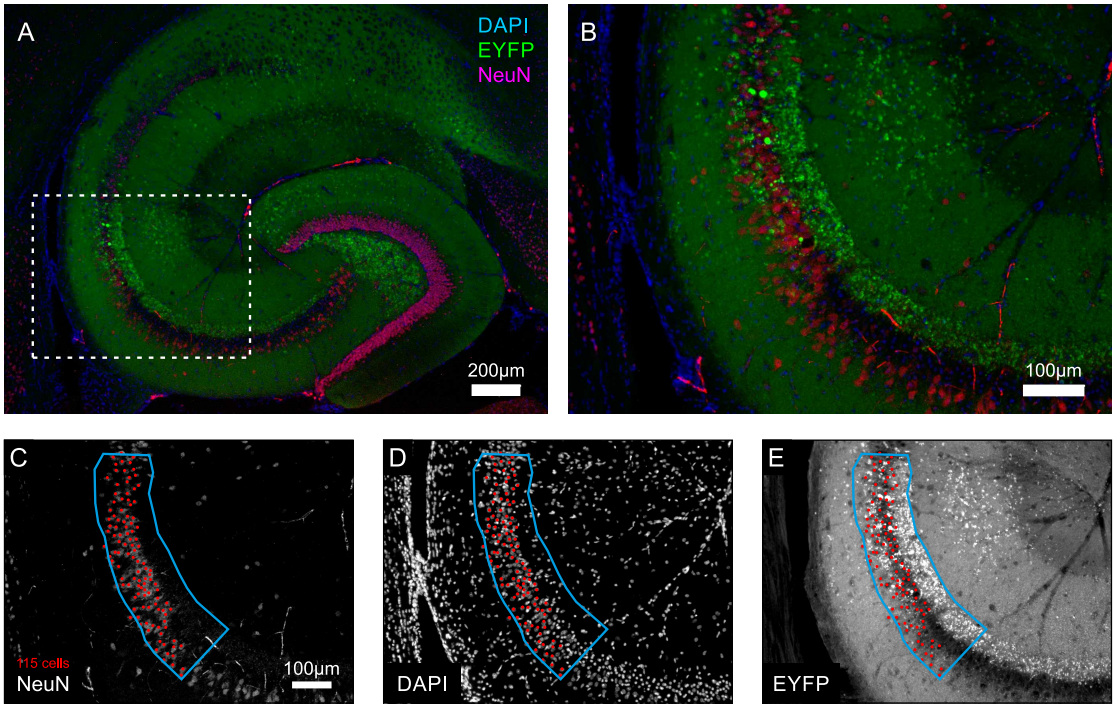

Figure 4.17: Estimation of Cell Number Activated by Laser Stimulation During a Typical Experiment. *(A) Fluorescence microscopic image of a 25µm thick hippocampal slice used for post-experimental staining. Image taken at 4x magnification. Framed area is shown at 10x magnification in (B). (C-E) Colour channels of the image shown in (B) split into NeuN (C), DAPI (D) and EYFP (E). A typical AOI used for optogenetic stimulation is displayed as a blue frame. Individual neurons within the AOI (n=115) are marked by red dots and were detected by NeuN/DAPI/EYFP staining. Scale bar in C is also applicable to (D) and (E).*

Individual cells were identified by colocalisation of NeuN and EYFP signal. Since the NeuN signal appeared relatively ruffled so that borders of single cells were difficult to make out, the DAPI signal served as an additional reference. As shown in figure 4.17 (C) the AOI in this particular slice contained 115 neurons. On average, the AOI in CA3a enclosed 118±3 cells (mean±STD, 3 slices, 2 mice). This value stands in good accordance with cell counts published by Golub et al. (2015) who found that the CA3 subfield of 30μm thick slices contains between 300 and 400 NeuN positive cells. Since the AOI in the experiments described here covered around a third of the total length of CA3, the results affirm these numbers. A 400μm thick slice contains between 13 and 20 layers of cells in CA3 assuming a somatic diameter of 20-30μm which means that the total volume beneath the AOI encompasses between 1573 and 2360 neuronal somata. In spite of the fact that the laser is focussed and should therefore deliver light relatively precisely in z-direction, due to scattering effects in brain tissue, it is difficult to make a statement about whether cells throughout the entire depth of the AOI receive sufficient optogenetic drive to fire action potentials. In addition, variations in ChR2 expression levels among cells may contribute to differences in activated cells.

In conclusion, in order to obtain more accurate information about the actual number of cells which are driven by optogenetic stimulation, single cell recordings may be needed to determine variations in ChR2 expression and to investigate scattering effects. For the latter, it may be feasible to shift the position of the focal point in three dimensions around the recorded cell. Nevertheless, based on the data at hand, it can be said that the number of potentially activated neurons ranges between 1573 and 2360.

5 Discussion

The data presented here provide first hints towards how hippocampal networks achieve the rapid state transition between the two most prevalent and behaviourally relevant oscillatory conditions. While there is a large body of work on the importance of gamma oscillations (Colgin, 2016; Buzsaki and Wang, 2012) and sharp wave-ripples (SPW-R) (Buzsaki, 2015) for memory formation and consolidation, knowledge about what happens at the cellular and network level when LFPs switch from one state to the other is scarce.

The main findings reported here are as follows: 1.) Driving pyramidal cells in a hippocampal slice preparation with different stimulus time courses evokes distinct network patterns resembling those *in vivo*. Short, synchronous excitation leads to generation of SPW-R and steadily increasing or prolonged inputs cause synchronisation in a gamma rhythm. 2.) The evoked gamma oscillation appears to occur instantaneously indicating a step-like switch of network states. 3.) Induction of gamma rhythmic activity is most efficiently achieved at low theta input frequencies both at the local field potential level as well as on the single unit level. This suggests that hippocampal networks are structurally preset to operate best at the physiological input frequency.

In this section, the results of this thesis will be discussed in the context of current working hypotheses about hippocampus dependent memory formation.

5.1 Implications for Hippocampal Gamma Oscillations

First of all, it appears striking that a highly reduced hippocampal slice network which is deprived of many important external inputs, from e.g. the medial septum is still capable of generating LFP patterns closely resembling physiological activity in an intact system. While this finding is not novel and there are many other *in vitro* preparations which have been reported to display similar behaviour even extending to spontaneous theta generation (Goutagny et al., 2009), it suggests that the spectrum of activity patterns in the hippocampus is predetermined by its architecture. In this context, the finding that both CA3 and CA1 are able to generate gamma intrinsically (figure 4.4 and 4.6) provides evidence that they possess similar

cellular composition necessary for gamma. Although it cannot be ruled out that optogenetic stimulation in CA1 also recruits Schaffer collateral inputs from CA3 in the experiments described here, CA1 minislice recordings published by Butler et al. (2016) support the notion of locally produced gamma. Butler et al. (2016) furthermore provided convincing evidence that optogenetically induced gamma is brought about by a pyramidal-interneuron gamma (PING) mechanism by showing that firing of pyramidal cells precedes that of interneurons. It has also been shown that gamma band activity can also be induced by stimulation of PV^+ interneurons, suggesting an interneuron gamma (ING) process (Cardin et al., 2009). However, the data presented by Cardin et al. (2009) leave the impression that the observed peak in the 40Hz band is merely an artefact of the used 40Hz stimulation frequency. It could be argued that the whole hippocampal network just follows the input frequency because of the large axonal arborisations of PV^+ interneurons innervating the majority of hippocampal cells. In contrast to that, the data presented here and findings published by Butler et al. (2016) hint towards a self synchronisation mechanism which involves feedback inhibition between excitatory and inhibitory cells. Furthermore, as Moca et al. (2014) have shown, membrane resonance properties appear to constitute another important factor for gamma oscillations. A remarkable feature of optogenetically induced gamma oscillations is that they appear to emerge instantaneously, meaning that the frequency of evoked activity does not "ramp up" gradually with increasing input strength but that the network locks into gamma mode in an almost digital fashion (see fore example figure 4.6 or 4.7). A possible underlying mechanism for this step-like state transition could be that excitation of inhibitory interneurons needs to exceed a threshold upon which in turn excitatory neurons are silenced according to a classical feedback inhibition circuit. This could mean that the frequency of evoked oscillations depends mostly on synaptic time constants between principal cells and interneurons. The identity of interneurons can however be only speculated about although PV^+ basket cells are highly likely to be involved (Buzsaki and Wang, 2012; Pastoll et al., 2013).

It could be demonstrated that the frequency of evoked gamma rhythms depends on illumination intensity (see figure 4.4 and 4.5). This unexpected finding may be explained by considering a gamma model proposed by Traub et al. (1996) which provides evidence that the major contributing factor for gamma frequency is excitatory input to interneurons. This proposition was confirmed by *in vitro* recordings of LFPs under application of increasing amounts of glutamate (Traub et al., 1996). Stronger light stimulation most likely has a similar effect on the local feedback network.

Additionally, results shown in figures 4.6, 4.7 and 4.11 revealed that gamma band activity is more efficiently elicited at input frequencies in the low theta range around 2-5Hz confirming data published by Butler et al. (2016). *In vivo*, gamma oscillations

are typically phase-locked to an underlying theta oscillation (Buzsaki et al., 1983) suggesting that hippocampal architecture has evolved to perform optimally when inputs arrive within this frequency range. This notion receives further support from single unit recordings displayed in figure 4.11 which indicate that although the overall amount of recorded units during gamma is independent of stimulation frequency, the temporal precision relative to the input phase is highest at theta frequencies. This could mean that the pool of available neurons in CA1 is bundled into gamma cycle-associated groups of neurons most effectively at theta inputs. Interestingly, long-term potentiation paradigms have also been reported to exert the strongest effect at theta stimulation frequency (Grover et al., 2009; Larson and Munkacsy, 2015) thus implying that synaptic plasticity occurs preferentially at this input rate. Although it has been reported early on by Dunwiddie and Lynch (1978) that intraburst stimulation frequencies of 33-100Hz appear to elicit stronger long-term potentiation compared to lower frequency inputs, the data provided by Larson and Munkacsy (2015) suggest that synaptic plasticity is even more efficiently induced when these bursts were separated by 200ms time windows. Therefore, it appears that both burst frequency as well as interburst interval play an important role for plastic changes. It is known that theta/gamma interaction is crucial for normal mnemonic performance (Tort et al., 2009) and the findings presented here contribute to the understanding of this phenomenon. Another unexpected observation was that gamma frequency increased with higher input frequency up to about 8Hz (shown for example in figure 4.6 (A)) after which it drops dramatically. The increase in gamma rhythm means that gamma cycles are either more temporally compressed or that more gamma cycles are superimposed onto a stimulation period. With regard to the data shown in 4.6, the number of gamma cycles per stimulation period ranges from 50 (at 1Hz stimulation frequency) to around 7 (at 8Hz stimulation frequency) which coincides with the proposed maximum number of gamma cycles that can be fit onto a physiological theta period (Jensen and Lisman, 2005). It appears that at stimulation frequencies above 8Hz this mechanism fails due to destructive interference which is why the frequency of evoked gamma decreases drastically. At the highest input rhythms (30/40Hz) the feedback synchronisation could be overridden so that neurons passively pursue the imposed frequency.

The fact that stimulation of CA3a apparently evokes higher power gamma rhythms compared to CA3b/c (see figure 4.8) is most likely due its higher relative recurrent connectivity (Ishizuka et al., 1990; Li et al., 1994) and the fact that CA3a pyramidal cells have a higher propensity of burst firing (Bilkey and Schwartzkroin, 1990; Jarsky et al., 2008) This causes increased local excitability so that a larger number of neurons can be recruited to participate in the evoked LFP resulting in increased gamma power. In this context, it might be insightful to also study each

subregion's ability to evoke SPW-R because it has bee shown that CA3c is most prominently connected to CA1 compared to the other subregions (de Almeida et al., 2007; Oliva et al., 2016).

Taken together, the data presented here illustrate that gamma oscillations emerge in response to prolonged stimulation of hippocampal pyramidal cells. The rhythm appears to be most efficiently generated at theta input frequencies and seems to emerge instantaneously. Furthermore, evoking gamma oscillations apparently suppresses endogenously produced SPW-R suggesting different causal network mechanisms.

5.2 Implications for Hippocampal Sharp Wave-Ripples

As one of the first findings reported here, it was shown that a short (5ms) square pulse of light applied to the pyramidal cell layer of CA3a evokes an LFP in CA1 which very closely resembles an SPW-R (see figure 4.1 or 4.3). The synchronous bout of excitation elicited by this short optogenetic activation probably recruits a similar mechanism which is responsible for spontaneous SPW-R generation because there is hardly any difference in the main features of evoked and spontaneous SPW-R (see figure 4.10). The lower number of units per SPW-R in the evoked case may be explained by the more synchronous input caused by optogenetic stimulation which may lead to more enhanced co-activity of single units. Typically, an SPW-R is brought about by a synchronised population event triggered in CA3 which then exerts glutamatergic excitation on CA1 apical dendrites that is accompanied by a ripple oscillation in the pyramidal cell layer (Girardeau and Zugaro, 2011). Recently, it was demonstrated that ripples are accompanied by inhibitory currents which occur in phase with ripple frequencies whereas excitatory inputs to not correlate with ripple cycles (Gan et al., 2017). In the experiments shown here, the population event is induced by light flashes. Interestingly, Keller et al. (2015) have shown that electrical stimulation of certain areas of the DG also leads to SPW-R generation in CA1 and that evoked SPW-R appear to be highly similar in terms of morphology. Although the similarity of optogenetically evoked SPW-R was not systematically examined in this thesis, it appears that using CA3a optogenetic stimulation elicits SPW-R with a higher degree of variation. This is most likely caused by the fact that a rather large area of CA3 containing potentially thousands of neurons is activated so that at each light pulse a different subgroup of cells is activated. Another intriguing property of optogenetically evoked SPW-R is that they are more readily elicited at low stimulus intensities (see figure 4.9). At higher laser power, the LFP seems to reflect more

a hypersynchronised field excitatory postsynatptic potential following a population spike. The implication of this finding may be that feed forward inhibitory potentials which are crucial for ripple generation are suppressed in presence of excessive excitation and that recruited feedback inhibition prevents formation of oscillations for a certain time frame.

It should furthermore be addressed how the potential number of optogenetically activated cells approximated in figure 4.17 could affect the generation of SPW-R. The results reported here indicate that roughly 2000 neurons could potentially be recruited by optogenetic stimulation in CA3a. However, due to variations in expression strength among cells and relatively precise z-directional beam focussing (Favre-Bulle et al., 2015) by holographic illumination, the actual number of neurons driven above threshold is likely to be much lower. According to Csicsvari et al. (2000), about 10% of all hippocampal neurons are active during any given SPW-R but the number of active neurons needed to evoke an SPW-R is probably much lower. Bazelot et al. (2016) have even shown that driving a single pyramidal cell in CA3 can evoke SPW-R and that variability of evoked events was much lower compared to spontaneous ones. Together with the findings of Keller et al. (2015), it appears that SPW-R variability is governed by the amount of cells which initiate the event. Using the data at hand, it seems clear that irregularity is higher when stimulating a large number of cell optogenetically. Nevertheless, applying a very low stimulation intensity as shown in figure 4.9 could cause only a handful of cells to be activated which are most sensitive to light.

In conclusion, it could be shown that SPW-R can be induced in CA1 by weak, synchronous optogenetic stimulation of CA3a pyramidal cells. Features of spontaneous and evoked SPW-R did not differ significantly implying that similar mechanisms are triggered. The exact number of cells required for successful SPW-R generation could not be resolved but it is likely to be in the range of a 10s of cells.

5.3 Switch Mechanisms

The work presented here is aimed at elucidating the mechanisms responsible for the transition of the different oscillatory states in the hippocampus. As previously mentioned, the two most prominent patterns of activity in the hippocampus are SPW-R and theta/gamma complexes (Colgin, 2016).

A highly interesting study published by Schlingloff et al. (2014) proposes that ripple and gamma oscillations are mediated by two different local network mechanisms. As presented in figure 5.1 (left), ripples may be generated by a local network of inhibitory PV^+ interneurons which receive bouts of excitation from recurrently connected pyramidal cells. This causes a synchronisation of interneurons to a ripple

frequency due to very short synaptic time constants between these cells (Hu et al., 2014) which is then projected back onto pyramidal cells causing ripple phase-locked firing. Schlingloff et al. (2014) suggest that a refractory component caused by this strong inhibitory input is responsible for the intermittent occurrence of SPW-R. On the other hand, gamma oscillations may be generated by the aforementioned PING mechanism (see figure 5.1, right) which requires constant drive for maintaining the back and forth interaction between pyramidal cells and interneurons.

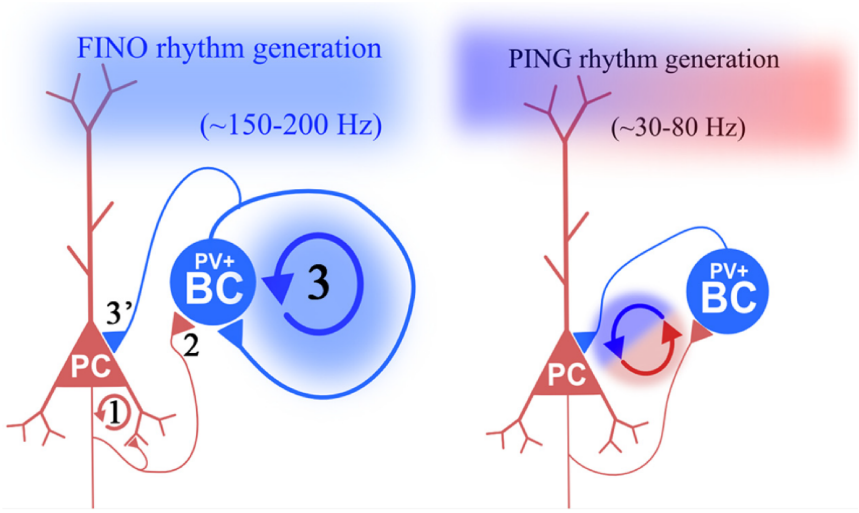

Figure 5.1: Putative local network mechanisms responsible for generation of ripple and gamma oscillations. *(Left) Fast interneuron oscillation (FINO) mechanism possibly responsible for ripple generation. Excitatory activity is reinforced in the recurrent network of CA3 for example (1) which is projected onto networks of PV^+ basket cells (BCs) (2). They in turn synchronise to a ripple rhythm due to short time constants of reciprocal inhibition among each other (3) and release this phase-locked inhibition pattern onto pyramidal cells (3'). (Right) Pyramidal-interneuron gamma (PING) mechanism possibly underlying gamma rhythms. A local feedback inhibition network consisting of excitatory projections from pyramidal cells onto interneurons and inhibitory synapses from interneurons on pyramidal cells generates gamma cycles depending on the synaptic time constants. Note that in the FINO mechanism, individual cycles of the oscillation are maintained within groups of the same cell type whereas in the PING mechanism one cycle represents one round of interaction of interneurons and pyramidal cells. Reprinted with permission of the Society for Neurosciences from Schlingloff et al. (2014).*

The data presented here confirm the findings of Schlingloff et al. (2014) and could be used as an extension of their proposed local network mechanisms. For example, it could be argued that a short square-pulse activation of pyramidal cells triggers the fast interneuron oscillation (FINO) mechanism which then outputs an SPW-R in CA1. Mechanistically, this could be mediated by non-linear dendritic integration which causes a very brief overshoot of feed forward excitation that recruits CA1 pyramidal cells at a very high frequency and is quickly captured by built-up inhibition. In support of this notion, Jahnke et al. (2015) proposed computational frameworks for the generation of SPW-R for which dendritic spikes which

are known to occur in pyramidal cells (Nevian et al., 2007), are a central component. In contrast to that, driving pyramidal cells persistently with a sinusoidal, ramp or prolonged square pulse activates the PING generator leading to persistent gamma oscillations. This may be caused by pronounced inhibition allowing merely short windows of opportunity resulting in a slower oscillation. The proposed refractory period in the FINO model could serve as an explanation for the observation that applying a prolonged square pulse stimulation evokes an SPW-R at stimulus onset which is followed by a gamma rhythm (see figure 4.16). The lack of input synchronicity may thus be causal for not activating dendritic spiking. Therefore, this might explain why ripple oscillations can only be maintained for a short period of time while gamma oscillations can occur continually.

The results obtained from whole-cell recordings showed that induction of gamma rhythms seemingly occurs in a step-like fashion (see figure 4.13 (D) and (E)) around 200ms after onset of a ramp stimulation. This near instantaneous switch of the network state is accompanied by a sharp increase in both inhibitory and excitatory postsynaptic currents. In the context of information processing within the network, this mechanism could mediate a clear-cut separation of information acquisition (theta/gamma) and consolidation modes (SPW-R). It may be beneficial for local networks to operate in such an either-or-manner as this may increase flexibility of cognitive states. Furthermore, one could speculate that the different gamma bands behave differently in this framework as they possibly convey different sensory or intrinsic information. However, in order to disentangle these relationships further experiments would have to carried out.

The persistent or prolonged excitatory drive that may be required for driving the PING mechanism may originate *in vivo* from septal cholinergic inputs. It has been shown *in vivo* that theta oscillations are generated in the presence of high cholinergic tone mediated by afferents originating in the medial septum (Buzsaki, 1989). On the other hand, SPW-R are expressed in behavioural states associated with low acetylcholine levels (Gais and Born, 2004) suggesting the presence of an intrinsic generator network for SPW-R. However, the importance of external cholinergic drive for the network state transition has been questioned by Goutagny et al. (2009) who demonstrated spontaneous, atropine resistant theta oscillations in an *in vitro* whole hippocampal preparation. Interestingly, their preparation exhibited a "pure" theta rhythm without any superimposed gamma activity. The results reported here show that driving excitatory cells in the hippocampus persistently or in a slow phasic manner causes the network to synchronise to a gamma band rhythm. It may be possible that in order to generate gamma band activity, the network simply requires persistent input of any sort which incidentally *in vivo* is carried by cholinergic fibers from the septum. The fact that cholinergic cells predominantly form diffuse, i.e.

not cell type specific terminals in the hippocampus (Aznavour et al., 2002) and that acetylcholine receptors, both muscarinic and nicotinic are widely expressed across a variety of inhibitory and excitatory cell types (Teles-Grilo Ruivo and Mellor, 2013) supports this hypothesis. Thus, it could be argued that the persistent optogenetic activation of pyramidal cells described here imitates this "background" persistent excitatory drive which causes the local feedback network to synchronise. In the absence of this tonic input, the hippocampus returns to its default state in which it is thought that population spikes are generated intermittently within the recurrent CA3 or CA2 network (Oliva et al., 2016) that are transmitted towards CA1 as SPW-R. This notion is supported by observations that recurrent synapses in CA3 are suppressed by increased cholinergic tone (Hasselmo, 2006). Applying a short light flash to CA3 as shown in figure 4.1 might imitate the highly synchronised input brought by CA3 population spikes. The work of Stark et al. (2014) has also provided evidence that optogenetic stimulation of pyramidal cells *in vivo* can evoke high frequency oscillations in the ripple band even if the stimulus was applied as a short arched time course and not as a square pulse. However, they still applied relatively short pulses of <100ms length and the results shown in figure 4.16 suggest that the wave form and duration of the stimulus input is critical for the generation of either gamma or SPW-R. Apart from cholinergic fibers, the medial septum also sends both glutamatergic and GABAergic axons towards the hippocampal-entorhinal formation (Justus et al., 2017; Fuchs et al., 2016; Fuhrmann et al., 2015) which have been associated with generating theta rhythms in the hippocampus or controlling grid cell activity in the medial entorhinal cortex. However, it is unclear whether these projections play a role for the emergence of gamma rhythms or SPW-R.

The importance of GABAergic inhibition for the two network states could not be addressed in a cell-specific manner within this thesis. However, it was shown that inhibitory postsynaptic currents may contribute to a larger extent to the maintenance of gamma oscillations as they occur with a much higher frequency compared to excitatory currents (see figure 4.13 (E)). Previous work by Gan et al. (2017) suggests that inhibitory inputs are also more pronounced than excitatory ones during SPW-R. In this study, the authors could show in awake mice that cells receive around 4-fold larger inhibitory conductances and that IPSCs are phase-locked to ripples whereas EPSCs are not. The data presented here suggest that while the excitation/inhibition balance is also shifted to the inhibitory side during gamma, both IPSCs and EPSCs are phase-locked to the local field potential gamma oscillation. However, a more detailed analysis of the temporal relationship of cellular and network contributions is necessary to make a more precise statement on that matter. Moreover, synaptic currents during evoked and spontaneous SPW-R and their relationship to the LFP needs to be evaluated to obtain a broader scope of the

network switch.

Another observation presented here is that SPW-R and gamma oscillations appear to be mutually exclusive. This is most prominently displayed in figure 4.12 which shows that ripple power decreases while gamma power rises in response to less synchronised but more persistent excitatory drive. Interestingly, other studies have indicated that both types of network patterns appear to influence each other. Reports of Bieri et al. (2014) and Carr et al. (2012) have provided evidence of a transient increase in slow gamma power (∼30Hz) as well as CA3-CA1 gamma synchrony around the peak of SPW-R and have highlighted the importance of this phenomenon for replay of place cell sequences. This could mean that ripple and gamma rhythms are governed by different mechanisms which do not interfere with each other. However, the results shown in figure 4.13 (B) and (C) show that in some cases, although the network has already shifted to generating a gamma pattern, it is occasionally interspersed by SPW-R and the associated postsynaptic currents. These sporadic observations need to be addressed in a more detailed manner as they may provide hints for extending the findings of Bieri et al. (2014) and Carr et al. (2012).

5.4 Methodological Aspects

5.4.1 Transgene Expression with Serotype 5 AAVs

AAV5 was chosen because it is known to preferentially infect neuronal cells (Burger et al., 2004) and it spreads fairly wide throughout neural tissue when applied intracranially (Burger et al., 2004; Aschauer et al., 2013) whilst yielding high expression levels (Burger et al., 2004). A widespread and strong expression of ChR2 was desirable for the experiments described here because the induction and maintenance of optogenetically elicited network patterns should be assessed in a region specific manner. Since the holographic illumination system allows highly precise delivery of light, it was possible to determine the contributions of each region to the network oscillation within a single ongoing experiment. This eliminated the need for highly localised injection of the viral vector to the region of interest for subregional characterisation thereby reducing the number of experimental animals used.

Nevertheless, some details about AAV mediated gene transfer remain open. For example, until today it is poorly understood how AAVs gain access to the cytosol. While there is correlative evidence linking the presence of surface proteins such as the platelet-derived growth factor receptor (PDGF-R) or 2,3-linked sialic acid to successful virus entry (Di Pasquale et al., 2003; Walters et al., 2001), it is unclear how their cell-type specific expression pattern influences virus mediated transduction. For example, it has been shown that PDGF-R is expressed in both neuronal and glial cells

(Nait Oumesmar et al., 1997), so it is feasible that the glial population is also affected by viral infection, albeit the use of the neuron-specific CamKIIα promoter probably prevents functional expression of ChR2. Furthermore, since PDGF-R is expressed in somatic as well as dendritic and even axonal neuronal domains (Nait Oumesmar et al., 1997), it is possible that viruses enter a cell at distal parts and deliver their genome through retrograde transport. This circumstance complicates any statement about whether the observed expression patterns are due to transgene production by local cells or by cells which project to the targeted region. It could be conceivable that evoked LFPs do not spread along the canonical trisynaptic pathway but that other pathways invading the hippocampus may be unspecifically activated. The possibility that axons originating from cells located in the medial septum for example take up the virus and express ChR2 which are then sensitive to optogenetic stimulation cannot be entirely ruled out. However, as axons from extrahippocampal regions are severed during the slicing procedure, this scenario may be unlikely but it cannot be ruled out with certainty that these sectioned axons retain the ability to release transmitters. A possible solution for this problem could be to use a soma targeted ChR2 variant that was reported by Baker et al. (2016) which restricts expression of the optogenetic construct to (peri)somatic domains this facilitating targeting of cells and distinction of ChR2 positive and negative cells.

5.4.2 Properties of the Expression Construct

The use of CaMKIIα-hChR2(H134R)-EYFP may also pose a confounding factor. The CaMKIIα promoter was chosen because optogenetically evoked gamma oscillations are most likely generated by a PING mechanism according to Butler et al. (2016). Therefore, since CaMKIIα appears specific for excitatory projection neurons, i.e. pyramidal cells in the hippocampus (Wang et al., 2013), it allowed for exclusive stimulation of this cell type. However, CaMKIIα has been shown to leak to other cell types. For example, immunofluorescence studies in mice (Nathanson et al., 2009) and marmosets (Watakabe et al., 2015) have provided evidence that about 20% of transgene expressing cells were inhibitory when using the CaMKIIα promoter. This observation received further support by Butler et al. (2016) who reported functional expression of ChR2 in GABAergic neurons as a secondary finding. The significance of this for the data presented here is difficult to evaluate as there is currently no experimental paradigm to restrict expression exclusively to excitatory neurons. One could however opt to use an interneuron specific promoter such as PV and apply a sinusoidal or ramp-like stimulation pattern as described here. Since the PV promoter is much more specific (Klausberger et al., 2005), this may answer the question whether excitatory neurons are necessary for gamma induction. After all, it

is difficult to rule out that low level interneuronal ChR2 expression is indispensable for the evoked network phenomena.

The H134R mutant of ChR2 was used because it was readily available from the vector core of UNC and its properties very well described in the literature (Berndt et al., 2011; Lin et al., 2009). It is used as a "general purpose" variant of ChR2 as it combines large enough stationary photocurrents with fairly fast kinetics (∼4ms on, ∼15ms off (Berndt et al., 2011)). ChR2 variants with faster kinetics usually suffer from smaller photocurrents which requires higher stimulation intensities that may cause phototoxicity (Mattis et al., 2012; Yizhar et al., 2011). Therefore, the H134R mutant with its theoretical frequency limit of 50-70Hz was deemed appropriate for eliciting oscillations in the gamma band. This also provides strong evidence against the notion that the observed resonance properties shown in figure 4.6 or 4.7 may be caused by the biophysical limitations of the used ChR2 mutant. Additionally, since the prolonged stimulation paradigms described here cause a steady photocurrent, the frequency of evoked oscillations most likely depends on intrinsic firing properties of neurons in the local network. It furthermore supports the feasibility that the local field potential follows input frequency at 30Hz or 40Hz as displayed for example in figure 4.6.

It should be noted here that the 515nm line of the imaging laser overlaps with the excitation spectrum of ChR2 (Mattis et al., 2012) which did cause unwanted activation of ChR2 when expression of EYFP was assessed. However, imaging periods were kept very short so that no noticeable excitotoxic effects could be seen. To mitigate this problem, one could use a ChR2-mCherry construct in future experiments. Lastly, it has to be stated that expression levels varied from mouse to mouse which may serve as an explanation for insufficient transfer of activity between hippocampal subregions in some slices. Expression levels had to be set sufficiently high to elicit the observed effects but low enough to avoid overexpression and associated neurotoxic damage (Miyashita et al., 2013).

5.4.3 MEA Recordings and Holographic Illumination

Since the methods for recording and stimulation described in this thesis are fairly complex and novel, possible issues and their significance should be discussed. First of all, using a MEA for LFP recordings on the one hand is advantageous because it allows thorough analysis of activity in many regions of the hippocampus simultaneously. For example, Kim et al. (2016) have shown that these complex datasets can be used to obtain planar current-source densities which in turn reveals real-time functional connectivity in the hippocampal formation during physiological activity. On the other hand, the necessity of using submerged conditions for MEA record-

ings did have a noticeable impact on the recording environment. Most notably, there was a relatively drastic reduction in SPW-R occurrence (0.6±0.3Hz in MEA vs. 3±1Hz in interface (value obtained from Maier et al. (2003))) and amplitude (28±11μV in MEA vs. 0.27±0.03mV in interface (value obtained from Maier et al. (2016))) compared to interface conditions. These differences can be explained by the improved oxygen supply of interface chambers allowing more efficient metabolic conversion of nutrients. Additionally, as depicted in figures 4.14, 4.15 and 4.16, gamma power markedly decreases towards the end of a 5s stimulation period. This effect is amplified when using high laser powers of more than 3mW/mm^2. This observation is much less pronounced in interface conditions where stimulation periods of even 30s do not appear to have any detrimental effects on slice physiology (as reported by Martin Kaiser and Justus Schneider). Nevertheless, because of the high signal-to-noise ratios and the fact that ripple frequency did not suffer dramatically in submerged conditions (196±28Hz in MEA vs. 210±16Hz in interface (value obtained from Maier et al. (2003))), the use of MEA systems for multiplexed recordings especially using double perfusion (Hajos et al., 2009; Maier et al., 2009) remains a viable option.

The usage of spatial light modulators for laser beam shaping in optogenetic experimental settings has gained a lot of attention in recent times. In comparison to digital micromirror device based approaches, SLMs offer greatly improved axial focussing and thereby make more efficient use of incident light (Favre-Bulle et al., 2015). Several studies published by Emiliani and colleagues have evaluated the possibilities of using SLMs for precisely delivering light in three dimensions for optogenetic stimulation or for improved fluorescence imaging (Szabo et al., 2014; Papagiakoumou et al., 2010). According to the study of Szabo et al. (2014), it is possible to limit illumination to a single cell which is confirmed by simulations of Favre-Bulle et al. (2015) who propose that volumes of even submicrometer size can theoretically be achieved. Nevertheless, the critical limiting factor of light scattering in brain tissue needs to be addressed. Al-Juboori et al. (2013) and Yona et al. (2016) have provided theoretical and experimental frameworks showing that light intensity drops according to an exponential function in z-direction which means that already at 100μm depth only about 30% of the initial power is retained. In regard to the experiments described here, this implies that although the illumination system appears very accurate in the horizontal plane, scattered laser light may reach cells which are not part of the AOI. This could in turn mean that using a higher laser power may not only drive stronger firing of cells within the AOI but that also more neurons are recruited because of scattered light. A surprising finding in connection with this is that the frequency of evoked gamma oscillations is positively correlated (albeit weakly) with laser power as shown in figure 4.4 and 4.5. One would expect

that recruiting a greater number of cells and therefore a larger network causes a slowing of oscillation as there is an inverse relationship between network size and locally recordable LFP frequencies (Buzsaki and Draguhn, 2004). Another possible source of variation is that AOIs were generated from freehandedly drawn polygonal areas which could result in different AOI sizes from slice to slice. As displayed in figure 3.4, the size of the AOI directly affects the local laser intensity although the effects are probably negligible. After all, the problem of light scattering could be solved by using two-photon optics or a second SLM as reported by Hernandez et al. (2016). The variable laser output power could be easily corrected by implementing a calibration factor which adjusts input voltage to the calculated area of the AOI. Another factor that has to be taken into account in optogenetic experiments is phototoxicity caused by prolonged laser exposure. This circumstance was especially important since the experiments were carried out in submerged conditions in which metabolites may accumulate more easily. However, since stimulation and imaging periods were kept fairly short (typically less than 15s), phototoxic effects are very likely to be minimal.

Lastly, the strengths and weaknesses of the present *in vitro* preparation should be discussed. The main advantage of using a reduced system of a hippocampal slice preparation over *in vivo* approaches is the ability to precisely control the experimental environment. It is furthermore much easier to obtain robust single cell recordings. Although interhemispheric and interregional connections are severed during slicing, it appears that the circuitry necessary for generating SPW-R and gamma oscillations remains intact to a reasonable extent. Nonetheless, there are apparent differences in network signatures. For one, SPW-R in slices are accompanied by a large positive LFP deflection in CA1 *stratum pyramidale* which is more variable in *in vivo* recordings. Furthermore, it is known that ripple oscillations *in vivo* in general have a lower frequency (Buzsaki, 2015). These differences may be caused by an altered cellular composition or a restructuring process following slice preparation. With regards to gamma oscillations, it is thought that different gamma bands originate from different sources (Scheffer-Teixeira et al., 2012; Belluscio et al., 2012). For example, medium and high frequency gamma oscillations (>60Hz) may originate from the EC (Scheffer-Teixeira et al., 2012). Since the connections between the EC and the CA1 area are usually not preserved in the slicing procedure reported here, it may not be possible to optogenetically recreate entorhinal inputs to CA1. However, this notion was not thoroughly investigated, so an adapted slicing protocol might provide insights into that issue. To sum up, although acute slices represent a reduced system compared to the intact brain, an *in vitro* approach offers remarkably favourable conditions for the investigation of cellular and network mechanisms.

5.5 Outlook

Although the work presented here provides basic clues about how neuronal networks achieve the transition between different states, some questions remain unsolved and require further investigation. Therefore, this section will provide ideas for future experiments and analyses which could contribute to a more detailed understanding of the state switch.

While the dynamics of postsynaptic currents during evoked gamma oscillations could be described here in rudimentary fashion, a more accurate analysis of the time course of the synchronisation will be necessary to make a more conclusive statement about the involvement of synaptic activity in gamma. It could be shown that the frequency of PSCs increases sharply after stimulus onset but we hypothesise that these currents initially occur in an unordered manner which becomes more and more rhythmic with increasing time stimulation intensity. This notion could for example be assessed by calculating the cross correlations or the entropy of the PSCs which we expect to decrease once the network has generated a gamma rhythm. In addition the data of the patch-clamp experiments described here did not include an analysis of PSCs during SPW-R which are essential for making a comment on the differences in synaptic activity during the network states.

As mentioned before, the exact sources of GABAergic inhibition and its importance for the emergence of gamma and SPW-R could unfortunately not be determined here. In order to achieve a more comprehensive picture on his issue, it could be insightful to modulate GABAergic inhibition pharmacologically by for example gabazine or diazepam. This intervention might influence the frequency of gamma oscillations or the time until gamma entrainment has developed. Furthermore, uncovering the type(s) of interneurons and their involvement in the observed network oscillations is necessary. The use of cell-type specific Cre-mouse lines may prove highly useful in this undertaking. A possible experiment could include driving or inhibiting interneurons optogenetically with simultaneous single-cell recordings to disambiguate the contributions of each cell-type to the field potential and to local synaptic activity.

We hypothesise that an important cellular mechanism responsible for recruitment of the FINO generator which triggers ripple band activity is supralinear dendritic integration. This mechanism could explain why SPW-R are only evoked when stimulation is delivered with a sharp rising edge. Finding direct evidence for that could be achieved by for example observing dendritic activity with localised patch-clamp recordings or calcium imaging methods which could reveal differences in activity during network states.

There are also some possibilities for exploiting the patterned illumination system

for more thorough investigations. For example, in order to gain a more precise idea of the number of cells which are active during each state it would be feasible to "ramp up" the stimulation intensity by detecting somata of single cells on-line and directing illumination to an increasing number of single cells in a stochastic fashion. With a few changes to the experimental paradigm (soma restricted expression of ChR2 (Baker et al., 2016), implementation of automated detection algorithms, delivery of light in three dimensions), this could prove a very useful tool for the interrogation of networks mechanisms. Along those lines, the SLM system could also be used for structured illumination microscopy since it can easily be used to generate grid-like illumination patterns which grant increased spatial resolution (Chang et al., 2009).

Lastly, since all electrophysiological data presented here were recorded with a MEA system, it may be possible to apply the algorithims published by Kim et al. (2016) which allow mapping the functional connectivity within the slice network based on current-source-density analyses. These data could reveal differences in local connectivity depending on the network state and might even expose a clear shift of co-active regions upon triggering the switch. However, it first has to be validated that the density of MEA electrodes is sufficiently high to distinguish individual subregions of the hippocampus. If this is not the case, using a higher density MEA would solve this problem. Connectivity or co-activity patterns could also be assessed by calcium imaging methods. Assuming that SPW-R are accompanied by activity of neuronal ensembles which are imprinted during previous theta/gamma periods, it would be intriguing to see whether the activity pattern changes from gamma to SPW-R and whether the composition of co-active neurons changes sustainably after prolonged induction of a gamma rhythm. Such experiments may generate highly relevant insights about the role of long-term plastic changes for information processing in hippocampal networks.

6 References

Al-Juboori SI, Dondzillo A, Stubblefield EA, Felsen G, Lei TC, and Klug A. Light scattering properties vary across different regions of the adult mouse brain. *PLoS One*, 2013; 8(7):e67626.

Amaral DG. A golgi study of cell types in the hilar region of the hippocampus in the rat. *J Comp Neurol*, 1978; 182(4 Pt 2):851–914.

Amaral DG and Witter MP. The three-dimensional organization of the hippocampal formation: a review of anatomical data. *Neuroscience*, 1989; 31(3):571–91.

Andersen P. *The hippocampus book*. Oxford University Press, Oxford; New York, 2007. ISBN 0195100271 9780195100273.

Annese J, Schenker-Ahmed NM, Bartsch H, Maechler P, Sheh C, Thomas N, Kayano J, Ghatan A, Bresler N, Frosch MP, Klaming R, and Corkin S. Postmortem examination of patient h.m.'s brain based on histological sectioning and digital 3d reconstruction. *Nat Commun*, 2014; 5:3122.

Aronov D, Nevers R, and Tank DW. Mapping of a non-spatial dimension by the hippocampal-entorhinal circuit. *Nature*, 2017; 543(7647):719–722.

Aschauer DF, Kreuz S, and Rumpel S. Analysis of transduction efficiency, tropism and axonal transport of aav serotypes 1, 2, 5, 6, 8 and 9 in the mouse brain. *PLoS One*, 2013; 8(9):e76310.

Augustinack JC, van der Kouwe AJ, Salat DH, Benner T, Stevens AA, Annese J, Fischl B, Frosch MP, and Corkin S. H.m.'s contributions to neuroscience: A review and autopsy studies. *Hippocampus*, 2014; 24(11):1267–86.

Axmacher N, Elger CE, and Fell J. Ripples in the medial temporal lobe are relevant for human memory consolidation. *Brain*, 2008; 131(Pt 7):1806–17.

Aznavour N, Mechawar N, and Descarries L. Comparative analysis of cholinergic innervation in the dorsal hippocampus of adult mouse and rat: a quantitative immunocytochemical study. *Hippocampus*, 2002; 12(2):206–17.

Bahner F, Weiss EK, Birke G, Maier N, Schmitz D, Rudolph U, Frotscher M, Traub RD, Both M, and Draguhn A. Cellular correlate of assembly formation in oscillating hippocampal networks in vitro. *Proc Natl Acad Sci U S A*, 2011; 108(35):E607–16.

Baker CA, Elyada YM, Parra A, and Bolton MM. Cellular resolution circuit mapping with temporal-focused excitation of soma-targeted channelrhodopsin. *Elife*, 2016; 5.

Barry PH. Jpcalc, a software package for calculating liquid junction potential corrections in patch-clamp, intracellular, epithelial and bilayer measurements and for correcting junction potential measurements. *J Neurosci Methods*, 1994; 51(1):107–16.

Bartos M, Vida I, and Jonas P. Synaptic mechanisms of synchronized gamma oscillations in inhibitory interneuron networks. *Nat Rev Neurosci*, 2007; 8(1):45–56.

Bazelot M, Telenczuk MT, and Miles R. Single ca3 pyramidal cells trigger sharp waves in vitro by exciting interneurones. *J Physiol*, 2016; .

Belluscio MA, Mizuseki K, Schmidt R, Kempter R, and Buzsaki G. Cross-frequency phase-phase coupling between theta and gamma oscillations in the hippocampus. *J Neurosci*, 2012; 32(2):423–35.

Berndt A, Schoenenberger P, Mattis J, Tye KM, Deisseroth K, Hegemann P, and Oertner TG. High-efficiency channelrhodopsins for fast neuronal stimulation at low light levels. *Proc Natl Acad Sci U S A*, 2011; 108(18):7595–600.

Bieri KW, Bobbitt KN, and Colgin LL. Slow and fast gamma rhythms coordinate different spatial coding modes in hippocampal place cells. *Neuron*, 2014; 82(3):670–81.

Bilkey DK and Schwartzkroin PA. Variation in electrophysiology and morphology of hippocampal ca3 pyramidal cells. *Brain Res*, 1990; 514(1):77–83.

Bir SC, Ambekar S, Kukreja S, and Nanda A. Julius caesar arantius (giulio cesare aranzi, 1530-1589) and the hippocampus of the human brain: history behind the discovery. *J Neurosurg*, 2015; 122(4):971–5.

Bliss TV and Lomo T. Long-lasting potentiation of synaptic transmission in the dentate area of the anaesthetized rabbit following stimulation of the perforant path. *J Physiol*, 1973; 232(2):331–56.

Both M, Bahner F, von Bohlen und Halbach O, and Draguhn A. Propagation of specific network patterns through the mouse hippocampus. *Hippocampus*, 2008; 18(9):899–908.

Boyden ES, Zhang F, Bamberg E, Nagel G, and Deisseroth K. Millisecond-timescale, genetically targeted optical control of neural activity. *Nat Neurosci*, 2005; 8(9):1263–8.

Brunel N and Wang XJ. What determines the frequency of fast network oscillations with irregular neural discharges? i. synaptic dynamics and excitation-inhibition balance. *J Neurophysiol*, 2003; 90(1):415–30.

Burger C, Gorbatyuk OS, Velardo MJ, Peden CS, Williams P, Zolotukhin S, Reier PJ, Mandel RJ, and Muzyczka N. Recombinant aav viral vectors pseudotyped with viral capsids from serotypes 1, 2, and 5 display differential efficiency and cell tropism after delivery to different regions of the central nervous system. *Mol Ther*, 2004; 10(2):302–17.

Butler JL, Mendonca PR, Robinson HP, and Paulsen O. Intrinsic cornu ammonis area 1 theta-nested gamma oscillations induced by optogenetic theta frequency stimulation. *J Neurosci*, 2016; 36(15):4155–69.

Buzsaki G. Hippocampal sharp waves: their origin and significance. *Brain Res*, 1986; 398(2):242–52.

Buzsaki G. Two-stage model of memory trace formation: a role for "noisy" brain states. *Neuroscience*, 1989; 31(3):551–70.

Buzsaki G. Theta rhythm of navigation: link between path integration and landmark navigation, episodic and semantic memory. *Hippocampus*, 2005; 15(7):827–40.

Buzsaki G. Hippocampal sharp wave-ripple: A cognitive biomarker for episodic memory and planning. *Hippocampus*, 2015; 25(10):1073–188.

Buzsaki G and Draguhn A. Neuronal oscillations in cortical networks. *Science*, 2004; 304(5679):1926–9.

Buzsaki G, Leung LW, and Vanderwolf CH. Cellular bases of hippocampal eeg in the behaving rat. *Brain Res*, 1983; 287(2):139–71.

Buzsaki G, Logothetis N, and Singer W. Scaling brain size, keeping timing: evolutionary preservation of brain rhythms. *Neuron*, 2013; 80(3):751–64.

Buzsaki G and Moser EI. Memory, navigation and theta rhythm in the hippocampal-entorhinal system. *Nat Neurosci*, 2013; 16(2):130–8.

Buzsaki G, Ponomareff GL, Bayardo F, Ruiz R, and Gage FH. Neuronal activity in the subcortically denervated hippocampus: a chronic model for epilepsy. *Neuroscience*, 1989; 28(3):527–38.

Buzsaki G and Wang XJ. Mechanisms of gamma oscillations. *Annu Rev Neurosci*, 2012; 35:203–25.

Cardin JA, Carlen M, Meletis K, Knoblich U, Zhang F, Deisseroth K, Tsai LH, and Moore CI. Driving fast-spiking cells induces gamma rhythm and controls sensory responses. *Nature*, 2009; 459(7247):663–7.

Carr MF, Karlsson MP, and Frank LM. Transient slow gamma synchrony underlies hippocampal memory replay. *Neuron*, 2012; 75(4):700–13.

Cetin A, Komai S, Eliava M, Seeburg PH, and Osten P. Stereotaxic gene delivery in the rodent brain. *Nat Protoc*, 2006; 1(6):3166–73.

Chang BJ, Chou LJ, Chang YC, and Chiang SY. Isotropic image in structured illumination microscopy patterned with a spatial light modulator. *Optics express*, 2009; 17(17):14710–14721.

Chen CM, Stanford AD, Mao X, Abi-Dargham A, Shungu DC, Lisanby SH, Schroeder CE, and Kegeles LS. Gaba level, gamma oscillation, and working memory performance in schizophrenia. *Neuroimage Clin*, 2014; 4:531–9.

Cho YH, Beracochea D, and Jaffard R. Extended temporal gradient for the retrograde and anterograde amnesia produced by ibotenate entorhinal cortex lesions in mice. *J Neurosci*, 1993; 13(4):1759–66.

Cho YH, Kesner RP, and Brodale S. Retrograde and anterograde amnesia for spatial discrimination in rats: Role of hippocampus, entorhinal cortex, and parietal cortex. *Psychobiology*, 1995; 23(3):185–194.

Colgin LL. Rhythms of the hippocampal network. *Nat Rev Neurosci*, 2016; 17(4):239–49.

Colgin LL, Denninger T, Fyhn M, Hafting T, Bonnevie T, Jensen O, Moser MB, and Moser EI. Frequency of gamma oscillations routes flow of information in the hippocampus. *Nature*, 2009; 462(7271):353–7.

Collingridge GL, Kehl SJ, and McLennan H. Excitatory amino acids in synaptic transmission in the schaffer collateral-commissural pathway of the rat hippocampus. *J Physiol*, 1983; 334:33–46.

Corkin S. What's new with the amnesic patient h.m.? *Nat Rev Neurosci*, 2002; 3(2):153–60.

Csicsvari J, Hirase H, Czurko A, Mamiya A, and Buzsaki G. Fast network oscillations in the hippocampal ca1 region of the behaving rat. *J Neurosci*, 1999; 19(16):RC20.

Csicsvari J, Hirase H, Mamiya A, and Buzsaki G. Ensemble patterns of hippocampal ca3-ca1 neurons during sharp wave-associated population events. *Neuron*, 2000; 28(2):585–94.

de Almeida L, Idiart M, and Lisman JE. Memory retrieval time and memory capacity of the ca3 network: role of gamma frequency oscillations. *Learn Mem*, 2007; 14(11):795–806.

Deng W, Aimone JB, and Gage FH. New neurons and new memories: how does adult hippocampal neurogenesis affect learning and memory? *Nat Rev Neurosci*, 2010; 11(5):339–50.

Di Pasquale G, Davidson BL, Stein CS, Martins I, Scudiero D, Monks A, and Chiorini JA. Identification of pdgfr as a receptor for aav-5 transduction. *Nat Med*, 2003; 9(10):1306–12.

Diba K and Buzsaki G. Forward and reverse hippocampal place-cell sequences during ripples. *Nat Neurosci*, 2007; 10(10):1241–2.

Dine J, Genewsky A, Hladky F, Wotjak CT, Deussing JM, Zieglgansberger W, Chen A, and Eder M. Local optogenetic induction of fast (20-40 hz) pyramidal-interneuron network oscillations in the in vitro and in vivo ca1 hippocampus: Modulation by crf and enforcement of perirhinal theta activity. *Front Cell Neurosci*, 2016; 10:108.

Draguhn A, Traub RD, Schmitz D, and Jefferys JG. Electrical coupling underlies high-frequency oscillations in the hippocampus in vitro. *Nature*, 1998; 394(6689):189–92.

Dunwiddie T and Lynch G. Long-term potentiation and depression of synaptic responses in the rat hippocampus: localization and frequency dependency. *J Physiol*, 1978; 276:353–67.

Eacott MJ and Norman G. Integrated memory for object, place, and context in rats: a possible model of episodic-like memory? *J Neurosci*, 2004; 24(8):1948–53.

Ego-Stengel V and Wilson MA. Disruption of ripple-associated hippocampal activity during rest impairs spatial learning in the rat. *Hippocampus*, 2010; 20(1):1–10.

Eichenbaum H, Dudchenko P, Wood E, Shapiro M, and Tanila H. The hippocampus, memory, and place cells: is it spatial memory or a memory space? *Neuron*, 1999; 23(2):209–26.

Ekstrom AD, Kahana MJ, Caplan JB, Fields TA, Isham EA, Newman EL, and Fried I. Cellular networks underlying human spatial navigation. *Nature*, 2003; 425(6954):184–8.

Favre-Bulle IA, Preece D, Nieminen TA, Heap LA, Scott EK, and Rubinsztein-Dunlop H. Scattering of sculpted light in intact brain tissue, with implications for optogenetics. *Sci Rep*, 2015; 5:11501.

Fisahn A, Contractor A, Traub RD, Buhl EH, Heinemann SF, and McBain CJ. Distinct roles for the kainate receptor subunits glur5 and glur6 in kainate-induced hippocampal gamma oscillations. *J Neurosci*, 2004; 24(43):9658–68.

Fisahn A, Pike FG, Buhl EH, and Paulsen O. Cholinergic induction of network oscillations at 40 hz in the hippocampus in vitro. *Nature*, 1998; 394(6689):186–9.

Fortin NJ, Wright SP, and Eichenbaum H. Recollection-like memory retrieval in rats is dependent on the hippocampus. *Nature*, 2004; 431(7005):188–91.

Foster DJ and Wilson MA. Reverse replay of behavioural sequences in hippocampal place cells during the awake state. *Nature*, 2006; 440(7084):680–3.

Fuchs E, Neitz A, Pinna R, Melzer S, Caputi A, and Monyer H. Local and distant input controlling excitation in layer ii of the medial entorhinal cortex. *Neuron*, 2016; 89(1):194–208.

Fuhrmann F, Justus D, Sosulina L, Kaneko H, Beutel T, Friedrichs D, Schoch S, Schwarz MK, Fuhrmann M, and Remy S. Locomotion, theta oscillations, and the speed-correlated firing of hippocampal neurons are controlled by a medial septal glutamatergic circuit. *Neuron*, 2015; 86(5):1253–64.

Gais S and Born J. Low acetylcholine during slow-wave sleep is critical for declarative memory consolidation. *Proc Natl Acad Sci U S A*, 2004; 101(7):2140–4.

Gan J, Weng SM, Pernia-Andrade AJ, Csicsvari J, and Jonas P. Phase-locked inhibition, but not excitation, underlies hippocampal ripple oscillations in awake mice in vivo. *Neuron*, 2017; 93(2):308–314.

Gerchberg RW. A practical algorithm for the determination of the phase from image and diffraction plane pictures. *Optik*, 1972; 35:237–246.

Girardeau G, Benchenane K, Wiener SI, Buzsaki G, and Zugaro MB. Selective suppression of hippocampal ripples impairs spatial memory. *Nat Neurosci*, 2009; 12(10):1222–3.

Girardeau G and Zugaro M. Hippocampal ripples and memory consolidation. *Curr Opin Neurobiol*, 2011; 21(3):452–9.

Golub VM, Brewer J, Wu X, Kuruba R, Short J, Manchi M, Swonke M, Younus I, and Reddy DS. Neurostereology protocol for unbiased quantification of neuronal injury and neurodegeneration. *Front Aging Neurosci*, 2015; 7:196.

Goutagny R, Jackson J, and Williams S. Self-generated theta oscillations in the hippocampus. *Nat Neurosci*, 2009; 12(12):1491–3.

Gradinaru V, Thompson KR, Zhang F, Mogri M, Kay K, Schneider MB, and Deisseroth K. Targeting and readout strategies for fast optical neural control in vitro and in vivo. *J Neurosci*, 2007; 27(52):14231–8.

Grover LM, Kim E, Cooke JD, and Holmes WR. Ltp in hippocampal area ca1 is induced by burst stimulation over a broad frequency range centered around delta. *Learn Mem*, 2009; 16(1):69–81.

Hajos N, Ellender TJ, Zemankovics R, Mann EO, Exley R, Cragg SJ, Freund TF, and Paulsen O. Maintaining network activity in submerged hippocampal slices: importance of oxygen supply. *Eur J Neurosci*, 2009; 29(2):319–27.

Harris KD, Csicsvari J, Hirase H, Dragoi G, and Buzsaki G. Organization of cell assemblies in the hippocampus. *Nature*, 2003; 424(6948):552–6.

Hasselmo ME. The role of acetylcholine in learning and memory. *Curr Opin Neurobiol*, 2006; 16(6):710–5.

Hernandez O, Papagiakoumou E, Tanese D, Fidelin K, Wyart C, and Emiliani V. Three-dimensional spatiotemporal focusing of holographic patterns. *Nat Commun*, 2016; 7:11928.

Hollnagel JO, ul Haq R, Behrens CJ, Maslarova A, Mody I, and Heinemann U. No evidence for role of extracellular choline-acetyltransferase in generation of gamma oscillations in rat hippocampal slices in vitro. *Neuroscience*, 2015; 284:459–69.

Hu H, Gan J, and Jonas P. Interneurons. fast-spiking, parvalbumin(+) gabaergic interneurons: from cellular design to microcircuit function. *Science*, 2014; 345(6196):1255263.

Hu L, Li X, Mu Q, Cao Z, Li D, Liu Y, Peng Z, and Lu X. A polarization independent liquid crystal adaptive optics system. *Journal of Optics*, 2010; 12(4):045501.

Hunsaker MR, Rosenberg JS, and Kesner RP. The role of the dentate gyrus, ca3a,b, and ca3c for detecting spatial and environmental novelty. *Hippocampus*, 2008; 18(10):1064–73.

Ishizuka N, Weber J, and Amaral DG. Organization of intrahippocampal projections originating from ca3 pyramidal cells in the rat. *J Comp Neurol*, 1990; 295(4):580–623.

Jahnke S, Timme M, and Memmesheimer RM. A unified dynamic model for learning, replay, and sharp-wave/ripples. *J Neurosci*, 2015; 35(49):16236–58.

Jarsky T, Mady R, Kennedy B, and Spruston N. Distribution of bursting neurons in the ca1 region and the subiculum of the rat hippocampus. *J Comp Neurol*, 2008; 506(4):535–47.

Jensen O and Lisman JE. Hippocampal sequence-encoding driven by a cortical multi-item working memory buffer. *Trends Neurosci*, 2005; 28(2):67–72.

Justus D, Dalugge D, Bothe S, Fuhrmann F, Hannes C, Kaneko H, Friedrichs D, Sosulina L, Schwarz I, Elliott DA, Schoch S, Bradke F, Schwarz MK, and Remy S. Glutamatergic synaptic integration of locomotion speed via septoentorhinal projections. *Nat Neurosci*, 2017; 20(1):16–19.

Keller MK, Draguhn A, Both M, and Reichinnek S. Activity-dependent plasticity of mouse hippocampal assemblies in vitro. *Front Neural Circuits*, 2015; 9:21.

Kennedy PJ and Shapiro ML. Motivational states activate distinct hippocampal representations to guide goal-directed behaviors. *Proc Natl Acad Sci U S A*, 2009; 106(26):10805–10.

Kim HB, Oh TI, Swanberg KM, Lee MB, Kim TW, Woo EJ, Park JH, and Kwon OI. Microelectrode array analysis of hippocampal network dynamics following theta-burst stimulation via current source density reconstruction by gaussian interpolation. *J Neurosci Methods*, 2016; 264:1–10.

Klausberger T, Magill PJ, Marton LF, Roberts JD, Cobden PM, Buzsaki G, and Somogyi P. Brain-state- and cell-type-specific firing of hippocampal interneurons in vivo. *Nature*, 2003; 421(6925):844–8.

Klausberger T, Marton LF, O'Neill J, Huck JH, Dalezios Y, Fuentealba P, Suen WY, Papp E, Kaneko T, Watanabe M, Csicsvari J, and Somogyi P. Complementary roles of cholecystokinin- and parvalbumin-expressing gabaergic neurons in hippocampal network oscillations. *J Neurosci*, 2005; 25(42):9782–93.

Lapray D, Lasztoczi B, Lagler M, Viney TJ, Katona L, Valenti O, Hartwich K, Borhegyi Z, Somogyi P, and Klausberger T. Behavior-dependent specialization of identified hippocampal interneurons. *Nat Neurosci*, 2012; 15(9):1265–71.

Larson J and Munkacsy E. Theta-burst ltp. *Brain Res*, 2015; 1621:38–50.

Lee AK and Wilson MA. Memory of sequential experience in the hippocampus during slow wave sleep. *Neuron*, 2002; 36(6):1183–94.

Lever C, Wills T, Cacucci F, Burgess N, and O'Keefe J. Long-term plasticity in hippocampal place-cell representation of environmental geometry. *Nature*, 2002; 416(6876):90–4.

Li XG, Somogyi P, Ylinen A, and Buzsaki G. The hippocampal ca3 network: an in vivo intracellular labeling study. *J Comp Neurol*, 1994; 339(2):181–208.

Lin JY, Lin MZ, Steinbach P, and Tsien RY. Characterization of engineered channelrhodopsin variants with improved properties and kinetics. *Biophys J*, 2009; 96(5):1803–14.

Lorente de No R. Studies on the structure of the cerebral cortex. ii. *J Psychol Neurol*, 1934; (46):113–177.

Magee JC and Johnston D. A synaptically controlled, associative signal for hebbian plasticity in hippocampal neurons. *Science*, 1997; 275(5297):209–13.

Maier N, Morris G, Johenning FW, and Schmitz D. An approach for reliably investigating hippocampal sharp wave-ripples in vitro. *PLoS One*, 2009; 4(9):e6925.

Maier N, Nimmrich V, and Draguhn A. Cellular and network mechanisms underlying spontaneous sharp wave-ripple complexes in mouse hippocampal slices. *J Physiol*, 2003; 550(Pt 3):873–87.

Maier P, Kaiser ME, Grinevich V, Draguhn A, and Both M. Differential effects of oxytocin on mouse hippocampal oscillations in vitro. *Eur J Neurosci*, 2016; 44(11):2885–2898.

Mann EO, Suckling JM, Hajos N, Greenfield SA, and Paulsen O. Perisomatic feedback inhibition underlies cholinergically induced fast network oscillations in the rat hippocampus in vitro. *Neuron*, 2005; 45(1):105–17.

Mattis J, Tye KM, Ferenczi EA, Ramakrishnan C, O'Shea DJ, Prakash R, Gunaydin LA, Hyun M, Fenno LE, Gradinaru V, Yizhar O, and Deisseroth K. Principles for applying optogenetic tools derived from direct comparative analysis of microbial opsins. *Nat Methods*, 2012; 9(2):159–72.

McBain CJ and Fisahn A. Interneurons unbound. *Nat Rev Neurosci*, 2001; 2(1):11–23.

McGaugh JL. Memory–a century of consolidation. *Science*, 2000; 287(5451):248–51.

Mitra A, Mitra SS, and Tsien RW. Heterogeneous reallocation of presynaptic efficacy in recurrent excitatory circuits adapting to inactivity. *Nat Neurosci*, 2011; 15(2):250–7.

Miyashita T, Shao YR, Chung J, Pourzia O, and Feldman DE. Long-term channelrhodopsin-2 (chr2) expression can induce abnormal axonal morphology and targeting in cerebral cortex. *Front Neural Circuits*, 2013; 7:8.

Moca VV, Nikolic D, Singer W, and Muresan RC. Membrane resonance enables stable and robust gamma oscillations. *Cereb Cortex*, 2014; 24(1):119–42.

Morris R. Developments of a water-maze procedure for studying spatial learning in the rat. *Journal of Neuroscience Methods*, 1984; 11(1):47–60.

Moser EI, Kropff E, and Moser MB. Place cells, grid cells, and the brain's spatial representation system. *Annu Rev Neurosci*, 2008; 31:69–89.

Muller GE and Pilzecker A. *Experimentelle beitraege zur lehre vom gedaechtniss*, volume 1. JA Barth, 1900.

Nadel L and Moscovitch M. Memory consolidation, retrograde amnesia and the hippocampal complex. *Curr Opin Neurobiol*, 1997; 7(2):217–27.

Nagel G, Brauner M, Liewald JF, Adeishvili N, Bamberg E, and Gottschalk A. Light activation of channelrhodopsin-2 in excitable cells of caenorhabditis elegans triggers rapid behavioral responses. *Curr Biol*, 2005; 15(24):2279–84.

Nait Oumesmar B, Vignais L, and Baron-Van Evercooren A. Developmental expression of platelet-derived growth factor alpha-receptor in neurons and glial cells of the mouse cns. *J Neurosci*, 1997; 17(1):125–39.

Nathanson JL, Yanagawa Y, Obata K, and Callaway EM. Preferential labeling of inhibitory and excitatory cortical neurons by endogenous tropism of adeno-associated virus and lentivirus vectors. *Neuroscience*, 2009; 161(2):441–50.

Neff JA, Athale RA, and Lee SH. Two-dimensional spatial light modulators: a tutorial. *Proceedings of the IEEE*, 1990; 78(5):826–855.

Nevian T, Larkum ME, Polsky A, and Schiller J. Properties of basal dendrites of layer 5 pyramidal neurons: a direct patch-clamp recording study. *Nat Neurosci*, 2007; 10(2):206–214.

Obien ME, Deligkaris K, Bullmann T, Bakkum DJ, and Frey U. Revealing neuronal function through microelectrode array recordings. *Front Neurosci*, 2014; 8:423.

O'Keefe J and Dostrovsky J. The hippocampus as a spatial map. preliminary evidence from unit activity in the freely-moving rat. *Brain Res*, 1971; 34(1):171–5.

O'Keefe J and Recce ML. Phase relationship between hippocampal place units and the eeg theta rhythm. *Hippocampus*, 1993; 3(3):317–30.

Oliva A, Fernandez-Ruiz A, Buzsaki G, and Berenyi A. Role of hippocampal ca2 region in triggering sharp-wave ripples. *Neuron*, 2016; 91(6):1342–55.

Osipova D, Takashima A, Oostenveld R, Fernandez G, Maris E, and Jensen O. Theta and gamma oscillations predict encoding and retrieval of declarative memory. *J Neurosci*, 2006; 26(28):7523–31.

Papagiakoumou E, Anselmi F, Begue A, de Sars V, Gluckstad J, Isacoff EY, and Emiliani V. Scanless two-photon excitation of channelrhodopsin-2. *Nat Methods*, 2010; 7(10):848–54.

Pastoll H, Solanka L, van Rossum MC, and Nolan MF. Feedback inhibition enables theta-nested gamma oscillations and grid firing fields. *Neuron*, 2013; 77(1):141–54.

Reichinnek S, Kunsting T, Draguhn A, and Both M. Field potential signature of distinct multicellular activity patterns in the mouse hippocampus. *J Neurosci*, 2010; 30(46):15441–9.

Reinhard K, Tikidji-Hamburyan A, Seitter H, Idrees S, Mutter M, Benkner B, and Munch TA. Step-by-step instructions for retina recordings with perforated multi electrode arrays. *PLoS One*, 2014; 9(8):e106148.

Rogers GL, Martino AT, Aslanidi GV, Jayandharan GR, Srivastava A, and Herzog RW. Innate immune responses to aav vectors. *Front Microbiol*, 2011; 2:194.

Roth FC, Beyer KM, Both M, Draguhn A, and Egorov AV. Downstream effects of hippocampal sharp wave ripple oscillations on medial entorhinal cortex layer v neurons in vitro. *Hippocampus*, 2016; 26(12):1493–1508.

Sadowski JH, Jones MW, and Mellor JR. Sharp-wave ripples orchestrate the induction of synaptic plasticity during reactivation of place cell firing patterns in the hippocampus. *Cell Rep*, 2016; 14(8):1916–29.

Scheffer-Teixeira R, Belchior H, Caixeta FV, Souza BC, Ribeiro S, and Tort AB. Theta phase modulates multiple layer-specific oscillations in the ca1 region. *Cereb Cortex*, 2012; 22(10):2404–14.

Scheffer-Teixeira R and Tort AB. On cross-frequency phase-phase coupling between theta and gamma oscillations in the hippocampus. *Elife*, 2016; 5.

Scheffzuk C, Kukushka VI, Vyssotski AL, Draguhn A, Tort AB, and Brankack J. Selective coupling between theta phase and neocortical fast gamma oscillations during rem-sleep in mice. *PLoS One*, 2011; 6(12):e28489.

Schlingloff D, Kali S, Freund TF, Hajos N, and Gulyas AI. Mechanisms of sharp wave initiation and ripple generation. *J Neurosci*, 2014; 34(34):11385–98.

Schonberger J, Draguhn A, and Both M. Lamina-specific contribution of glutamatergic and gabaergic potentials to hippocampal sharp wave-ripple complexes. *Front Neural Circuits*, 2014; 8:103.

Scoville WB. The limbic lobe in man. *J Neurosurg*, 1954; 11(1):64–6.

Scoville WB and Milner B. Loss of recent memory after bilateral hippocampal lesions. *J Neurol Neurosurg Psychiatry*, 1957; 20(1):11–21.

Sik A, Penttonen M, and Buzsaki G. Interneurons in the hippocampal dentate gyrus: an in vivo intracellular study. *Eur J Neurosci*, 1997; 9(3):573–88.

Sohal VS, Zhang F, Yizhar O, and Deisseroth K. Parvalbumin neurons and gamma rhythms enhance cortical circuit performance. *Nature*, 2009; 459(7247):698–702.

Somogyi P, Katona L, Klausberger T, Lasztoczi B, and Viney TJ. Temporal redistribution of inhibition over neuronal subcellular domains underlies state-dependent rhythmic change of excitability in the hippocampus. *Philos Trans R Soc Lond B Biol Sci*, 2014; 369(1635):20120518.

Spruston N and Johnston D. Perforated patch-clamp analysis of the passive membrane properties of three classes of hippocampal neurons. *J Neurophysiol*, 1992; 67(3):508–29.

Stark E, Roux L, Eichler R, Senzai Y, Royer S, and Buzsaki G. Pyramidal cell-interneuron interactions underlie hippocampal ripple oscillations. *Neuron*, 2014; 83(2):467–80.

Sullivan D, Csicsvari J, Mizuseki K, Montgomery S, Diba K, and Buzsaki G. Relationships between hippocampal sharp waves, ripples, and fast gamma oscillation: influence of dentate and entorhinal cortical activity. *J Neurosci*, 2011; 31(23):8605–16.

Szabo V, Ventalon C, De Sars V, Bradley J, and Emiliani V. Spatially selective holographic photoactivation and functional fluorescence imaging in freely behaving mice with a fiberscope. *Neuron*, 2014; 84(6):1157–69.

Teles-Grilo Ruivo LM and Mellor JR. Cholinergic modulation of hippocampal network function. *Front Synaptic Neurosci*, 2013; 5:2.

Tort AB, Komorowski R, Eichenbaum H, and Kopell N. Measuring phase-amplitude coupling between neuronal oscillations of different frequencies. *J Neurophysiol*, 2010; 104(2):1195–210.

Tort AB, Komorowski RW, Manns JR, Kopell NJ, and Eichenbaum H. Theta-gamma coupling increases during the learning of item-context associations. *Proc Natl Acad Sci U S A*, 2009; 106(49):20942–7.

Tort AB, Kramer MA, Thorn C, Gibson DJ, Kubota Y, Graybiel AM, and Kopell NJ. Dynamic cross-frequency couplings of local field potential oscillations in rat striatum and hippocampus during performance of a t-maze task. *Proc Natl Acad Sci U S A*, 2008; 105(51):20517–22.

Traub RD and Bibbig A. A model of high-frequency ripples in the hippocampus based on synaptic coupling plus axon-axon gap junctions between pyramidal neurons. *J Neurosci*, 2000; 20(6):2086–93.

Traub RD, Whittington MA, Colling SB, Buzsaki G, and Jefferys JG. Analysis of gamma rhythms in the rat hippocampus in vitro and in vivo. *J Physiol*, 1996; 493 (Pt 2):471–84.

Tulving E and Markowitsch HJ. Episodic and declarative memory: role of the hippocampus. *Hippocampus*, 1998; 8(3):198–204.

van Vugt MK, Schulze-Bonhage A, Litt B, Brandt A, and Kahana MJ. Hippocampal gamma oscillations increase with memory load. *J Neurosci*, 2010; 30(7):2694–9.

Vanderwolf CH. Hippocampal electrical activity and voluntary movement in the rat. *Electroencephalogr Clin Neurophysiol*, 1969; 26(4):407–18.

Vargha-Khadem F. Differential effects of early hippocampal pathology on episodic and semantic memory. *Science*, 1997; 277(5324):376–380.

Walker MP. The role of slow wave sleep in memory processing. *J Clin Sleep Med*, 2009; 5(2 Suppl):S20–6.

Walters RW, Yi SM, Keshavjee S, Brown KE, Welsh MJ, Chiorini JA, and Zabner J. Binding of adeno-associated virus type 5 to 2,3-linked sialic acid is required for gene transfer. *J Biol Chem*, 2001; 276(23):20610–6.

Wang SH, Teixeira CM, Wheeler AL, and Frankland PW. The precision of remote context memories does not require the hippocampus. *Nat Neurosci*, 2009; 12(3):253–5.

Wang X, Zhang C, Szabo G, and Sun QQ. Distribution of camkiialpha expression in the brain in vivo, studied by camkiialpha-gfp mice. *Brain Res*, 2013; 1518:9–25.

Wang XJ and Buzsaki G. Gamma oscillation by synaptic inhibition in a hippocampal interneuronal network model. *J Neurosci*, 1996; 16(20):6402–13.

Watakabe A, Ohtsuka M, Kinoshita M, Takaji M, Isa K, Mizukami H, Ozawa K, Isa T, and Yamamori T. Comparative analyses of adeno-associated viral vector serotypes 1, 2, 5, 8 and 9 in marmoset, mouse and macaque cerebral cortex. *Neurosci Res*, 2015; 93:144–57.

Whitlock JR, Heynen AJ, Shuler MG, and Bear MF. Learning induces long-term potentiation in the hippocampus. *Science*, 2006; 313(5790):1093–7.

Whittington MA, Traub RD, and Jefferys JG. Synchronized oscillations in interneuron networks driven by metabotropic glutamate receptor activation. *Nature*, 1995; 373(6515):612–5.

Wikipedia. Hippocampus. 2017. [Online; accessed 20-May-2017].

Wilson MA and McNaughton BL. Reactivation of hippocampal ensemble memories during sleep. *Science*, 1994; 265(5172):676–9.

Wiltgen BJ, Zhou M, Cai Y, Balaji J, Karlsson MG, Parivash SN, Li W, and Silva AJ. The hippocampus plays a selective role in the retrieval of detailed contextual memories. *Curr Biol*, 2010; 20(15):1336–44.

Winocur G. Anterograde and retrograde amnesia in rats with dorsal hippocampal or dorsomedial thalamic lesions. *Behav Brain Res*, 1990; 38(2):145–54.

Yamamoto J, Suh J, Takeuchi D, and Tonegawa S. Successful execution of working memory linked to synchronized high-frequency gamma oscillations. *Cell*, 2014; 157(4):845–57.

Yizhar O, Fenno LE, Davidson TJ, Mogri M, and Deisseroth K. Optogenetics in neural systems. *Neuron*, 2011; 71(1):9–34.

Ylinen A, Bragin A, Nadasdy Z, Jando G, Szabo I, Sik A, and Buzsaki G. Sharp wave-associated high-frequency oscillation (200 hz) in the intact hippocampus: network and intracellular mechanisms. *J Neurosci*, 1995; 15(1 Pt 1):30–46.

Yona G, Meitav N, Kahn I, and Shoham S. Realistic numerical and analytical modeling of light scattering in brain tissue for optogenetic applications(1,2,3). *eNeuro*, 2016; 3(1).

Zaiss AK, Liu Q, Bowen GP, Wong NC, Bartlett JS, and Muruve DA. Differential activation of innate immune responses by adenovirus and adeno-associated virus vectors. *J Virol*, 2002; 76(9):4580–90.

Zhang Y, Li J, Yang W, Zhang J, Wang P, and Xu W. Eliminate the influence of zero-order diffraction for wavefront reconstruction with selectable magnification in digital holographic. *Optical and Quantum Electronics*, 2013; 45(10):1077–1086.

7 List of Figures

8 List of Abbreviations

AAV	Adeno-associated virus	LFP	Local Field Potential
ACSF	Artificial cerebrospinal fluid	LTP	Long-term potentiation
AMPA	α-amino-3-hydroxy-5-methyl-4-isoxazolepropionic acid	MEA	Microelectrode array
ANOVA	Analysis of variance	ms	Millisecond
AOI	Area of illumination	NGS	Normal goat serum
CA3/CA1	Cornu ammonis area 3/1	PBS	Phosphate-buffered saline
CamKIIα	Calmodulin kinase IIα	PC	Pyramidal Cell
ChR2	Channelrhodopsin-2	PFA	Paraformaldehyde
DAPI	4',6-diamidino-2-phenylindole	PV	Parvalbumin
DG	Dentate Gyrus	REM	Rapid eye movement
DNA	Desoxyribonucleic acid	SEM	Standard error of the mean
EPSC/IPSC	Excitatory/Inhibitory post-synaptic current	SNLE	Smoothed non-linear energy
EtOH	Ethanol	SPW-R	Sharpwave-ripple complex
EYFP	Enhanced yellow-fluorescent protein	STD	Standard deviation
FELASA	Federation of European Laboratory Animal Science Associations	TTL	Transistor-transistor logic
FWHM	Full width at half-maximum		
GABA	γ-aminobutyric acid		

9 Acknowledgements

I would like to express my gratitude to Andreas Draguhn for taking me in as a greenhorn bachelor student from Zweibrücken. His openness and the supportive environment he creates within the group were a wonderful start to my scientific career which ultimately resulted in this thesis. I'd also like to thank my TAC members Rohini Kuner and Hilmar Bading for their valuable strategic advice on this project. Furthermore, I'd like to acknowledge the IZN/BCCN graduate programme and the DFG for providing financial support along with an excellent scientific framework which served as a great basis for this work.

Additionally, I would like to thank Martin Both for his supervision and for trusting me with the extremely expensive tools that I had great fun tinkering around with. It was nice having a MATLAB expert in the background who would be ready to jump in whenever one of those pesky errors popped up. Claus Bruehl should also be mentioned as the most powerful weapon in the battle against mains hum.

I'd like to acknowledge Martin Kaiser as not only my office neighbour but also for assembling and disassembling the recording setup (multiple times) with me. A very special thanks of course goes to Justus Schneider and Nadine Zuber for helping out with fluorescence stainings and to Vivan Nguyen Chi and Jan-Oliver Hollnagel for providing exemplary recordings from their data. A very big thanks also goes to Katja Lankisch who helped a great deal by performing intracranial virus injections allowing me to focus on recording and analysis. I also want to acknowledge the concerted efforts of Martin Both, Felix Friedl, Martin Kaiser and Jan-Oliver Hollnagel that went into developing the graphical user interface for controlling the imaging and illumination setup. Surely, all other "Draguhnis" should not be forgotten for producing an atmosphere in which I enjoyed working in.

Finally, I want to thank my family for never once doubting that I could be able to achieve my goals. This includes my fiancée Tairi with whom I shared the ups and downs of my PhD. Sincerely, thank you for believing in me.